

NUMERICAL MODELING OF MICROWAVE EMISSION FROM
IRREGULAR LAYER

by

LUIS MANUEL CAMACHO-VELAZQUEZ

Presented to the Faculty of the Graduate School of
The University of Texas at Arlington in Partial Fulfillment
of the Requirements
for the Degree of

DOCTOR OF PHILOSOPHY

THE UNIVERSITY OF TEXAS AT ARLINGTON

December 2011

Copyright © by Luis Manuel Camacho-Velazquez 2011

All Rights Reserved

ACKNOWLEDGEMENTS

I would like to express my sincere appreciation to my supervising professor, Dr. Saibun Tjuatja, for his guidance, assistance and stimulating discussions throughout my Doctor of Philosophy degree studies. My success in this Ph.D. program is largely due to his time, encouragement, and practical insights for not only the academic activities but also personal issues. I would also like to thank Dr. Mingyu Lu for his advices regarding the numerical analysis aspects in my research. I would also like to thank the members of my dissertation committee, Dr. Jonathan Bredow, Dr. Tuncay Aktosun, and Dr. Laureano Hoyos for their suggestions and for allocating their precious time in participating in my dissertation defense examination. Also, special thanks to the High Performance Computing system at the University of Texas at Arlington for providing computational resources for the numerical analysis.

I am deeply thankful to the Universidad Autónoma de Nuevo León, Mexico, for the support to carry out graduate studies at UTA. Especially to José A. González Treviño, José L. Castillo Ocañas, Cástulo E. Vela Villarreal, Rogelio G. Garza Rivera, Esteban Báez Villarreal and Eugenio López Guerrero.

Furthermore, I would like to share the satisfaction of this degree with my friends, José Mireles Jr., Humberto Ochoa, and Suman K. Gunnala for their discussions, help and generosity.

Finally, I would like to express my love and appreciation to my wife, Fina, and our children, Estefania, Ximena, and Luis, for their patience, understanding and unconditional support. I also thank my parents, José Delfino Camacho Nava, from whom I found out that learning is a lifetime process, and Luvia Velázquez de Camacho, for her prayers and love. Last,

but not least, I want to thank my brothers, sisters and family-in-law, for their encouragement. I dedicate this work to all of them.

November 30, 2010

ABSTRACT

NUMERICAL MODELING OF MICROWAVE EMISSION FROM IRREGULAR LAYER

Luis Manuel Camacho-Velazquez, PhD.

The University of Texas at Arlington, 2011

Supervising Professor: Saibun Tjuatja

A numerical approach to model the microwave emission from an irregular layer is developed. The phase matrix of the layer components as well as the emission characteristics are estimated using a numerical approach, namely the Finite-Difference Time-Domain (FDTD) method. The phase matrix is then integrated into a layer model that accounts for the scattering between the layer and ground, using the radiative transfer theory. The effects of interface roughness on emission are incorporated into the model through the surface phase matrices, which are computed using the Integral Equation Model (IEM).

The validity of the phase matrices computation is tested against theoretical models. Similarly, the numerical model is validated by comparing its results with field measurements. For this purpose the components of the irregular layer are chosen to be corn stalks, represented by vertical dielectric cylinders. The bottom half-space bottom is chosen to be soil with rough surface. The microwave emission model predictions are then compared to those field measurements, showing a good agreement.

TABLE OF CONTENTS

ACKNOWLEDGEMENTS	iii
ABSTRACT	v
LIST OF ILLUSTRATIONS	ix
LIST OF TABLES	xiv
Chapter	Page
1. INTRODUCTION	1
1.1 Remote sensing	1
1.2 Microwave frequency range for emission from soil	3
1.3 Classification of approaches to model emission and scattering from vegetation canopies	4
1.4 Current work	4
1.5 Approach used in study	7
2. RADIATIVE TRANSFER FORMULATION.....	10
2.1 Stokes parameters	12
2.2 Phase function and phase matrix.....	13
2.2.1 Phase matrix of rough surfaces	14
2.3 Radiative transfer equation	15
2.4 Scattering from an inhomogeneous layer with irregular boundaries	17
2.5 Emission model for an inhomogeneous layer	18
2.6 Formulation of surface scattering matrices using the Integral Equation method	19

3. FINITE DIFFERENCE TIME DOMAIN (FDTD) METHOD.....	22
3.1 Introduction to the Finite Difference Time Domain (FDTD) method	23
3.2 Maxwell's equations in three dimensions	23
3.2 The Yee algorithm	26
3.4 Finite differences and notation.....	28
3.5 Finite differences expressions for Maxwell's equations in three dimensions	30
4. NUMERICAL COMPUTATION OF EMISSION FROM FINITE-SIZE OBJECTS	37
4.1 Emission theory.....	37
4.2 Validation of FDTD results by comparison with analytical results using Mie series solutions.....	39
4.3 Validation of FDTD results by comparison with method of moments (MoM) results	42
4.4 Cross sections computation using FDTD and Mie series solutions	48
4.5 Computation of emissivity from finite size objects	52
4.5.1 Introduction	52
4.5.2 Emission from finite-size objects.....	53
4.5.3 Numerical modeling approach	55
4.5.4 Numerical computation of emissivity from lossless objects	58
4.5.5 Numerical computation of emissivity of lossy dielectric objects	63
4.5.6 Results and analysis	64
5. MODELING OF MICROWAVE EMISSION FROM IRREGULAR LAYER	75
5.1 Introduction.....	75

5.2 Construction of phase matrix for a circular cylinder.....	75
5.3 Construction of phase matrix of corn stalks represented by cylinders.....	81
5.4 Validation of phase matrices for energy conservation	83
5.5 Verification of computation of backward and forward phase matrices.....	85
5.6 Emission scattering mechanisms.....	88
5.7 Determination of effective permittivity of layer	92
5.8 Validation of model by comparison with field measurements.....	93
6. CONCLUSIONS AND RECOMMENDATIONS.....	97
6.1 Summary and conclusions	97
6.2 Future work.....	98
APPENDIX	
A. LIST OF ABBREVIATIONS	99
REFERENCES.....	101
BIOGRAPHICAL INFORMATION	105

LIST OF ILLUSTRATIONS

Figure	Page
2.1 Geometry for specific intensity and the change in intensity I	10
2.2 Scattering from an inhomogeneous layer above a homogeneous half space	17
3.1 Positions of field components. The \vec{E} -components are in the middle of edges and the \vec{H} -components are in the center of the faces.....	26
3.2 Leapfrog time integration.....	28
3.3 Staircased sphere in cubical Yee cells.....	36
4.1 The brightness temperature of an object is related to its physical temperature by its emissivity.....	38
4.2 Configuration for simulation of plane wave impinging on a dielectric sphere	40
4.3 Comparison of scattered field values obtained by using FDTD and Mie series solution. (a) E_θ and E_ϕ , (b) H_θ and H_ϕ (normalized to $ \vec{H}_{inc} $).....	42
4.4 Geometry used to compute scattering from a cylinder Figure reproduced from [47]	44
4.5 General scattering pattern of a cylinder Figure reproduced from [47]	45
4.6 Normalized bistatic scattering coefficient vs. scattering angle for finite dielectric cylinder computed with FDTD and MoM. The parameters of the cylinder are $L = 10.0\lambda_0$, $a = 0.4\lambda_0$, $\epsilon = 18 - j6$, and incident angle $\theta_i = 20^\circ$ (top) and $\theta_i = 80^\circ$ (bottom).....	47
4.7 Comparison of absorption cross section of a 4 - cm diameter sphere using analytical solution and FDTD simulations. The properties	

of the sphere are $\epsilon_r = 4.0$ and $\sigma = 0.1 S/m$. The Yee cell is $\Delta x = 0.001m$ ($0.0167 - 0.0233 \lambda_0$)	49
4.8 Comparison of absorption cross section of a 4- <i>cm</i> diameter sphere using analytical solution and FDTD simulations. The properties of the sphere are $\epsilon_r = 4.0$ and $\sigma = 0.1 S/m$. The Yee cell is $\Delta x = 0.00050m$ ($0.0083 - 0.0117 \lambda_0$)	49
4.9 Comparison of absorption cross section of a 4- <i>cm</i> diameter sphere using analytical solution and FDTD simulations. The properties of the sphere are $\epsilon_r = 10.0$ and $\sigma = 0.5 S/m$. The Yee cell is $\Delta x = 0.000315m$ ($0.00525 - 0.00735 \lambda_0$)	50
4.10 Comparison of absorption cross section of a 4- <i>cm</i> diameter sphere using analytical solution and FDTD simulations. The properties of the sphere $\epsilon_r = 4.0$ and $\sigma = 0.5 S/m$. The Yee cell is $\Delta x = 0.001m$ ($0.0167 - 0.0233 \lambda_0$)	50
4.11 Comparison of absorption cross section of a 4- <i>cm</i> diameter sphere using analytical solution and FDTD simulations. The properties of the sphere are $\epsilon_r = 10.0$ and $\sigma = 0.1 S/m$. The Yee cell is $\Delta x = 0.00063m$ ($0.0083 - 0.0117 \lambda_0$)	51
4.12 Comparison of absorption cross section of a 4- <i>cm</i> diameter sphere using analytical solution and FDTD simulations. The properties of the sphere are $\epsilon_r = 10.0$ and $\sigma = 0.1 S/m$. The Yee cell is $\Delta x = 0.000315m$ ($0.00525 - 0.00735 \lambda_0$)	51
4.13 Virtual enclosing surface used for computation of cross sections. For absorption cross section the enclosing surface is generated in the FDTD total field region, while for the scattering cross section the enclosing surface is generated in the scattered field region.....	56
4.14 Virtual enclosing surface used for computation of cross sections using the Gaussian quadrature technique. For absorption cross section the enclosing surface uses the FDTD total field values, while for the scattering cross section the enclosing surface uses the scattered fields by subtracting the incident field from the total field.....	56
4.15 Emissivity of lossless cylinder with respect to incident angle, when varying the cell size Δs from $0.00075m$ to $0.00125m$. The dimensions of the cylinder are: diameter = $0.05m$ and height = $0.05m$. The dielectric properties are $\epsilon_r = 4.0$ and $\sigma = 0 S/m$.	

The frequency of analysis is 5GHz . The polarization is vertical	59
4.16 Emissivity of lossless cylinder with respect to incident angle, when varying the cell size from Δs from 0.0005m to 0.0010m . The dimensions of the cylinder are: diameter = 0.04m and height = 0.04m . The dielectric properties are $\epsilon_r = 4.0$ and $\sigma = 0\text{S/m}$. The frequency of analysis is 6GHz . The polarization is vertical	60
4.17 Emissivity of lossless cylinder with respect to incident angle, when varying the cell size from Δs from 0.0005m to 0.0010m . The dimensions of the cylinder are: diameter = 0.04m and height = 0.04m . The dielectric properties are $\epsilon_r = 4.0$ and $\sigma = 0\text{S/m}$. The frequency of analysis is 5GHz . The polarization is vertical	61
4.18 Emissivity of PEC cube with respect to incident angle, when varying the cell size from Δs from 0.0005m to 0.0010m . The dimensions of the cube are: side = 0.04m . The frequency of analysis is 6GHz . The polarization is vertical.	62
4.19 Emissivity of PEC cube with respect to incident angle, when varying the cell size from Δs from 0.0005m to 0.0010m . The dimensions of the cube are: side = 0.04m . The frequency of analysis is 5GHz . The polarization is vertical.	63
4.20 Emissivity at 6GHz for a sphere ($r = \lambda_0$) with $\epsilon_r = 4.0$ and $\sigma = 0.1, 0.5\text{S/m}$	64
4.21 Geometry used for FDTD simulation of plane wave impinging on landmine-like object ($d = 2.4\lambda_0$ and $h = 0.8\lambda_0$)	65
4.22 Emissivity at 6GHz for a circular cylinder with $\epsilon_r = 4.0$ and $\sigma = 0.1, 0.125, 0.15, 0.2, 0.3, 0.5\text{S/m}$, for vertical polarization. Dimensions of the cylinder are $d = 2.4\lambda_0 (12\text{cm})$ and $h = 0.8\lambda_0 (4\text{cm})$	65
4.23 Emissivity at 6GHz for a circular cylinder with $\epsilon_r = 4.0$ and $\sigma = 0.1, 0.3, 0.5\text{S/m}$, for horizontal polarization. Dimensions of the cylinder are $d = 2.4\lambda_0 (12\text{cm})$ and $h = 0.8\lambda_0 (4\text{cm})$	66
4.24 Geometry used for FDTD simulation of plane wave impinging on cylinder ($d = 1.2\lambda_0 (6\text{cm})$ and $h = 3.6\lambda_0 (18\text{cm})$)	67

4.25 Emissivity at 6GHz for a circular cylinder with $\epsilon_r = 4.0$ and $\sigma = 0.1, 0.125, 0.15, 0.2, 0.3, 0.5 S/m$, for vertical polarization. Dimensions of the cylinder are $d = 1.2\lambda_0(6cm)$ and $h = 3.6\lambda_0(18cm)$	67
4.26 Emissivity at 6GHz for a circular cylinder with $\epsilon_r = 4.0$ and $\sigma = 0.1, 0.3, 0.5 S/m$, for horizontal polarization. Dimensions of the cylinder are $d = 1.2\lambda_0(6cm)$ and $h = 3.6\lambda_0(18cm)$	68
4.27 Geometry used for FDTD simulation of plane wave impinging on cylinder ($d = 1.6\lambda_0(8cm)$ and $h = 1.6\lambda_0(8cm)$)	69
4.28 Emissivity at 6GHz for a circular cylinder with $\epsilon_r = 4.0$ and $\sigma = 0.1, 0.125, 0.15, 0.2, 0.3, 0.5 S/m$, for vertical polarization. Dimensions of the cylinder are $d = 1.6\lambda_0(8cm)$ and $h = 1.6\lambda_0(8cm)$	69
4.29 Geometry used for FDTD simulation of plane wave impinging on cylinder ($d = 2.0\lambda_0(10cm)$ and $h = 1.2\lambda_0(6cm)$)	70
4.30 Emissivity at 6GHz for a circular cylinder with $\epsilon_r = 4.0$ and $\sigma = 0.1, 0.125, 0.15, 0.2, 0.3, 0.5 S/m$, for vertical polarization. Dimensions of the cylinder are $d = 2.0\lambda_0(10cm)$ and $h = 1.2\lambda_0(6cm)$	70
4.31 Geometry used for FDTD simulation of plane wave impinging on cylinder ($d = 1.2\lambda_0(6cm)$ and $h = 1.8\lambda_0(9cm)$)	71
4.32 Emissivity at 6GHz for a circular cylinder with $\epsilon_r = 4.0$ and $\sigma = 0.1, 0.125, 0.15, 0.2, 0.3, 0.5 S/m$, for vertical polarization. Dimensions of the cylinder are $d = 1.2\lambda_0(6cm)$ and $h = 1.8\lambda_0(9cm)$	71
4.33 Geometry used for FDTD simulation of plane wave impinging on cylinder ($d = 2.8\lambda_0(14cm)$ and $h = 0.4\lambda_0(2cm)$)	72
4.34 Emissivity at 6GHz for a circular cylinder with $\epsilon_r = 4.0$ and $\sigma = 0.1, 0.125, 0.15, 0.2, 0.3, 0.5 S/m$, for vertical polarization. Dimensions of the cylinder are $d = 2.8\lambda_0(14cm)$ and	

$h = 0.4\lambda_0 (2\text{ cm})$	72
5.1 Geometry of the object for computation of the phase matrix.....	76
5.2 Computational structure of the phase matrix for the first two Stokes parameters	78
5.3 Configuration for modeling of emission from soil in the presence of vertical cylindrical vegetation components. Dielectric cylinders are used to model the vegetation components.	80
5.4 Geometry used for FDTD simulation of plane wave impinging on cylinder	81
5.5 Corn stalks represented by dielectric cylinders.....	82
5.6 (a) Absorption and (b) scattering cross sections numerically computed for a dielectric cylinder representing a corn stalk.....	83
5.7 Energy conservation test results for numerically-computed phase matrices S^* and T^*	84
5.8 Emission from surface with a cover of a layer with phase matrices characterized as those of a sphere. The phase matrices were obtained using Mie-formulation fields, FDTD-computed fields (phase matrix normalized by analytical scattering cross section – FDTD1), and FDTD-computed fields (phase matrix normalized by scattering cross section using method described in chapter 4 – FDTD2), (a) V-polarization, and (b) H-polarization	87
5.9 General geometry for modeling of emission from soil in the presence of inhomogeneous layer.....	89
5.10 Emission scattering mechanisms for upwelling and downwelling emission from the layer and upwelling emission from the bottom half-space.....	89
5.11 Effective reflectivity matrix from the medium 2 - medium 3 interface	91
5.12 Comparison of model-predicted microwave emission and field measurements (ARC) from soil with a cover of corn stalks.....	95

LIST OF TABLES

Table	Page
3.1 Location of the different fields in the Yee cell.....	28
4.1 Parameters of object used in FDTD simulation of plane wave impinging on dielectric sphere	40
4.2 Parameters of incident plane wave and scattered field.....	41
4.3 Parameters used for comparison de computation of absorption cross section of a 4-cm-diameter sphere using analytical solution and FDTD simulations.....	48
5.1 Parameters used for computation of emission from ground covered with an inhomogeneous layer with phase matrices similar to those of a sphere	85
5.2 Parameters used for model-predicted emission.....	95

CHAPTER 1

INTRODUCTION

1.1 Remote sensing

The term “microwave remote sensing” encompasses the physics of radiowave propagation in and interaction with material media, including surface scattering, volume scattering and emission in the microwave region. Sensors used in microwave remote sensing are divided into two groups according to their modes of operation: active sensors are those that provide their own source of illumination and therefore contain a transmitter and a receiver, while passive sensors are simply receivers that measure the radiation emanating from the scene under observation.

In passive microwave remote sensing radiation is measured (emission, reflection, polarization). From these measurements, parameters such as temperature, radiation, soil moisture, sea surface salinity, and sea surface winds are inferred. Active sensors are also sensitive to such parameters, but active instruments are typically much larger, require larger antennas, and use more power. Some applications of microwaves to remote sensing, such as scattering and emission from agricultural soil, snow and atmosphere are given in [1].

Models have been developed to characterize the emission from soil to interpret the observed relations between radiometer observations and soil parameters [2]. In fact, extensive research has been carried out to estimate the emission from bare surfaces [3-5]. However, the emission from soils is in many cases affected by a vegetation layer, which attenuates the soil emission and adds its own contribution to the land surface emission. In order to account for it,

models have been developed that incorporate the effect of vegetation on soil's microwave emission [6]. The problem of electromagnetic scattering by vegetation has received much attention in recent years, particularly with the deployment of air and satellite-born Synthetic Aperture Radar (SAR) instruments. It is therefore especially important to have dependable models to characterize the electromagnetic behavior of vegetation.

Numerous research works have been published to document the merits of the proposed models and many more have reported the results of experimental observations; however, many unresolved questions remain about the nature of the wave-target interaction process, both in the canopy volume and between the canopy elements and the underlying soil surface. For the most part, the applicability of a given model to a given target type is evaluated by comparing the model-calculated scattering coefficient or brightness temperature to the corresponding measured values. The model is based on certain assumptions and is a function of a set of electromagnetic and physical parameters of the target, from which many are difficult to measure and are, therefore, selected such that the fit between the model and observations are optimized.

In general, scattering consists of both surface scattering due to the boundary discontinuities and volume scattering due to inhomogeneities in the medium. Hence, the modeling of scattering requires an appropriate combination of surface-scattering and volume-scattering methods. In volume scattering, two general approaches have been used: the wave approach and the intensity approach, also referred to as radiative transfer approach [7, 8]. The wave approach relies on Maxwell's equations and can be rigorously formulated. However, to obtain useful, practical results, some approximations must be made. When the volume-scattering problem is formulated in terms of the averaged power or intensity based on the radiative transfer principle [8-10], strong dielectric fluctuations and certain types of multiple scattering can be included.

Surface scattering from a rough surface has been studied extensively [3, 4]. The problem of scattering from rough surfaces has been studied using low frequency (Small Perturbation Method -- SPM) and high frequency (Kirchhoff) approximations. For rough surfaces with different scales of roughness, two-scale models combining the two aforementioned approximations were used. However, a rough surface in reality may have a continuous scale of roughness and may not follow a two-scale model. As the scattering elements of rough surfaces present a complex geometry and are randomly distributed, their electromagnetic scattering involves complex interactions. The Integral Equation Method (IEM) [11] combines the two approximations together and can be used to model surfaces with arbitrary roughness scales.

1.2 Microwave frequency range for emission from soil

It has been found that the microwave frequency range that works best for soil moisture monitoring is 1-2 GHz (L-band) because at this frequency range (a) the atmosphere is in effect transparent, (b) vegetation is semi-transparent, hence, allowing observations of the surface, and (c) the microwave measurement is strongly dependent on soil moisture. Additionally, because of the long electromagnetic wavelength of the incident wave (21 cm for a 1.4 GHz wave); the surface roughness effects are small. In principle, vegetation effects are also small, but they cannot be neglected if the observation angle is large and/or the vegetation cover is thick or dense. Hence, most of the measurements as well as model predictions are carried out in that frequency range; however, uncertainties related to surface roughness and the absorption, scattering, and emission by vegetation must be resolved before soil moisture retrieval algorithms can be applied with known and acceptable accuracy using satellite observations.

1.3 Classification of approaches to model emission and scattering from vegetation canopies

In the microwave region, most vegetation canopies are considered inhomogeneous media, and in some cases, anisotropic also. Generally, efforts to model the radar backscattering and radiometric emission from vegetation follow one of two basic approaches. In the first approach, the canopy is treated as a continuous random medium with an average dielectric constant ϵ_a and a fluctuating component $\epsilon_f(x, y, z)$, which, in the general case, may be formulated as a tensor. When modeled using the second approach, the canopy is treated as the sum of discrete elements each characterized by a scattering phase function that relates the directional distribution of energy scattered by the element to the energy incident upon it.

Models to compute the emission are mainly classified in the following groups: (a) simple model, where vegetation is treated as a purely absorbing layer and is incorporated into an attenuation parameter; (b) parametric models, which rely on vegetation parameters; and (c) physical models.

1.4 Current work

To get a better understanding of microwave emission from vegetation, measurements at 2.7 and 5.1 GHz for row crops have been performed using a metallic screen under the vegetation layer so that the emission from the soil is not considered [12].

A model based on radiative transfer theory was used at high-frequencies (10 and 37 GHz) to evaluate the effects of single-plant constituents on the total emission from crops. The effects were evaluated by means of measurements carried out on plants in natural conditions and after sequential cuts of fruits, leaves, and stems. The analyzed crops had vertical stems [13].

In a program consisting of numerous field and aircraft experiments, it was determined that a 21-cm wavelength radiometer was the best single sensor for soil moisture research [14].

Furthermore, in order to assess the effect of man-made vegetation canopies, a field-approach two-dimensional model was developed to explain wave propagation through such canopies. The model was found to provide excellent agreement with the experimental results, although a 3D model has to be developed [15].

Using the Ulaby and El-Rayes model, a study of the vegetation effects on the microwave emission from soils was performed to estimate the absorption loss and optical depth of plant canopies for frequencies ranging from 1 to 40 GHz [16].

A study to quantify the sensitivities of soil moisture retrieved using an L-band single-polarization algorithm to three land surface parameters for corn and soybean sites was carried out [17].

Many retrieval approaches are based on the $\tau - \omega$ model [18]. The $\tau - \omega$ model has been found to be accurate at L-band. It relies on two vegetation parameters: the optical depth (τ), which parameterizes the attenuation effects; and the single-scattering albedo (ω), which parameterizes the scattering effects within the canopy. Hence, a characterization of the dependence of vegetation model parameters on crop structure, incidence angle and polarization at L-band for several crop types using the $\tau - \omega$ model was carried out [19].

Several backscatter and emission models of corn canopies for soil moisture retrieval, in general assume a uniform distribution of leaves and stalks, and hence treat the canopy as a uniform layer. The model parameters are optimized to yield good agreement with experimental data when data is restricted to a particular observation angle and polarization. However, azimuthal angle dependence of emission by the canopy is not considered by these models. Therefore, a simulation study was performed at L-band to analyze the effect of structural

features of vegetation canopies on brightness temperature. The simulations were performed on quasi-periodic corn canopies consisting of only stalks. It was shown that at low angles of incidence the effect the canopy row structure is reduced and the canopy looks similar a uniform canopy. At higher angles of incidence the effect of canopy structure on emission is observed through the azimuthal dependence of the canopy emission. In order to simplify the analysis, the underlying ground is assumed to be a perfect conduction (PEC) plane to eliminate emission by the ground [20].

With respect to physical models, a microwave radiometry model for a vegetation canopy was developed by Karam [21]. The model is based on an iterative solution of the radiative transfer equations. In the model, finite-length dielectric cylinders were used to represent some vegetation components. The scattering amplitude tensors for finite length cylinders were calculated through estimating the inner field with its corresponding inside infinite cylinders having similar radial properties. In this regard, a validation of both surface- and volume-current models for electromagnetic scattering from finite-length dielectric cylinders was carried out [22]. These approaches require the length of the cylinder to be much larger than its diameter.

A discrete model to evaluate vegetation effect in passive microwave soil moisture retrieval was given in [23]. In this model, vegetation canopy consisted of discrete scatters such as leaves, stems, branches with various sizes and orientations. A Matrix Doubling algorithm was used for the vegetation layer, so the multiple scattering within the canopy could be accounted for. The surface scattering was modeled by the IEM algorithm. Preliminary results showed that the emission from soil is dominant; the vegetation mainly acts as an absorption layer.

A comparison between theory and experiment of radiometric measurements over bare field and covered with grass, soybean, corn, and alfalfa made with 1.4- and 5-GHz microwave radiometers was carried out [24]. The measured results were compared with radiative transfer theory treating the vegetated fields as a two-layer random medium. It was found that the presence of a vegetation cover generally gives a higher brightness temperature than that expected from a bare soil.

A major component of the emission from vegetation-covered soil is the emission coming from the surface. A key factor that affects the surface emission is the surface roughness. For example, using land surface process/radiobrightness (LSP/R) model for prairie grassland the L-band brightness predicted appeared to be lower than expected. A crucial reason for the underestimation was that the surface was assumed to be smooth. In [25] the surface roughness effects were included by means of the IEM model. Furthermore, another parameter to be included in simulations is the vegetation volumetric fraction. An analysis about the effect of the variation of this parameter, in addition to surface roughness, was given in [26]. A more comprehensive analysis of other models for vegetation has been described in [3].

1.5 Approach used in study

All phenomena involving electromagnetic fields can be mathematically described by applying Maxwell's equations. Unfortunately, solving these equations analytically is often very difficult, and certain approximations have to be introduced to obtain a practical solution. One option to circumvent this issue is the use of other analysis techniques. Some of these techniques are the numerical methods, which are used to perform a simulation of electromagnetic wave propagation in different media [27]. The obtained results using numerical methods are accurate to within the tolerance that can be arbitrarily preset, and the simulated objects can be of any

shape and size, limited only by the available computational resources. For those reasons, numerical methods represent very attractive tools for modeling and analysis of various electromagnetic problems. For this purpose, in this research the Finite-Difference Time-Domain Method (FDTD) is used, which solves Maxwell's equations [28, 29]. The FDTD method has proven to be an effective technique of calculating the interaction of electromagnetic waves with bodies of different material, and complex, hence realistic geometries [30, 31]. Numerical methods did not gain much importance until recently because of the lengthy computational time and enormous amount of memory required to get solutions; but now, with the current powerful computational resources, numerical methods are becoming the primary methods to observe electromagnetic wave propagation, scattering and penetration.

In this study, the vegetation layer is represented as an inhomogeneous layer, on top of a homogeneous half space, representing the soil. On top of the inhomogeneous layer, another homogeneous half space is present, representing air. Therefore, a key component of this research is to characterize the scattering and emission properties of the inhomogeneous layer.

In [32] a 3D-FDTD algorithm was developed and used to compute the emissivity of finite-size cylindrical-shape objects, though it can be used for any arbitrary-shape object. A similar approach is also used in this research to attain not only the emission properties of the layer components under study, but also the scattering characteristics. An indirect method is used to analyze a passive emission problem by simulating an active scattering problem, in which a numerical method is used to simulate the interaction of a plane wave and the object. Contrary to the limitations with respect to the geometry of the body in other approaches [33], in this study an object of arbitrary shape could be analyzed.

The scattering properties of the object are also obtained and used to generate the phase matrix, which relates the scattered intensities to the incident intensities. The phase matrix is

then integrated into a radiative transfer model, involving the inhomogeneous layer, and the homogenous half spaces mentioned above.

The organization of this dissertation is as follows: Chapter 2 offers a description of the radiative transfer theory. The construction of surface scattering matrices using the Integral Equation Method is also given. Radiative transfer equations do not have closed-form solutions; an iterative process is used to get the solutions which provide some insight into the mechanics of scattering. Hence, radiative transfer theory sets up an iterative integral equation to compute the emissivity from the layer. This process of setting up the equation for iterative solution is given also in Chapter 2. A description of the numerical technique to be used, namely, the FDTD method is given in Chapter 3. A validation of the accuracy of the computational approach used to perform the simulation is given in Chapter 4. This validation is carried out by comparing the results obtained using the FDTD approach with analytical solutions as well as published results. Also, the numerical computation of emissivity from finite-size objects is given in Chapter 4. Chapter 5 gives the numerical approach to generate the phase matrix, and the approach used to integrate the phase matrix into a layer model. The model is then validated by comparing its predictions with field measurements. The contribution of this work and suggestions for future work related to this dissertation are discussed in Chapter 6.

CHAPTER 2

RADIATIVE TRANSFER FORMULATION

The basic development and formulation of radiative transfer theory is provided by Chandrasekhar [34]. Several researchers have contributed to this theory [5, 35]. For ease of reference a brief discussion of this model is given here. The classical derivation of the radiative transfer theory is based on the amount of radiant energy, transported across the medium, expressed in terms of specific intensity I_ν . The specific intensity is defined in terms of amount of power dP flowing along the \hat{r} direction within the solid angle $d\Omega$ through an elementary area dA in a frequency interval $(\nu, \nu + d\nu)$ as follows:

$$dP = I_\nu(\hat{r})(\cos \alpha) dA d\Omega d\nu \quad (2.1)$$

where α is the angle between the outward normal \hat{a} to dA and the unit vector \hat{r} as shown in Figure 2.1.

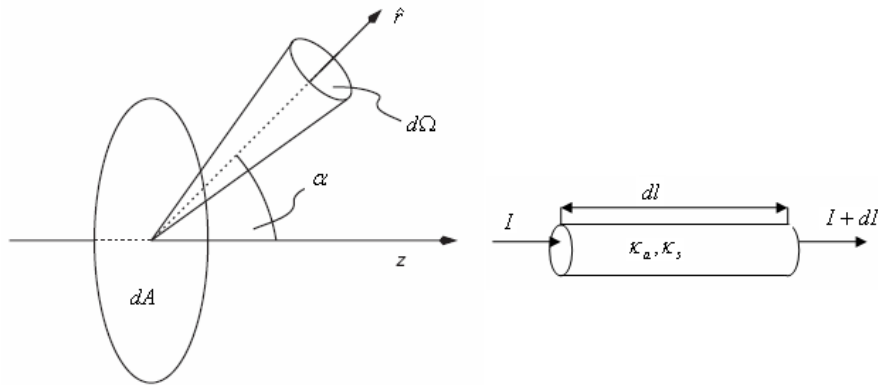


Figure 2.1 Geometry for specific intensity and the change in intensity I .

The dimension of I_ν is $Wm^{-2}sr^{-1}Hz^{-1}$. It is convenient to consider the intensity I at frequency ν , therefore $I(\hat{r}) = I_\nu(\hat{r})d\nu$. Hence, the power at a single frequency can be written as

$$dP = I(\hat{r})(\cos \alpha) dA d\Omega \quad (2.2)$$

The equation of transfer governs the variation of intensities in a medium that absorbs, emits and scatters radiation. Within the medium, consider a cylindrical volume of unit cross section and length dl as shown in Figure 2.1. Energy balance requires that the change in intensity I propagating through the cylindrical volume along the distance dl is due to absorption loss, scattering loss, thermal emission and scattering in the direction of propagation, i.e.,

$$dI = -\kappa_a I dl - \kappa_s I dl + \kappa_a J_a dl + \kappa_s J_s dl \quad (2.3)$$

where κ_a and κ_s are the volume absorption and volume scattering coefficients, respectively. The first two terms on the right hand side of (2.3) represent, respectively, absorption loss and loss due to scattering away from the direction of propagation, and J_a and J_s are the emission source function and the scattering source function representing the energy scattered into the direction of propagation. Equation (2.3) is the radiative transfer equation where J_s is given by

$$J_s(\theta_s, \phi_s) = \frac{1}{4\pi} \int_0^{2\pi} \int_0^\pi P(\theta_s, \phi_s; \theta, \phi) I(\theta, \phi) \sin \theta d\theta d\phi \quad (2.4)$$

where $P(\theta_s, \phi_s; \theta, \phi)$ is the phase function accounting for scattering within the medium.

2.1 Stokes parameters

Light gets polarized on scattering; therefore exact treatment of polarized radiation is required. To describe a polarized beam generally four parameters should be specified, which will give the intensity, the degree of polarization, the plane of polarization, and the ellipticity of the radiation at each point and in any given direction [34]. However, it is difficult to include such diverse quantities as intensity, a ratio, an angle, and a pure number in any symmetrical way in formulating the equations of transfer. In radiative transfer theory, the Stokes parameters are used to describe the partially polarized electromagnetic waves.

Consider an elliptically polarized monochromatic plane wave

$$\vec{E} = (E_v \hat{v} + E_h \hat{h}) \exp(j \vec{k} \cdot \vec{r} - j \omega t) \quad (2.5)$$

propagating through a differential solid angle $d\Omega$ in a medium with intrinsic impedance η .

The vertical and horizontal polarization states are represented by \hat{v} and \hat{h} unit vectors, and vertically and horizontally polarized incident field components are denoted by E_v and E_h , respectively. The modified Stokes parameters I_v , I_h , U , and V in the dimension of intensity are defined as

$$I_v d\Omega = \langle |E_v|^2 \rangle / \eta \quad (2.6)$$

$$I_h d\Omega = \langle |E_h|^2 \rangle / \eta \quad (2.7)$$

$$U d\Omega = 2 \operatorname{Re} \langle E_v E_h^* \rangle / \eta \quad (2.8)$$

$$V d\Omega = 2 \operatorname{Im} \langle E_v E_h^* \rangle / \eta \quad (2.9)$$

In (2.6) to (2.9) the symbol $\langle \cdot \rangle$ denotes a time average. These four Stokes parameters have the same dimensions and hence are more convenient to use than amplitude and phase,

which have different dimensions. It has been shown that the amplitude, phase, and polarization state of any elliptically polarized wave can be completely characterized by these parameters [8]. Due to the additivity of the average power of independent waves, the Stokes parameters are additive only for incoherent waves.

2.2 Phase function and phase matrix

Scattering is the interaction between electromagnetic wave and the medium. This interaction can be characterized in terms of its scattering properties, i.e., scattering cross sections, or its thermal emission spectrum. During scattering the medium takes energy from the incident wave and reradiates depending upon the ratio of scatter size to the wavelength of the incident wave. The phase function gives the rate at which the energy is scattered per unit solid angle in a given direction to the average energy in all directions [34]. In addition to the angular distribution of the scattered radiation at microwave frequencies, the scattering and emission from natural surfaces are largely determined by the surface roughness and the inhomogeneous profile of the dielectric constant, temperature and the volume scattering property. In the remote sensing of soil moisture at microwave frequencies, the non-uniform moisture and temperature profiles in the near-surface region and the rough surface play a dominant role. The effect of subsurface volume scattering plays a secondary role because of high absorption due to soil moistures.

Phase matrix is a quantity that relates the corresponding Stokes vectors of the scattered wave and the incident wave. Since the characteristics of the surface scattering and the volume scattering are different, the phase matrices defined for these two cases will also be different. For surface scattering, the incident wave excites surface currents on the surface that reradiate the scattered wave. So, the quantities used are generally normalized by the illuminated area.

While for volume scattering, the sources of re-radiation are volume currents, and then the quantities are normalized by the volume of the particle.

2.2.1 Phase matrix of rough surfaces

To relate the scattered intensity to the incident intensity, consider a plane wave illuminating a rough surface area A [3]. The relation between the vertically and horizontally polarized scattered field components E_v^s, E_h^s and those of the incident field components E_v^i, E_h^i is

$$\begin{bmatrix} E_v^s \\ E_h^s \end{bmatrix} = \frac{e^{jkR}}{R} \begin{bmatrix} S_{vv} & S_{vh} \\ S_{hv} & S_{hh} \end{bmatrix} \begin{bmatrix} E_v^i \\ E_h^i \end{bmatrix} \quad (2.10)$$

where S_{pq} ($p, q = v \text{ or } h$) is the scattering amplitude in meters, R is the distance from the center of the illuminated area to the point of observation, and k is the wave number. The scattering coefficient σ_{pq}^0 is defined as

$$\sigma_{pq}^0 = \frac{\langle |E_p^s|^2 \rangle}{A |E_q^i|^2 / (4\pi R^2)} \quad (2.11)$$

The matrix equation relates the scattered intensities I^s to the incident intensities I^i through the dimensionless quantity referred to as phase matrix P ,

$$I^s = \frac{1}{4\pi} P I^i d\Omega \quad (2.12)$$

The components of I^i are the Stokes parameters defined by (2.6) to (2.9) for the incident plane wave. The components of the scattered intensity I^s are also Stokes parameters but are defined for spherical waves. To sum up all possible incident intensities from all

directions contributing to I^s along a given direction, (2.12) is integrated over all solid angles, i.e.,

$$I^s = \frac{1}{4\pi} \int_{4\pi} P I^i d\Omega \quad (2.13)$$

Here I^s , I^i are column vectors whose components are the Stokes parameters. The detailed contents of the phase matrix are summarized below

$$P = 4\pi \langle M \rangle / (A \cos \theta_s) = \sigma^0 / \cos \theta_s \quad (2.14)$$

where the Stokes matrix M has been provided by Ishimaru [8],

$$\begin{bmatrix} |S_{vv}|^2 & |S_{vh}|^2 & \text{Re}(S_{vv}S_{vh}^*) & -\text{Im}(S_{vv}S_{vh}^*) \\ |S_{hv}|^2 & |S_{hh}|^2 & \text{Im}(S_{hv}S_{hh}^*) & -\text{Im}(S_{hv}S_{hh}^*) \\ 2\text{Re}(S_{vv}S_{hv}^*) & 2\text{Re}(S_{vh}S_{hh}^*) & \text{Re}(S_{vv}S_{hh}^* + S_{vh}S_{hv}^*) & -\text{Im}(S_{vv}S_{hh}^* - S_{vh}S_{hv}^*) \\ 2\text{Im}(S_{vv}S_{hv}^*) & 2\text{Im}(S_{vh}S_{hh}^*) & \text{Im}(S_{vv}S_{hh}^* + S_{vh}S_{hv}^*) & \text{Re}(S_{vv}S_{hh}^* - S_{vh}S_{hv}^*) \end{bmatrix}$$

The theory for construction of the phase matrix for an inhomogeneous medium has been developed for some time already [5, 7, 36]. Several factors are considered to generate the phase matrix like size, shape, orientation, volumetric density, etc. The approach used to generate the phase matrix in this study will be given in Chapter 5.

2.3 Radiative transfer equation

The radiative transfer equation for partially polarized waves in a discrete inhomogeneous medium should include both scattering and absorbing characteristic in the differential equation and can be written as [5]

$$\frac{dI}{dl} = -\kappa_e I + \frac{\kappa_e}{4\pi} \int_{4\pi} P_e I d\Omega + \kappa_a J_a \quad (2.15)$$

or

$$\frac{dI}{dl} = -\kappa_e I + \frac{\kappa_s}{4\pi} \int_{4\pi} P_s I d\Omega + \kappa_a J_a \quad (2.16)$$

Most of the studies to date have dealt with the special case of spherical particles. For these particles, or for non-spherical particles with random orientations, κ_e and κ_s reduce to scalars [37]. If this is so, it is convenient to convert the independent variable in (2.15) or (2.16) to optical thickness τ . Then, (2.15) and (2.16) reduce respectively to

$$\frac{dI}{d\tau} = -I + \frac{1}{4\pi} \int_{4\pi} P_e I d\Omega + (1 - \omega) J_a \quad (2.17)$$

and

$$\frac{dI}{d\tau} = -I + \frac{\omega}{4\pi} \int_{4\pi} P_s I d\Omega + (1 - \omega) J_a \quad (2.18)$$

where $\tau = \int \kappa_e dl$ and ω is the albedo, which is the ratio of κ_s to κ_e . It may be helpful to note that $P_e = \omega P_s$. The radiative transfer equation is formulated on the basis of energy balance. Thus, the phase changes of the scattered wave and its cross-correlation term are ignored in the solution of the transfer equation. Although the radiative transfer approach cannot account for phase effects in multiple scattering calculations, it does include phase effect in the phase function calculation and it accounts for higher order multiple scattering more effectively than the wave approach. It is assumed that there is no correlation between fields; hence addition of intensities is considered instead of addition of fields. In the radiative transfer formulation, the phase matrix characterizes the coupling of intensities in any direction due to scattering, and the extinction matrix describes the attenuation of specific intensity due to absorption and scattering.

2.4 Scattering from an inhomogeneous layer with irregular boundaries

For bounded media, scattering or reflection may occur at the boundary. Both incident and scattered intensities are needed in the boundary conditions. Therefore, it is necessary to split the intensity matrix into upward I^+ and downward I^- components and rewrite the transfer equation as two equations.

Consider the problem of a plane wave in air incident upon an inhomogeneous layer above the ground surface. The geometry of the scattering problem is depicted in Figure 2.2. The inhomogeneous layer is assumed to have such characteristics that the upward intensity I^+ and the downward intensity I^- satisfy the radiative transfer equation.

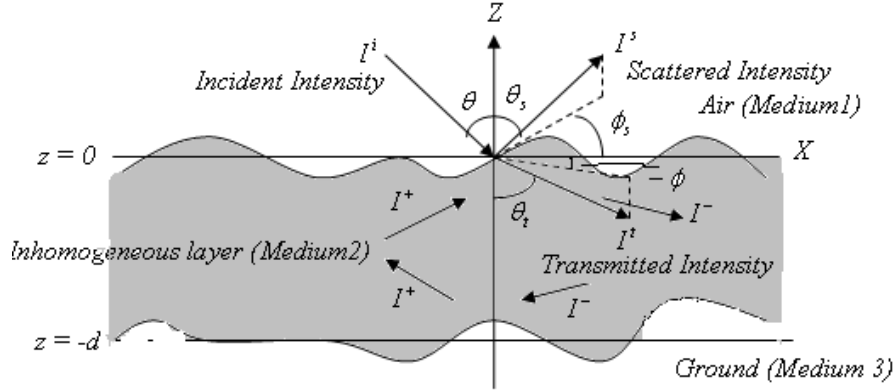


Figure 2.2 Scattering from an inhomogeneous layer above a homogeneous half space.

Upon re-writing (2.18) in terms of these intensities, the equations can be expressed as

$$\begin{aligned} \mu_s \frac{d}{dz} I^+(z, \mu_s, \phi_s) = & -\kappa_e I^+(z, \mu_s, \phi_s) + \frac{1}{4\pi} \int_0^{2\pi} \int_0^1 \kappa_s P_s(\mu_s, \mu, \phi_s - \phi) I^+(z, \mu_s, \phi_s) d\mu d\phi \\ & + \frac{1}{4\pi} \int_0^{2\pi} \int_0^1 \kappa_s P_s(\mu_s, -\mu, \phi_s - \phi) I^-(z, \mu, \phi) d\mu d\phi \end{aligned} \quad (2.19)$$

$$\mu_s \frac{d}{dz} I^-(z, \mu_s, \phi_s) = \kappa_e I^-(z, \mu_s, \phi_s) - \frac{1}{4\pi} \int_0^{2\pi} \int_0^1 \kappa_s P_s(-\mu_s, \mu, \phi_s - \phi) I^+(z, \mu_s, \phi_s) d\mu d\phi$$

$$-\frac{1}{4\pi} \int_0^{2\pi} \int_0^1 \kappa_s P_s(-\mu_s, -\mu, \phi_s - \phi) I^-(z, \mu, \phi) d\mu d\phi \quad (2.20)$$

where $\mu = \cos \theta$; $\mu_s = \cos \theta_s$; I^+, I^- are column vectors containing the four modified Stokes parameters and P_s is the phase matrix.

The explicit form of the phase matrices for the IEM model is given in next sections. The transfer equations given by (2.19) and (2.20) can be solved by using a numerical technique.

2.5 Emission model for an inhomogeneous layer

Consider the emission problem of an inhomogeneous irregular layer above a homogeneous half space (Figure 2.2). The incoherent source term is represented by the emitted intensity I^e due to the layer temperature profile T . The incoherent source term in (2.17), I^e , is included. I^e is given by

$$I^e = (1 - \omega) J_a = \frac{K}{\lambda^2} \epsilon_r T \quad (2.21)$$

where K is the Boltzmann constant, λ is the operating wavelength in the free space, and ϵ_r is the relative permittivity of the layer.

The intensity vectors consist of a vertically and a horizontally polarized component, i.e. only the first two Stokes parameters. Also, the layer temperature profile T is assumed independent of azimuthal angles.

The first point above is the consequence of the incoherent nature of natural emission which causes the third and the fourth Stokes parameters to vanish. This is because cross polarization of vertical and horizontal emission components is zero. The second point allows to

replace the elements of the phase matrix by their zeroth-order Fourier components in both the transfer equations and the associated boundary conditions.

2.6 Formulation of surface scattering matrices using the Integral Equation method

An appropriate description of the surface is required for all surface modeling. Two principal parameters characterize the surface: the standard deviation of height and correlation length which describe the degrees of vertical and horizontal roughness.

The problem of scattering from rough surfaces has been studied using low frequency (Small Perturbation Method, SPM) and high frequency (Kirchhoff) approximations. For rough surfaces with different scales of roughness, two-scale models combining the above two approximations were used. But, real rough surface may have a continuous scale of roughness and may not follow a two-scale model. On the other hand, as the scattering elements of rough surfaces present a complex geometry and are randomly distributed, their electromagnetic scattering involves complex interactions. The Integral Equation Method (IEM) combines the two approximations together and can be used to model surfaces with arbitrary roughness scales. At low frequencies, IEM reduces to the first-order SPM and at high frequencies; it reduces to the Kirchhoff term [3].

The IEM model was first developed to describe electromagnetic wave scattering for a randomly rough, perfectly conducting surface [38], and later, for a randomly rough dielectric surface [11]. The first complete version of the IEM model was developed and proposed by Fung [11], based on a more rigorous solution of a pair of integral equations governing the surface current. In this model, a simplifying assumption was made on the spectral form of the Green's function by ignoring the phase term. In particular, it was argued that the absolute value of the difference in the surface heights at two surface points appearing in the phase of the

Green's function can be ignored [39]. This argument was arrived at by noting that a) if the two points are close together, the difference in heights should be small for a continuous surface and b) if the two surface points are far apart, there should be a negligible amount of correlation between the two points and hence will not contribute significantly to the scattered power.

In IEM, for a given incident plane wave defined using \vec{E}^i and \vec{H}^i , the tangential \vec{E} and \vec{H} fields on the interface between two media are found by solving Electric Integral Field Equation (EFIE) and Magnetic Integral Field Equation (MFIE). Then, using the Stratton-Chu Radiation Integral, the far zone fields using the tangential fields at the dielectric interface is found. Once expressions for the scattered \vec{E} and \vec{H} fields have been derived, the average scattered power in a given direction is found by averaging the field quantities over various realizations of the rough surface where the realizations themselves are picked from various probability distributions of the surface. Most of the approximations made in the derivation are related to making the field quantities as independent of the local coordinates as possible.

The single backscattering coefficients from the IEM model are given by

$$\sigma_{pp}^0 = \frac{k^2}{2} \exp[-2k_z^2 \sigma^2] \sum_{n=1}^{\infty} \sigma^{2n} |I_{pp}^n|^2 \frac{W^n(-2k_x, 0)}{n!} \quad (2.22)$$

with

$$I_{pp}^n = (2k_z)^n f_{pp} \exp[-2k_z^2 \sigma^2] + \frac{1}{2} \{k_z^n [F_{pp}(-k_x, 0) + F_{pp}(k_x, 0)]\} \quad (2.23)$$

where pp denotes the polarization state and

$$f_{vv} = \frac{2R_v}{\cos(\theta_i)} \quad (2.24)$$

$$f_{hh} = \frac{-2R_h}{\cos(\theta_i)} \quad (2.25)$$

$$F_{vv}(-k_x, 0) + F_{vv}(k_x, 0) = \frac{2\sin^2(\theta_i)(1 + R_v)^2}{\cos(\theta_i)} \left[\left(1 - \frac{1}{\epsilon_s}\right) + \frac{\mu_T \epsilon_s - \sin^2(\theta_i) - \epsilon_s \cos^2(\theta_i)}{\epsilon_s^2 \cos^2(\theta_i)} \right] \quad (2.26)$$

$$F_{hh}(-k_x, 0) + F_{hh}(k_x, 0) = \frac{-2\sin^2(\theta_i)(1 + R_h)^2}{\cos(\theta_i)} \left[\left(1 - \frac{1}{\mu_T}\right) + \frac{\mu_T \epsilon_s - \sin^2(\theta_i) - \mu_T \cos^2(\theta_i)}{\mu_T^2 \cos^2(\theta_i)} \right] \quad (2.27)$$

In the above equations, θ_i is the angle of incidence, R_h and R_v are the horizontally and vertically polarized Fresnel reflection coefficients; ϵ_s and μ_T are the relative permittivity and permeability of the surface; σ is the standard deviation of the surface height; k is the wave number; $k_z = k \cos(\theta_i)$; $k_x = k \sin(\theta_i)$; and W^n is the Fourier transform of the n th power of a known surface correlation function which can be calculated by

$$W^n(K) = \int_0^\infty \rho^n(\xi) J_0(K\xi) \xi d\xi \quad (2.28)$$

where ρ is the surface correlation and J_0 is the Bessel function to the zeroth order.

More details about derivation are given in [3, 36]. In the above expression, f_{pp} is the Kirchoff's field coefficient and F_{pp} is the complementary field coefficient. The expression for the scattering coefficient involves a series and roughly the number of terms required for convergence is given by [3]

$$n = -1.47 + 16.96(k\sigma) - 15.71(k\sigma)^2 + 9.488(k\sigma)^3 - 1.47(k\sigma)^4 \quad (2.29)$$

where $(k\sigma)$ is the normalized standard deviation of the surface roughness. The construction of bistatic single-scatter scattering and transmission phase coefficient phase matrix is also given in detail in [36].

CHAPTER 3

FINITE-DIFFERENCE TIME-DOMAIN METHOD

All phenomena involving electromagnetic fields can be mathematically described by applying Maxwell's equations. Unfortunately, solving these equations analytically is often very difficult, and certain approximations have to be introduced to obtain a practical solution. Solutions to these equations have a long history, and a large variety of methods have been developed. The most satisfactory solution is the mathematically exact one. Analytical methods used for obtaining such solutions are: separation of variables, series expansion, conformal mapping and integral methods. However, these methods can be used only in the analysis of very specific field problems. In many practical situations, the complexity of the problem is simply too large for it to be solved analytically. In this case other analysis techniques need to be considered, such as numerical, graphical and experimental methods. Usually experimental solutions are very expensive, and graphical ones are not accurate enough. On the other hand, numerical methods are relatively inexpensive, and the obtained results are accurate to within the tolerance that can be arbitrarily preset. For those reasons, numerical methods represent very attractive tools for modeling and analysis of various electromagnetic problems. The Finite Difference Time-Domain (FDTD) method is a widely used computational technique for providing accurate full-wave analysis of electromagnetic phenomena.

3.1 Introduction to the Finite Difference Time-Domain (FDTD) method

The Finite-Difference Time-Domain Method (FDTD) is a Maxwell's equations solver [28, 29]. It has proven to be an effective technique of calculating the interaction of electromagnetic waves with bodies of different material, and complex geometries [31]. Also, FDTD is considered to be one of the most popular and robust means to implement engineering electromagnetics models [30].

In this chapter, the foundation of FDTD electromagnetic field analysis, the algorithm introduced by Kane Yee [29] is given. Yee chose a geometry for spatially sampling the electric and magnetic field vector components, which robustly represent both the differential and integral forms of Maxwell's equations. The description given here follows closely the one given in [40].

3.2 Maxwell's equations in three dimensions

Assume a region of space that has no electric or magnetic current sources, but may have materials that absorb electric or magnetic field energy. In this situation, the time-dependent Maxwell's equations are given in differential and integral form by

Faraday's law:

$$\frac{\partial \vec{B}}{\partial t} = -\nabla \times \vec{E} - \vec{M} \quad (3.1)$$

$$\frac{\partial}{\partial t} \iint_A \vec{B} \cdot d\vec{A} = -\oint_L \vec{E} \cdot d\vec{L} - \iint_A \vec{M} \cdot d\vec{A} \quad (3.2)$$

Ampere's law:

$$\frac{\partial \vec{D}}{\partial t} = \nabla \times \vec{H} - \vec{J} \quad (3.3)$$

$$\frac{\partial}{\partial t} \iint_A \vec{D} \cdot d\vec{A} = \oint_L \vec{H} \cdot d\vec{L} - \iint_A \vec{J} \cdot d\vec{A} \quad (3.4)$$

Gauss' law for the electric field:

$$\nabla \cdot \vec{D} = 0 \quad (3.5)$$

$$\oiint_A \vec{D} \cdot d\vec{A} = 0 \quad (3.6)$$

Gauss' law for the magnetic field:

$$\nabla \cdot \vec{B} = 0 \quad (3.7)$$

$$\oiint_A \vec{B} \cdot d\vec{A} = 0 \quad (3.8)$$

In linear, isotropic, nondispersive materials, to relate \vec{D} to \vec{E} and \vec{B} to \vec{H} the following expressions can be used:

$$\vec{D} = \epsilon \vec{E} = \epsilon_r \epsilon_0 \vec{E} \quad \vec{B} = \mu \vec{H} = \mu_r \mu_0 \vec{H} \quad (3.9)$$

The sources \vec{J} and \vec{M} can act as independent sources of \vec{E} - and \vec{H} -field energy, \vec{J}_{source} and \vec{M}_{source} . Materials with isotropic, nondispersive electric and magnetic losses that attenuate \vec{E} - and \vec{H} -fields via conversion to heat energy can be involved. This yields

$$\vec{J} = \vec{J}_{source} + \sigma \vec{E} \quad \vec{M} = \vec{M}_{source} + \rho' \vec{H} \quad (3.10)$$

where σ and ρ' are electric conductivity (Siemens/meter) and the equivalent magnetic loss (ohms/meter), respectively.

By substituting (3.9) and (3.10) into (3.1) and (3.3), the Maxwell's curl equations in linear, isotropic, nondispersive, lossy materials are given by:

$$\frac{\partial \vec{H}}{\partial t} = -\frac{1}{\mu} \nabla \times \vec{E} - \frac{1}{\mu} (\vec{M}_{source} + \rho' \vec{H}) \quad (3.11)$$

$$\frac{\partial \vec{E}}{\partial t} = \frac{1}{\epsilon} \nabla \times \vec{H} - \frac{1}{\epsilon} (\vec{J}_{source} + \sigma \vec{E}) \quad (3.12)$$

The vector components of the curl operators of (3.11) and (3.12) in Cartesian coordinates are represented by the following system of six coupled scalar equations:

$$\frac{\partial H_x}{\partial t} = \frac{1}{\mu} \left(\frac{\partial E_y}{\partial z} - \frac{\partial E_z}{\partial y} - (M_{source_x} + \rho' H_x) \right) \quad (3.13)$$

$$\frac{\partial H_y}{\partial t} = \frac{1}{\mu} \left(\frac{\partial E_z}{\partial x} - \frac{\partial E_x}{\partial z} - (M_{source_y} + \rho' H_y) \right) \quad (3.14)$$

$$\frac{\partial H_z}{\partial t} = \frac{1}{\mu} \left(\frac{\partial E_x}{\partial y} - \frac{\partial E_y}{\partial x} - (M_{source_z} + \rho' H_z) \right) \quad (3.15)$$

$$\frac{\partial E_x}{\partial t} = \frac{1}{\epsilon} \left(\frac{\partial H_z}{\partial y} - \frac{\partial H_y}{\partial z} - (J_{source_x} + \sigma E_x) \right) \quad (3.16)$$

$$\frac{\partial E_y}{\partial t} = \frac{1}{\epsilon} \left(\frac{\partial H_x}{\partial z} - \frac{\partial H_z}{\partial x} - (J_{source_y} + \sigma E_y) \right) \quad (3.17)$$

$$\frac{\partial E_z}{\partial t} = \frac{1}{\epsilon} \left(\frac{\partial H_y}{\partial x} - \frac{\partial H_x}{\partial y} - (J_{source_z} + \sigma E_z) \right) \quad (3.18)$$

The system of six coupled partial differential equations of (3.13) to (3.18) forms the basis of FDTD numerical algorithm for electromagnetic wave interactions with general three-dimensional objects. The FDTD algorithm need not explicitly enforce the Gauss' law relations indicating zero free electric and magnetic charge, (3.5) to (3.8); because these relations are theoretically a direct consequence of the curl equations. Nevertheless, the FDTD space lattice must be structured so that the Gauss' law relations are implicit in the positions of the \vec{E} and \vec{H} components, and in the numerical space-derivative operations upon these components that model the action of the curl operator.

3.3 The Yee algorithm

Yee originated a set of finite-difference equations for the time-dependent Maxwell's curl equations system of (3.13) and (3.18) for the lossless materials case $\rho' = 0$ and $\sigma = 0$ [29].

The Yee algorithm solves for both electric and magnetic fields in time and space using the coupled Maxwell's curl equations, instead of solving for the electric field alone (or the magnetic field alone) with a wave equation.

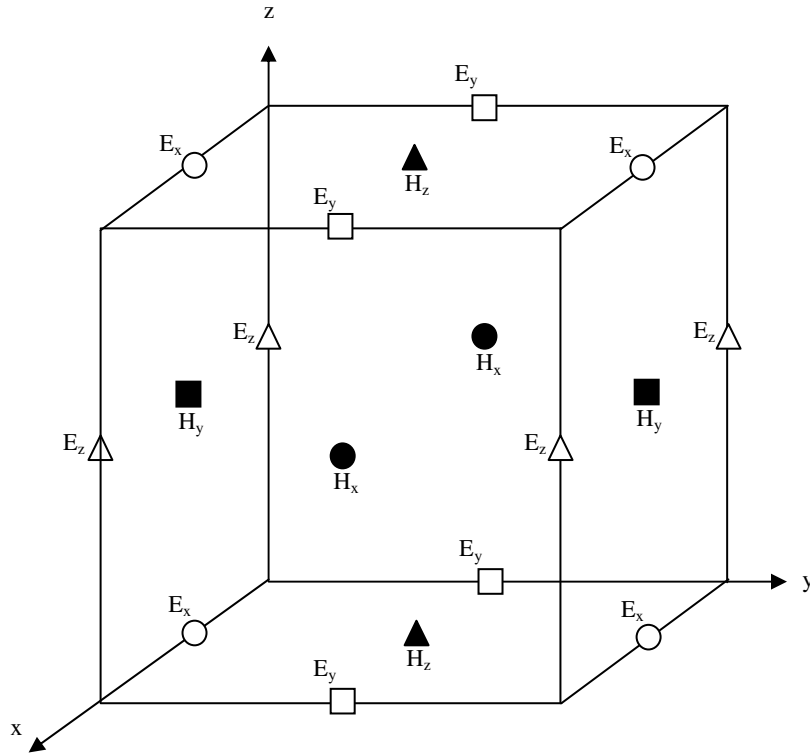


Figure 3.1 Positions of field components. The \vec{E} -components are in the middle of edges and the \vec{H} -components are in the center of the faces.

The Yee algorithm centers its \vec{E} and \vec{H} components in three-dimensional space so that every \vec{E} component is surrounded by four circulating \vec{H} components, and every \vec{H} component is surrounded by four circulating \vec{E} components (Fig. 3.1).

This provides a simple picture of three-dimensional space being filled by an interlinked array of Faraday's law and Ampere's law contours. It is possible to identify Yee \vec{E} components associated with displacement current flux linking \vec{H} loops, as well as \vec{H} components associated with magnetic flux linking \vec{E} loops. Actually, the Yee algorithm simultaneously simulates the pointwise differential form and the macroscopic integral form of Maxwell's equations. Another features of the Yee space lattice are : a) the finite-difference expressions for the space derivatives used in the curl operators are central-difference in nature and second-order accurate; b) continuity of tangential \vec{E} and \vec{H} is naturally maintained across an interface of dissimilar materials if the interface is parallel to one of the lattice coordinate axes. For this case, there is no need to specially enforce field boundary conditions at the interface. At the beginning of the problem, the material permittivity and permeability at each field component location is specified. This yields a stepped or "staircase" approximation of the surface and internal geometry of the structure, with a space resolution set by the size of the lattice unit cell; and c) the location of the \vec{E} and \vec{H} components in the Yee space lattice and the central- difference operations on these components implicitly enforce the two Gauss' law relations. Consequently, the Yee mesh is divergence-free with respect to its \vec{E} and \vec{H} fields in the absence of free electric and magnetic charge.

The Yee algorithm also centers its \vec{E} and \vec{H} components in time, in what is termed as a leapfrog arrangement (Fig. 3.2). All of the \vec{E} computations in the modeled space are completed and stored in memory for a particular time point using previously stored \vec{H} data. Afterward, all of the \vec{H} computations in the space are completed and stored in memory using the \vec{E} data just computed. The cycle starts again with the recomputation of the \vec{E} components based on the recently obtained \vec{H} . This process carries on until time-stepping is concluded.

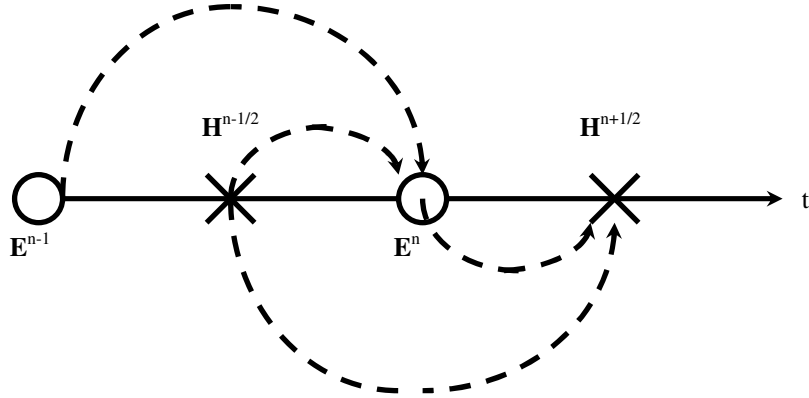


Figure 3.2 Leapfrog time integration.

3.4 Finite differences and notation

In [29] Yee introduced the notation shown in table 3.1 for space points and functions of space and time in a uniform, rectangular lattice.

Table 3.1 Location of the different fields in the Yee cell

Element	Location
$E_x^n(i, j, k)$	$x = \left(i + \frac{1}{2}\right)\Delta x, y = j\Delta y, z = k\Delta z$
$E_y^n(i, j, k)$	$x = i\Delta x, y = \left(j + \frac{1}{2}\right)\Delta y, z = k\Delta z$
$E_z^n(i, j, k)$	$x = i\Delta x, y = j\Delta y, z = \left(k + \frac{1}{2}\right)\Delta z$
$E_z^n(i, j, k)$	$x = i\Delta x, y = \left(j + \frac{1}{2}\right)\Delta y, z = \left(k + \frac{1}{2}\right)\Delta z$
$H_y^n(i, j, k)$	$x = \left(i + \frac{1}{2}\right)\Delta x, y = j\Delta y, z = \left(k + \frac{1}{2}\right)\Delta z$
$H_z^n(i, j, k)$	$x = \left(i + \frac{1}{2}\right)\Delta x, y = \left(j + \frac{1}{2}\right)\Delta y, z = k\Delta z$

The lattice space increments in the x , y , and z coordinate directions are denoted by Δx , Δy , and Δz respectively; and i , j , and k are integers. Hence, any function u of space and time evaluated at a discrete point in the grid and at a discrete point in time is denoted as

$$u(i \Delta x, j \Delta y, k \Delta z, n \Delta t) = u_{i,j,k}^n \quad (3.19)$$

where Δt is the time increment, assumed uniform over the observation interval, and n is an integer.

Yee made use of centered finite-difference expressions for the space and time derivatives that are both simply programmed and second-order accurate in the space and time increments. An expression for the first partial space derivative of u in the x -direction, evaluated at the fixed time $t_n = n \Delta t$ is given by:

$$\frac{\partial u}{\partial x}(i \Delta x, j \Delta y, k \Delta z, n \Delta t) = \frac{u_{i+\frac{1}{2},j,k}^n - u_{i-\frac{1}{2},j,k}^n}{\Delta x} + O[(\Delta x)^2] \quad (3.20)$$

A $\pm 1/2$ increment in the i subscript (x -coordinate) of u denotes a space finite-difference over $\pm(1/2) \Delta x$. A second-order accurate central differencing is used. Data for the central differences are taken to the right and left of the observation point by only $\Delta x/2$, rather than a full Δx .

This notation is chosen to interleave \vec{E} and \vec{H} components in the space lattice at intervals of $\Delta x/2$. The difference of two adjacent \vec{E} components, separated by Δx and located $\pm(1/2)\Delta x$ on either side of an \vec{H} component, would be used to provide a numerical approximation for $\partial \vec{E} / \partial x$ to permit stepping the \vec{H} component in time. For the sake of completeness, it should be added that a numerical approximation analogous to (3.20) for $\partial u / \partial y$

or $\partial u / \partial z$ can be written simply by incrementing the j or k subscript of u by $\pm(1/2)\Delta y$ or $\pm(1/2)\Delta z$, respectively.

The expression for the first time partial derivative of u , evaluated at the fixed space point (i, j, k) , follows by analogy:

$$\frac{\partial u}{\partial t}(i \Delta x, j \Delta y, k \Delta z, n \Delta t) = \frac{u_{i,j,k}^{n+\frac{1}{2}} - u_{i,j,k}^{n-\frac{1}{2}}}{\Delta t} + O[(\Delta t)^2] \quad (3.21)$$

Now the $\pm 1/2$ increment is in the n superscript (time coordinate) of u , denoting a time finite- difference over $\pm(1/2)\Delta t$. This notation was chosen to interleave the \vec{E} and \vec{H} components in time at intervals of $(1/2)\Delta t$ for purposes of implementing a leapfrog algorithm.

3.5 Finite differences expressions for Maxwell's equations in three dimensions

The ideas and notation shown above are applied to achieve a numerical approximation of the Maxwell's curl equations in three dimensions given by (3.13) to (3.18). The E_x field-component is given by (3.16):

$$\frac{\partial E_x}{\partial t} = \frac{1}{\epsilon} \left(\frac{\partial H_z}{\partial y} - \frac{\partial H_y}{\partial z} - (J_{source_x} + \sigma E_x) \right)$$

Consider a typical substitution of central differences for the time and space derivatives in (3.16), for example, at $E_x\left(i, j + \frac{1}{2}, k + \frac{1}{2}, n\right)$. Initially

$$\begin{aligned}
& \frac{E_x|_{i,j+\frac{1}{2},k+\frac{1}{2}}^{n+\frac{1}{2}} - E_x|_{i,j+\frac{1}{2},k+\frac{1}{2}}^{n-\frac{1}{2}}}{\Delta t} = \\
& \frac{1}{\mathcal{E}_{i,j+\frac{1}{2},k+\frac{1}{2}}^{n+\frac{1}{2}}} \cdot \left(\frac{H_z|_{i,j+\frac{1}{2},k+\frac{1}{2}}^n - H_z|_{i,j,k+\frac{1}{2}}^n}{\Delta y} - \frac{H_y|_{i,j+\frac{1}{2},k+1}^n - H_y|_{i,j+\frac{1}{2},k}^n}{\Delta z} \right. \\
& \quad \left. - J_{source_x}|_{i,j+\frac{1}{2},k+\frac{1}{2}}^n - \sigma_{i,j+\frac{1}{2},k+\frac{1}{2}} E_x|_{i,j+\frac{1}{2},k+\frac{1}{2}}^n \right) \quad (3.22)
\end{aligned}$$

All field quantities in the right hand side are evaluated at time-step n , including the electric field E_x appearing due to the material conductivity σ . Since E_x values at time-step n are not assumed to be stored in the computer's memory (only the previous values of E_x at time-step $n - \frac{1}{2}$ are assumed to be in memory), some way to estimate such terms is needed. One way is using what is called a semi-implicit approximation:

$$E_x|_{i,j+\frac{1}{2},k+\frac{1}{2}}^n = \frac{E_x|_{i,j+\frac{1}{2},k+\frac{1}{2}}^{n+\frac{1}{2}} + E_x|_{i,j+\frac{1}{2},k+\frac{1}{2}}^{n-\frac{1}{2}}}{2} \quad (3.23)$$

The E_x values at time-step n are assumed to be simply the arithmetic average of the stored values of E_x at time-step $n - \frac{1}{2}$, and the yet-to-be-computed new values of E_x at time-step $n + \frac{1}{2}$. By substitution of (3.23) into (3.22) after multiplying both sides by Δt , the following is obtained

$$\begin{aligned}
& E_x \big|_{i,j+\frac{1}{2},k+\frac{1}{2}}^{n+\frac{1}{2}} - E_x \big|_{i,j+\frac{1}{2},k+\frac{1}{2}}^{n-\frac{1}{2}} = \\
& \frac{\Delta t}{\varepsilon_{i,j+\frac{1}{2},k+\frac{1}{2}}} \cdot \left(\frac{H_z \big|_{i,j+1,k+\frac{1}{2}}^n - H_z \big|_{i,j,k+\frac{1}{2}}^n}{\Delta y} - \frac{H_y \big|_{i,j+\frac{1}{2},k+1}^n - H_y \big|_{i,j+\frac{1}{2},k}^n}{\Delta z} \right. \\
& \left. - J_{source_x} \big|_{i,j+\frac{1}{2},k+\frac{1}{2}}^n - \sigma_{i,j+\frac{1}{2},k+\frac{1}{2}} \cdot \left(\frac{E_x \big|_{i,j+\frac{1}{2},k+\frac{1}{2}}^{n+\frac{1}{2}} - E_x \big|_{i,j+\frac{1}{2},k+\frac{1}{2}}^{n-\frac{1}{2}}}{\Delta t} \right) \right) \quad (3.24)
\end{aligned}$$

The terms $E_x \big|_{i,j+\frac{1}{2},k+\frac{1}{2}}^{n+\frac{1}{2}}$ and $E_x \big|_{i,j+\frac{1}{2},k+\frac{1}{2}}^{n-\frac{1}{2}}$ appear on both sides of (3.24). Collecting all

terms of these two types and isolating $E_x \big|_{i,j+\frac{1}{2},k+\frac{1}{2}}^{n+\frac{1}{2}}$ on the left-hand side yields

$$\begin{aligned}
& \left(1 + \frac{\sigma_{i,j+\frac{1}{2},k+\frac{1}{2}} \Delta t}{2\varepsilon_{i,j+\frac{1}{2},k+\frac{1}{2}}} \right) E_x \big|_{i,j+\frac{1}{2},k+\frac{1}{2}}^{n+\frac{1}{2}} = \left(1 - \frac{\sigma_{i,j+\frac{1}{2},k+\frac{1}{2}} \Delta t}{2\varepsilon_{i,j+\frac{1}{2},k+\frac{1}{2}}} \right) E_x \big|_{i,j+\frac{1}{2},k+\frac{1}{2}}^{n-\frac{1}{2}} + \\
& \frac{\Delta t}{\varepsilon_{i,j+\frac{1}{2},k+\frac{1}{2}}} \cdot \left(\frac{H_z \big|_{i,j+1,k+\frac{1}{2}}^n - H_z \big|_{i,j,k+\frac{1}{2}}^n}{\Delta y} - \frac{H_y \big|_{i,j+\frac{1}{2},k+1}^n - H_y \big|_{i,j+\frac{1}{2},k}^n}{\Delta z} \right. \\
& \left. - J_{source_x} \big|_{i,j+\frac{1}{2},k+\frac{1}{2}}^n \right) \quad (3.25)
\end{aligned}$$

Both sides are divided by $\left(1 + \frac{\sigma_{i,j+\frac{1}{2},k+\frac{1}{2}} \Delta t}{2\varepsilon_{i,j+\frac{1}{2},k+\frac{1}{2}}} \right)$. Hence, the desired explicit time-stepping

relation for $E_x \big|_{i,j+\frac{1}{2},k+\frac{1}{2}}^{n+\frac{1}{2}}$ is:

$$\begin{aligned}
E_x \Big|_{i,j+\frac{1}{2},k+\frac{1}{2}}^{n+\frac{1}{2}} &= \left(\frac{1 - \frac{\sigma_{i,j+\frac{1}{2},k+\frac{1}{2}} \Delta t}{2\mathcal{E}_{i,j+\frac{1}{2},k+\frac{1}{2}}}}{1 + \frac{\sigma_{i,j+\frac{1}{2},k+\frac{1}{2}} \Delta t}{2\mathcal{E}_{i,j+\frac{1}{2},k+\frac{1}{2}}}} \right) E_x \Big|_{i,j+\frac{1}{2},k+\frac{1}{2}}^{n-\frac{1}{2}} + \left(\frac{\frac{\Delta t}{\mathcal{E}_{i,j+\frac{1}{2},k+\frac{1}{2}}}}{1 + \frac{\sigma_{i,j+\frac{1}{2},k+\frac{1}{2}} \Delta t}{2\mathcal{E}_{i,j+\frac{1}{2},k+\frac{1}{2}}}} \right) \\
&\quad \left(\frac{H_z \Big|_{i,j+1,k+\frac{1}{2}}^n - H_z \Big|_{i,j,k+\frac{1}{2}}^n}{\Delta y} - \frac{H_y \Big|_{i,j+\frac{1}{2},k+1}^n - H_y \Big|_{i,j+\frac{1}{2},k}^n}{\Delta z} \right. \\
&\quad \left. - J_{source_x} \Big|_{i,j+\frac{1}{2},k+\frac{1}{2}}^n \right)
\end{aligned} \tag{3.26}$$

The semi-implicit assumption of (3.23) yields numerically stable and accurate results for values of σ from zero to infinity [31]. The term of this type introduced on the right-hand side of (3.24) can be grouped with a like term on the left-hand side and then solved explicitly.

Similarly, finite-difference expressions based on Yee's algorithm for the E_y and E_z field components, given by Maxwell's equations (3.17) and (3.18) respectively, can be derived. The time-stepping expressions for the E_y and E_z are then

$$\begin{aligned}
E_y \Big|_{i-\frac{1}{2},j+1,k+\frac{1}{2}}^{n+\frac{1}{2}} &= \left(\frac{1 - \frac{\sigma_{i-\frac{1}{2},j+1,k+\frac{1}{2}} \Delta t}{2\mathcal{E}_{i-\frac{1}{2},j+1,k+\frac{1}{2}}}}{1 + \frac{\sigma_{i-\frac{1}{2},j+1,k+\frac{1}{2}} \Delta t}{2\mathcal{E}_{i-\frac{1}{2},j+1,k+\frac{1}{2}}}} \right) E_y \Big|_{i-\frac{1}{2},j+1,k+\frac{1}{2}}^{n-\frac{1}{2}} + \left(\frac{\frac{\Delta t}{\mathcal{E}_{i-\frac{1}{2},j+1,k+\frac{1}{2}}}}{1 + \frac{\sigma_{i-\frac{1}{2},j+1,k+\frac{1}{2}} \Delta t}{2\mathcal{E}_{i-\frac{1}{2},j+1,k+\frac{1}{2}}}} \right) \\
&\quad \left(\frac{H_x \Big|_{i-\frac{1}{2},j+1,k+1}^n - H_x \Big|_{i-\frac{1}{2},j+1,k}^n}{\Delta z} - \frac{H_z \Big|_{i,j+1,k+\frac{1}{2}}^n - H_z \Big|_{i-1,j+1,k+\frac{1}{2}}^n}{\Delta x} \right. \\
&\quad \left. - J_{source_y} \Big|_{i-\frac{1}{2},j+1,k+\frac{1}{2}}^n \right)
\end{aligned} \tag{3.27}$$

$$\begin{aligned}
E_z \Big|_{i-\frac{1}{2}, j+\frac{1}{2}, k+1}^{n+\frac{1}{2}} &= \left(\frac{1 - \frac{\sigma_{i-\frac{1}{2}, j+\frac{1}{2}, k+1} \Delta t}{2\epsilon_{i-\frac{1}{2}, j+\frac{1}{2}, k+1}}}{1 + \frac{\sigma_{i-\frac{1}{2}, j+\frac{1}{2}, k+1} \Delta t}{2\epsilon_{i-\frac{1}{2}, j+\frac{1}{2}, k+1}}} \right) E_z \Big|_{i-\frac{1}{2}, j+\frac{1}{2}, k+1}^{n-\frac{1}{2}} + \left(\frac{\frac{\Delta t}{\epsilon_{i-\frac{1}{2}, j+\frac{1}{2}, k+1}}}{1 + \frac{\sigma_{i-\frac{1}{2}, j+\frac{1}{2}, k+1} \Delta t}{2\epsilon_{i-\frac{1}{2}, j+\frac{1}{2}, k+1}}} \right) \\
&\quad \left(\frac{H_y \Big|_{i, j+\frac{1}{2}, k+1}^n - H_y \Big|_{i-1, j+\frac{1}{2}, k+1}^n}{\Delta x} - \frac{H_x \Big|_{i-\frac{1}{2}, j+1, k+1}^n - H_x \Big|_{i-\frac{1}{2}, j, k+1}^n}{\Delta y} \right. \\
&\quad \left. - J_{source_x} \Big|_{i-\frac{1}{2}, j+\frac{1}{2}, k+1}^n \right)
\end{aligned} \tag{3.28}$$

Likewise, finite-difference equations for (3.13) to (3.15) to time-step H_x , H_y and H_z can be derived, using a semi-implicit procedure analogous to (3.23). A magnetic loss term is represented by $\rho'H$ on the right-hand side of each equation. This yields three equations having a form similar to that of the \vec{E} equations. Hence, the following time-stepping expression for the H_x component located at the upper right corner of the unit cell can be obtained:

$$\begin{aligned}
H_x \Big|_{i-\frac{1}{2}, j+1, k+1}^{n+1} &= \left(\frac{1 - \frac{\rho'_{i-\frac{1}{2}, j+1, k+1} \Delta t}{2\mu_{i-\frac{1}{2}, j+1, k+1}}}{1 + \frac{\rho'_{i-\frac{1}{2}, j+1, k+1} \Delta t}{2\mu_{i-\frac{1}{2}, j+1, k+1}}} \right) H_x \Big|_{i-\frac{1}{2}, j+1, k+1}^n + \left(\frac{\frac{\Delta t}{\mu_{i-\frac{1}{2}, j+1, k+1}}}{1 + \frac{\rho'_{i-\frac{1}{2}, j+1, k+1} \Delta t}{2\mu_{i-\frac{1}{2}, j+1, k+1}}} \right) \\
&\quad \left(\frac{E_y \Big|_{i-\frac{1}{2}, j+1, k+\frac{3}{2}}^{n+\frac{1}{2}} - E_y \Big|_{i-\frac{1}{2}, j+1, k+\frac{1}{2}}^{n+\frac{1}{2}}}{\Delta z} - \frac{E_z \Big|_{i-\frac{1}{2}, j+\frac{3}{2}, k+1}^{n+\frac{1}{2}} - E_z \Big|_{i-\frac{1}{2}, j+\frac{1}{2}, k+1}^{n+\frac{1}{2}}}{\Delta y} \right. \\
&\quad \left. - M_{source_x} \Big|_{i-\frac{1}{2}, j+1, k+1}^{n+\frac{1}{2}} \right)
\end{aligned} \tag{3.29}$$

Similarly, the time-stepping expressions for the H_y and H_z components, located at the upper front corner and the right front corner of the unit cell, respectively, can be represented as:

$$\begin{aligned}
H_y|_{i,j+\frac{1}{2},k+1}^{n+1} &= \left(\frac{1 - \frac{\rho'_{i,j+\frac{1}{2},k+1} \Delta t}{2\mu_{i,j+\frac{1}{2},k+1}}}{1 + \frac{\rho'_{i,j+\frac{1}{2},k+1} \Delta t}{2\mu_{i,j+\frac{1}{2},k+1}}} \right) H_y|_{i,j+\frac{1}{2},k+1}^n + \left(\frac{\frac{\Delta t}{\mu_{i,j+\frac{1}{2},k+1}}}{1 + \frac{\rho'_{i,j+\frac{1}{2},k+1} \Delta t}{2\mu_{i,j+\frac{1}{2},k+1}}} \right) \\
&\quad \left(\frac{E_z|_{i+\frac{1}{2},j+\frac{1}{2},k+1}^{n+\frac{1}{2}} - E_z|_{i-\frac{1}{2},j+\frac{1}{2},k+1}^{n+\frac{1}{2}}}{\Delta x} - \frac{E_x|_{i,j+\frac{1}{2},k+\frac{3}{2}}^{n+\frac{1}{2}} - E_x|_{i,j+\frac{1}{2},k+\frac{1}{2}}^{n+\frac{1}{2}}}{\Delta z} \right. \\
&\quad \left. - M_{source_x}|_{i,j+\frac{1}{2},k+1}^{n+\frac{1}{2}} \right)
\end{aligned} \tag{3.30}$$

and

$$\begin{aligned}
H_z|_{i,j+1,k+\frac{1}{2}}^{n+1} &= \left(\frac{1 - \frac{\rho'_{i,j+1,k+\frac{1}{2}} \Delta t}{2\mu_{i,j+1,k+\frac{1}{2}}}}{1 + \frac{\rho'_{i,j+1,k+\frac{1}{2}} \Delta t}{2\mu_{i,j+1,k+\frac{1}{2}}}} \right) H_z|_{i,j+1,k+\frac{1}{2}}^n + \left(\frac{\frac{\Delta t}{\mu_{i,j+\frac{1}{2},k+\frac{1}{2}}}}{1 + \frac{\rho'_{i,j+1,k+\frac{1}{2}} \Delta t}{2\mu_{i,j+1,k+\frac{1}{2}}}} \right) \\
&\quad \left(\frac{E_x|_{i,j+\frac{3}{2},k+\frac{1}{2}}^{n+\frac{1}{2}} - E_x|_{i,j+\frac{1}{2},k+\frac{1}{2}}^{n+\frac{1}{2}}}{\Delta y} - \frac{E_y|_{i+\frac{1}{2},j+1,k+\frac{1}{2}}^{n+\frac{1}{2}} - E_y|_{i-\frac{1}{2},j+1,k+\frac{1}{2}}^{n+\frac{1}{2}}}{\Delta x} \right. \\
&\quad \left. - M_{source_x}|_{i,j+1,k+\frac{1}{2}}^{n+\frac{1}{2}} \right)
\end{aligned} \tag{3.31}$$

respectively.

In conclusion, with the system of finite-difference expressions given by (3.26)-(3.31), the new value of an electromagnetic field vector component at any lattice point depends only on its previous value, the previous values of the components of the other field vector at adjacent points, and the known electric and magnetic current sources.

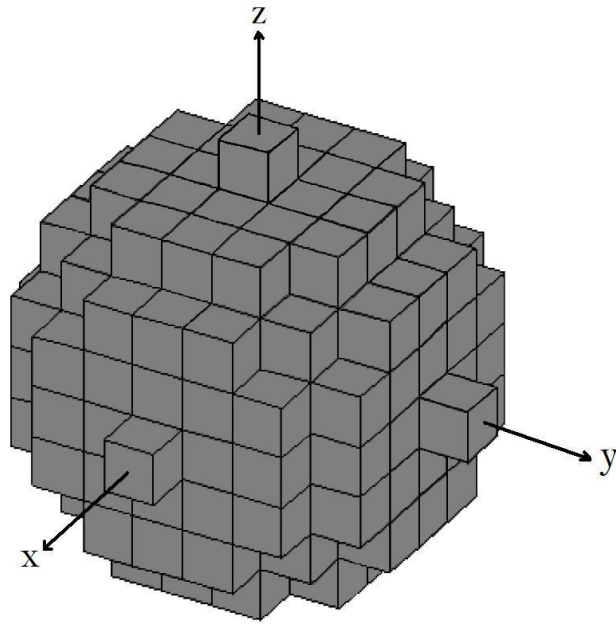


Figure 3.3 Staircased sphere in cubical Yee cells.

For illustrations purposes of a discretized object, in Figure 3.3 a sphere is approximated using cubical Yee cells, with the staircasing of the sphere surface shown clearly.

CHAPTER 4

NUMERICAL COMPUTATION OF EMISSION FROM FINITE-SIZE OBJECTS

4.1 Emission theory

It is well known that all matter radiates electromagnetic energy [41]. The radiation is a consequence of the interaction between the atoms and the molecules in the material. A material also may absorb and/or reflect energy incident upon it. When in thermodynamic equilibrium with its environment, a material absorbs and radiates energy at the same rate. A blackbody is defined as an ideal material that absorbs all of the incident radiation, reflecting none. Since energy absorbed by a material would increase its temperature if no energy were emitted, a perfect absorber is also a perfect emitter. The blackbody radiation spectrum is given by Planck's radiation law, which was formulated in the basis of the quantum theory of matter. This spectrum is used as a reference against which the radiation spectra of real bodies at the same physical temperature are compared. The spectral, polarization, and angular variations of the radiation emitted, absorbed, and scattered by a medium are governed by the geometrical configuration of the surface and interior of the medium, and by the spatial distributions of its dielectric and temperature.

Radiometry is the measurement of electromagnetic radiation. A microwave radiometer is a highly sensitive receiver capable of measuring low levels of microwave radiation. When a scene, such as terrain, is observed by a microwave radiometer, the radiation received by the antenna is partly due to self-emission by the scene and partly due to reflected radiation originating from the surroundings, such as the atmosphere. Through proper choice of the

radiometer parameters (wavelength, polarization, and viewing angle), it is sometimes possible to establish useful relations between magnitude of the energy received by the radiometer and specific terrestrial or atmospheric parameters of interest. For example, observations of bare soil surfaces have shown that the radiometric response of the 20-30 cm wavelength range is influenced strongly by the soil moisture content [42]. Such dependence can be used over large areas to remotely map soil moisture content, an important physical parameter in many hydrological, agricultural, and meteorological applications.

The science of microwave radiometry is also referred as passive microwave remote sensing, in contrast to radar, which is known as active microwave remote sensing. Numerous investigations have been conducted to evaluate the use of passive microwave sensors for meteorological, hydrological, oceanographic, and military applications.

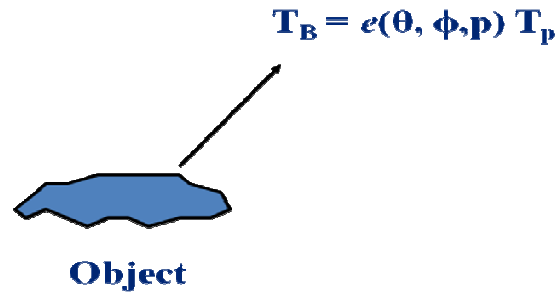


Figure 4.1 The brightness temperature of an object is related to its physical temperature by its emissivity.

Every object with a physical temperature above absolute zero radiates energy. The amount of energy radiated is usually represented by an equivalent temperature T_B , better known as brightness temperature (Fig. 4.1), and it is defined as

$$T_B(\theta, \phi, p) = \epsilon(\theta, \phi, p) T_p \quad (4.1)$$

where:

T_p : Physical temperature

$e(\theta, \phi, p)$: Emissivity

θ, ϕ : Elevation and azimuth angles

p : Polarization (v,h)

Hence, when analyzing the radiation from a finite-size object, a parameter to consider is the emissivity, which is the ratio of energy radiated by a particular material to energy radiated by a black body.

This chapter presents a method to numerically compute the emissivity from a finite size object. In [43] the significance of the equation obtained for the generalized Kirchhoff's law for a finite-size anisotropic medium is the fact that it relates the thermal emission from the original object to the absorption cross section of the “complementary” object, therefore relating a passive emission problem to an active scattering problem. Hence, although the purpose is to model the emission from an object, a numerical method can be used to simulate the interaction of a plane wave and the object and hence find the absorption and scattering properties of the object.

Before the emissivity of a finite-size object was computed, several tests were conducted in order to establish the accuracy of the FDTD approach to compute the scattered electromagnetic fields. The tests consisted of comparing the FDTD results with analytical results as well as published results using a different numerical method.

4.2 Validation of FDTD results by comparison with analytical results using Mie series solutions

One of the tests was the comparison of scattered fields of a dielectric sphere. A sphere is used because the scattered fields from a sphere due to a plane wave incidence have analytical

solutions. The solutions are usually called Mie series solutions. Therefore, a plane wave impinging on a sphere was simulated in the FDTD approach, as shown in Fig. 4.2. The parameters of the sphere are given in table 4.1, where λ_0 is the wavelength of the incident wave in free space. Table 4.2 shows the parameters of the incident plane wave as well as the scattered fields. The term range refers to the distance, from the center of the sphere, at which the scattered fields values were computed.

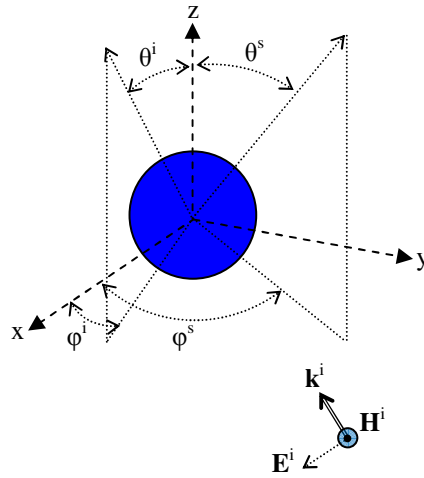


Figure 4.2 Configuration for simulation of plane wave impinging on a dielectric sphere.

Table 4.1 Parameters of object used in FDTD simulation of plane wave impinging on dielectric sphere.

Parameter	Value
Relative permittivity	3.15
Conductivity	0.02921 S/m
Radius	1 mm ($0.1167 \lambda_0$)

Table 4.2 Parameters of incident plane wave and scattered field.

Parameter	Value
Polarization	Vertical
Incident field elevation angle	$\theta^i = 89.07^\circ$
Incident field azimuth angle	$\phi^i = 0.0^\circ$
Scattered field azimuth angle	$\phi^s = 1.79^\circ$
Frequency	35 GHz
Range	2.407996 mm ($0.2809\lambda_0$) from center of sphere

Figure 4.3 shows the values of both \vec{E} and \vec{H} fields, computed with FDTD approach and Mie series solutions. The values of the components of \vec{H} are normalized by $|\vec{H}_{inc}|$. A good agreement can be observed.

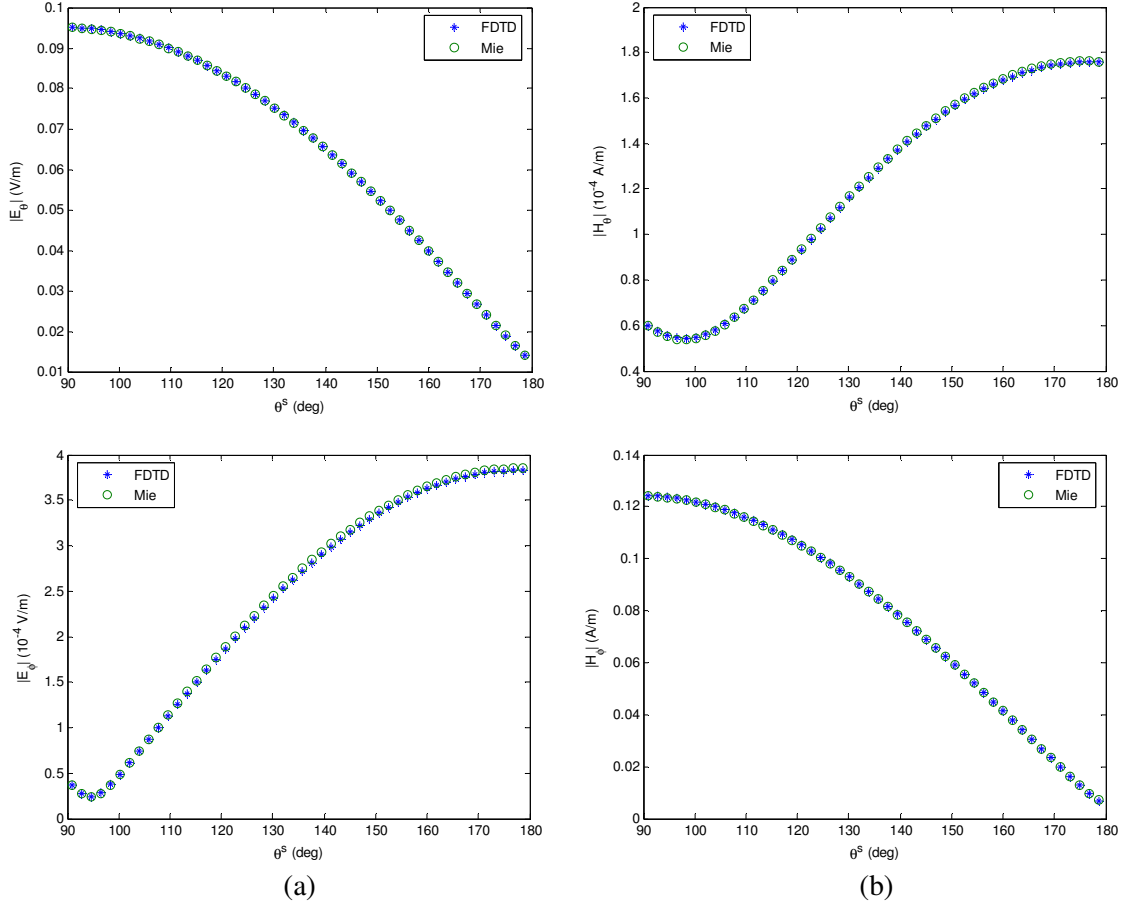


Figure 4.3 Comparison of scattered field values obtained by using FDTD and Mie series solution. (a) E_θ and E_ϕ , (b) H_θ and H_ϕ (normalized to $|\vec{H}_{inc}|$).

4.3 Validation of FDTD results by comparison with method of moments (MoM) results

Although an exact analytical solution for the scattering from finite-length cylinders does not exist, numerical methods can indeed provide accurate results. The study of the scattering behavior of a dielectric cylinder is relevant in this study because several vegetation components can be represented by them. In microwave remote sensing, a vegetation canopy can be considered as a multilayered medium above a half space representing the ground. Each layer can be modeled as an ensemble of individual dielectric objects of different type, size, and

orientation [3]. Among the most common components in a vegetated medium are cylindrical structures, such as stems, branches, trunks, needles and stalks [44, 45]. The cylinders are generally circular, homogeneous, and lossy.

While the numerical treatment of the problem of scattering from a finite cylinder has generally been limited to the method of moments [46], the FDTD method is suitable for problems involving inhomogeneous cylinders.

In this section it is carried out a comparison of the normalized bistatic coefficient of finite-size cylinder using two numerical methods: the FDTD approach and the method of moments (MoM). For this purpose, the results published in [47] are used.

For the comparison, consider a finitely-long circular dielectric cylinder of radius a and length L , with permittivity $\epsilon = \epsilon_c \epsilon_0$ and permeability $\mu = \mu_0$, located in free space. Here, ϵ_0 and μ_0 are the free space permittivity and permeability, respectively, and $\epsilon_c = \epsilon' - j\epsilon''$ is the (complex) relative permittivity of the cylinder. A rectangular coordinate system (x, y, z) is defined with its origin in the center of the cylinder, and the z -axis coincident with the cylinder axis, as illustrated in Figure 4.4.

Assuming an angular frequency $\omega = 2\pi f$ (f being the frequency), and time dependence of the form $e^{j\omega t}$ for all electromagnetic quantities, the cylinder is considered to be illuminated by a uniform plane wave given by

$$\vec{E}^{(i)}(r) = \hat{q}_i e^{-jk_0 \hat{k}_i \cdot \vec{r}}, \quad q = h, v. \quad (4.2)$$

where $k_0 = \omega \sqrt{\epsilon_0 \mu_0}$ is the free space wavenumber, and

$$\hat{k}_i = -\hat{x} \sin \theta_i \cos \phi_i - \hat{y} \sin \theta_i \sin \phi_i - \hat{z} \cos \theta_i \quad (4.3)$$

is the propagation vector of the incident wave from the direction (θ_i, ϕ_i) . Unit vectors, such as \hat{x} or \hat{k}_i , are denoted by symbols with hats on them.

A scattered wave is considered in the direction (θ_s, ϕ_s) with propagation vector

$$\hat{k}_s = \sin \theta_s \cos \phi_s \hat{x} + \sin \theta_s \sin \phi_s \hat{y} + \cos \theta_s \hat{z} \quad (4.4)$$

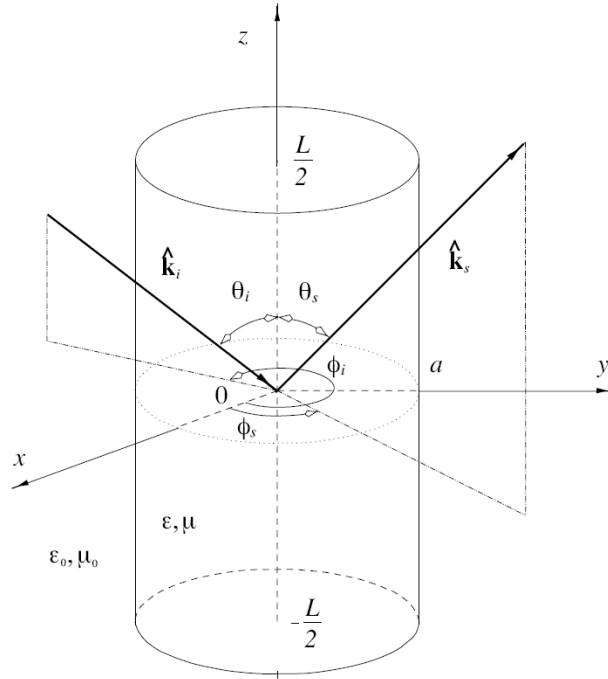


Figure 4.4. Geometry used to compute scattering from a cylinder. Figure reproduced from [47].

The relative dielectric constant ϵ_c of vegetation structures greatly depends on their water content. Tree trunk and branches are usually drier and therefore have a lower ϵ_c than corn stalks. For comparison purposes only one value for the dielectric constant ϵ_c is used. The value chosen in [47] is $\epsilon_c = 18 - j6$, and is consistent with ground data measurements and Ulaby's empirical model [48].

In radar remote sensing, particularly when considering scattering from a layer of dielectric objects, the interest lies in the main scattering lobes. This is a consequence of the large number of scatterers in such vegetation media. Since the contributions from the single scatterers are added all together, the relative weight of the scattering from the side lobes becomes negligible. Therefore, when comparing scattering coefficient using different numerical methods it is considered acceptable if the two methods agree inside the main scattering lobe and does not produce high scattering elsewhere.

In the following section, the values of the scattering coefficient (scattering cross section per unit area) computed by both numerical methods are compared. In particular, for two incident angles (θ_i, ϕ_i) , the bistatic scattering coefficient over a range of scattering angles (θ_s, ϕ_s) using both methods is determined. In agreement with the results of [47] the illustration of results is limited to the case of scattering in the same plane $\phi = \phi_i$ of the incident wave.

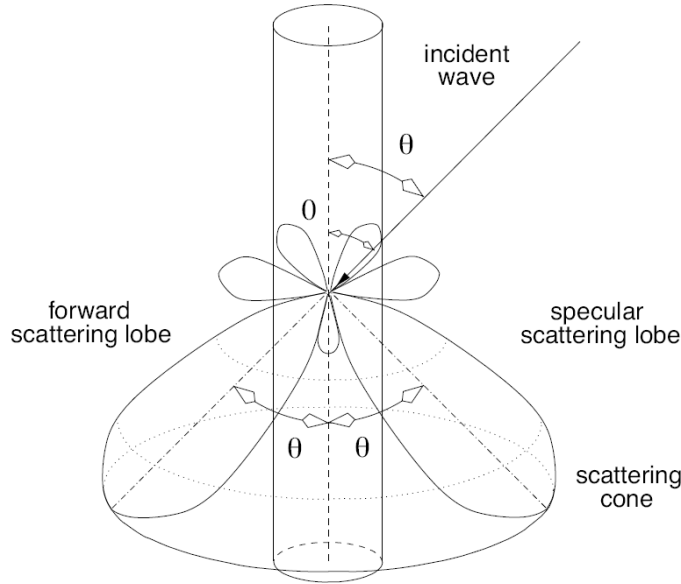


Figure 4.5 General scattering pattern of a cylinder. Figure reproduced from [47].

A cylinder with dimensions chosen consistently with the ground data in [49] and [50] is considered. The general shape of the scattering pattern of a dielectric cylinder is illustrated in Figure 4.5. The amplitude of the scattering has its maximum in a conical region also referred to as the scattering cone. In a section $\phi = \phi_i$ of the scattering pattern there will be two relative maxima corresponding to the main scattering cone, one in the forward direction, the other one in the specular direction with respect to the cylinder side.

In the following, the normalized bistatic scattering coefficient $\sigma/(\pi a^2)$ are plotted as a function of the scattering angle for a fixed incident angle, in both hh - and vv -polarization. The scattering angle θ_s in the plots ranges between 0 and 2π , therefore only the specular lobe at $\theta_s = \pi - \theta_i$ will be observable.

The case examined is a cylinder of length $L = 10.0\lambda_0$ and radius $a = 0.4\lambda_0$ with $\epsilon_c = 18 - j6$. For a wavelength $\lambda_0 = 60\text{ cm}$ (or $f = 500\text{ MHz}$, in P -band), this corresponds to a tree trunk 6 m long with a diameter of 4.8 cm . The normalized bistatic scattering coefficient $\sigma/(\pi a^2)$ is plotted in Figure 4.6 as a function of the scattering angle θ_s for an incident angle $\theta_i = 20^\circ$, in both hh - and vv -polarization. The solid curve represents the FDTD solution, while the dashed curve is obtained using the method of moments. A very good agreement can be observed between the two solutions except for vv -polarization at angles θ_s far from the specular scattering lobe located at approximately $\theta_s = 160^\circ$, and for h - h polarization at $\theta_s = 100^\circ$, respectively. When treating remote sensing problems, only the scattering within 10 dB of the peak value is relevant, therefore we are concerned with achieving a good approximation only in the region surrounding the maxima.

For some of the difference in the plots, a possible cause would be the fact that in our approach 160 evaluation points for θ_s were used, while in [47] 120 points were used. An improvement in the FDTD results is expected by reducing the size of the Yee cell; hence, the discretized model of the cylinder would approach more the curvature of the cylinder. With the previous results, it was shown that the FDTD approach used in this study provides accurate values for scattered fields in the far-zone for cylinder sizes and dielectric constant similar to those used to represent vegetation elements.

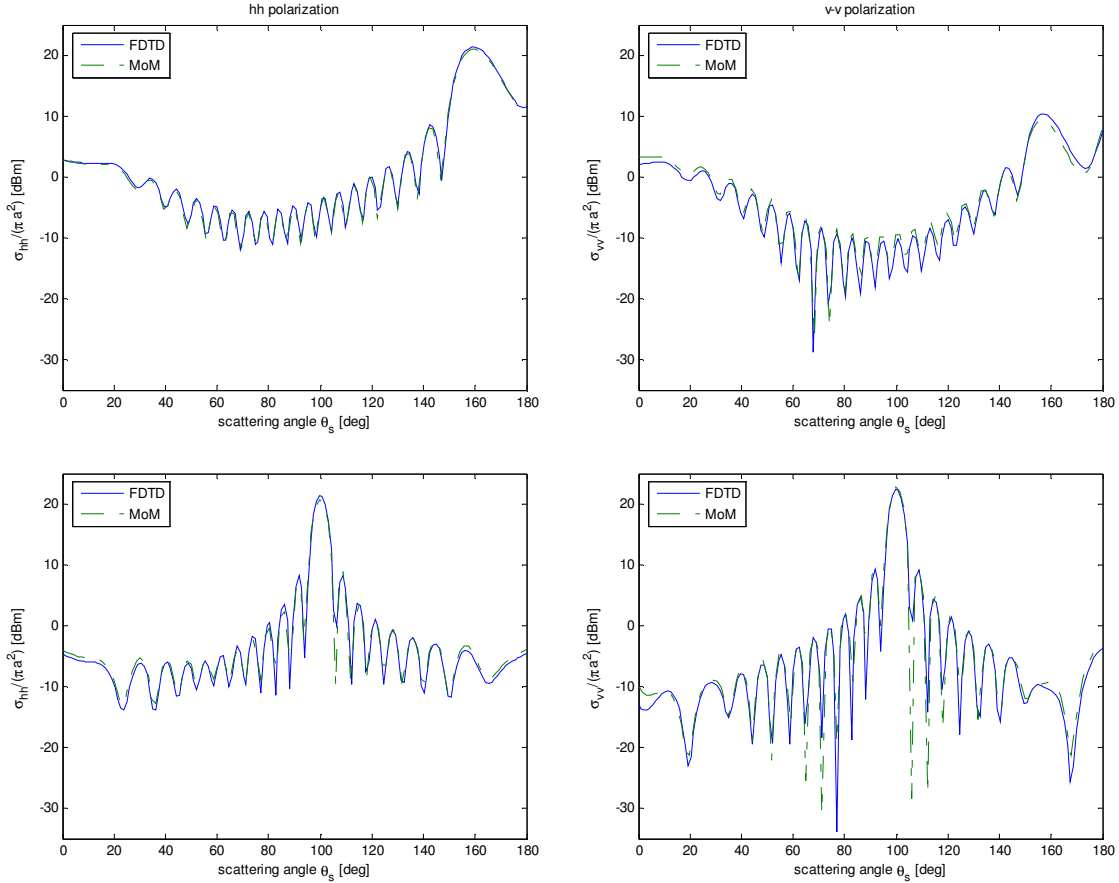


Figure 4.6 Normalized bistatic scattering coefficient vs. scattering angle for finite dielectric cylinder computed with FDTD and MoM. The parameters of the cylinder are $L = 10.0\lambda_0$, $a = 0.4\lambda_0$, $\epsilon_c = 18 - j6$, and incident angle $\theta_i = 20^\circ$ (top) and $\theta_i = 80^\circ$ (bottom).

4.4 Cross sections computation using FDTD and Mie series solutions

For the analysis conducted in this study, two parameters of interest are the absorption and scattering cross sections. Hence, a final test to be conducted to assess the accuracy of the FDTD approach is the comparison of absorption cross section computed using FDTD method and Mie series solutions.

The object under study was also a sphere. The frequency of analysis was in the range 5.0 - 7.0 GHz (C-band). The sphere had a physical diameter of 4 cm (0.6667 - 0.9333 λ_0). The relative permittivity values are 4.0 and 10.0. The conductivity values are 0.1 and 0.5 S/m. The Yee cell size was chosen to be $\Delta x = \Delta y = \Delta z = 0.001m$ (0.0167 - 0.0233 λ_0), 0.00075m (0.0125 - 0.0175 λ_0), and 0.0005m (0.0083 - 0.0117 λ_0) for $\epsilon_r = 4.0$, while for $\epsilon_r = 10.0$ the cell size was 0.00063m (0.0083 - 0.0117 λ_0) and 0.000315m (0.00525 - 0.00735 λ_0). Table 4.3 shows the parameters used in absorption cross section results comparison.

Table 4.3 Parameters used for comparison de computation of absorption cross section of a 4-cm-diameter sphere using analytical solution and FDTD simulations.

Relative permittivity	Conductivity	Yee cell size
$\epsilon_r = 4.0$	$\sigma = 0.1 S / m$	$\Delta x = 0.0010 m$
$\epsilon_r = 4.0$	$\sigma = 0.1 S / m$	$\Delta x = 0.0005 m$
$\epsilon_r = 10.0$	$\sigma = 0.5 S / m$	$\Delta x = 0.000315 m$
$\epsilon_r = 4.0$	$\sigma = 0.5 S / m$	$\Delta x = 0.0010 m$
$\epsilon_r = 10.0$	$\sigma = 0.1 S / m$	$\Delta x = 0.00063 m$
$\epsilon_r = 10.0$	$\sigma = 0.1 S / m$	$\Delta x = 0.000315 m$

Figures 4.7 to 4.12 show the comparison of absorption cross section of a 4-cm - diameter sphere computed using analytical solutions and the FDTD approach.

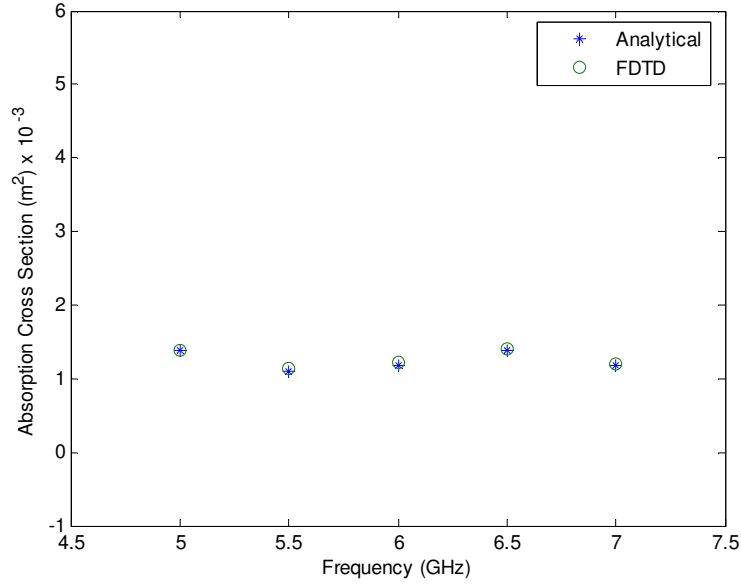


Figure 4.7 Comparison of absorption cross section of a 4-*cm* diameter sphere using analytical solution and FDTD simulations. The properties of the sphere are $\epsilon_r = 4.0$ and $\sigma = 0.1 S/m$. The Yee cell is $\Delta x = 0.001m$ ($0.0167 - 0.0233 \lambda_0$).

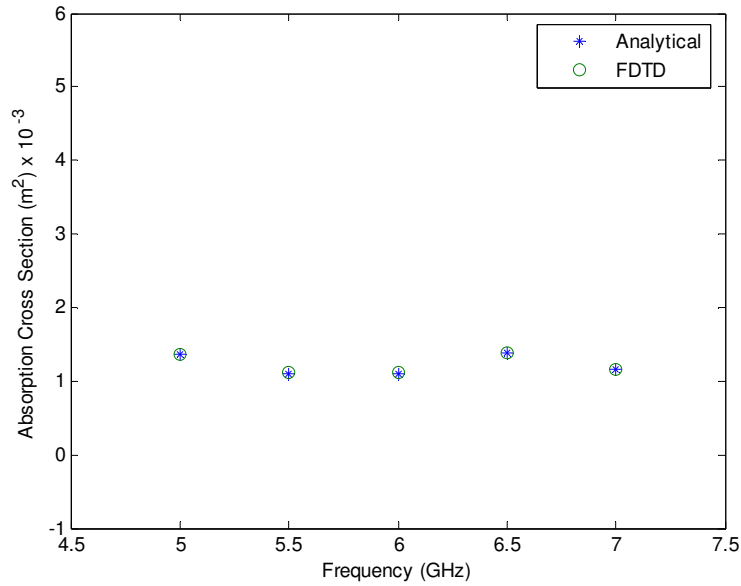


Figure 4.8 Comparison of absorption cross section of a 4-*cm* diameter sphere using analytical solution and FDTD simulations. The properties of the sphere are $\epsilon_r = 4.0$ and $\sigma = 0.1 S/m$. The Yee cell is $\Delta x = 0.00050m$ ($0.0083 - 0.0117 \lambda_0$).

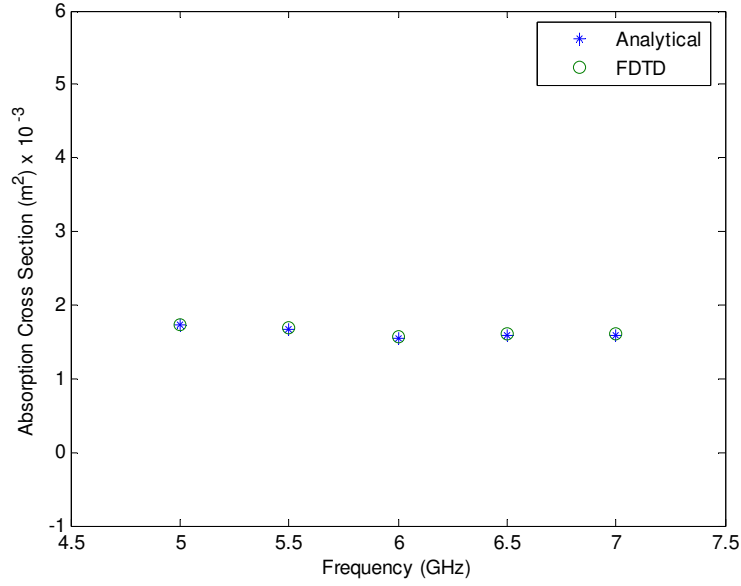


Figure 4.9 Comparison of absorption cross section of a 4 - *cm* diameter sphere using analytical solution and FDTD simulations. The properties of the sphere are $\epsilon_r = 10.0$ and $\sigma = 0.5 S/m$. The Yee cell is $\Delta x = 0.000315 m$ ($0.00525 - 0.00735 \lambda_0$).

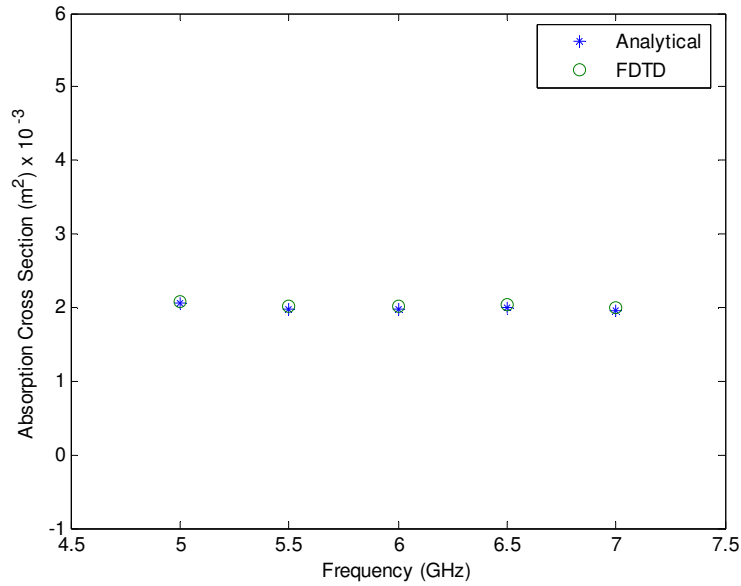


Figure 4.10 Comparison of absorption cross section of a 4 - *cm* diameter sphere using analytical solution and FDTD simulations. The properties of the sphere $\epsilon_r = 4.0$ and $\sigma = 0.5 S/m$. The Yee cell is $\Delta x = 0.001 m$ ($0.0167 - 0.0233 \lambda_0$).

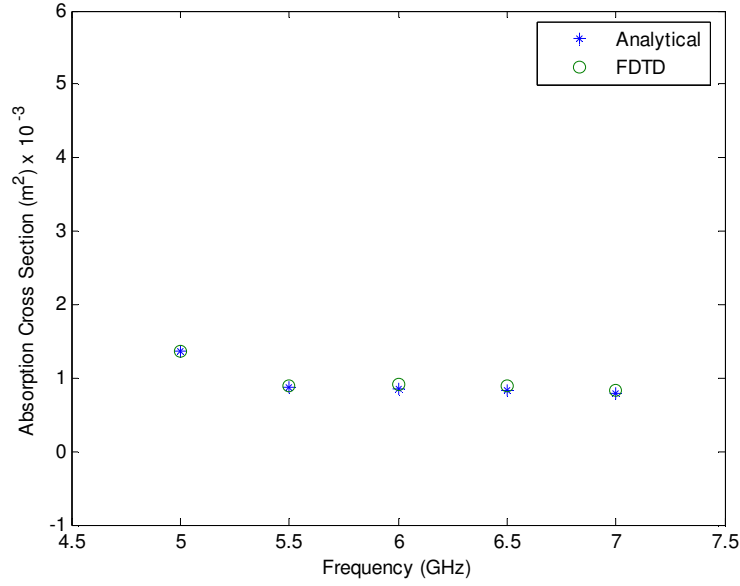


Figure 4.11 Comparison of absorption cross section of a 4-*cm* diameter sphere using analytical solution and FDTD simulations. The properties of the sphere are $\epsilon_r = 10.0$ and $\sigma = 0.1 S/m$. The Yee cell is $\Delta x = 0.00063m$ ($0.0083 - 0.0117 \lambda_0$).

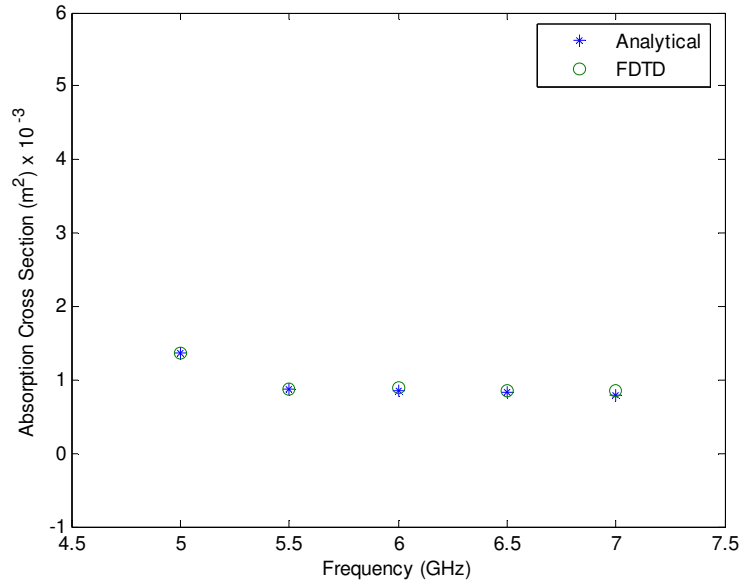


Figure 4.12 Comparison of absorption cross section of a 4-*cm* diameter sphere using analytical solution and FDTD simulations. The properties of the sphere are $\epsilon_r = 10.0$ and $\sigma = 0.1 S/m$. The Yee cell is $\Delta x = 0.000315m$ ($0.00525 - 0.00735 \lambda_0$).

Figures 4.7 to 4.12 show both that a) the FDTD approach can be used to compute the required fields to obtain the absorption cross section, and b) the integration approach used to compute the absorption cross section is satisfactory. In next section more information will be given about the integration approach.

In the range of analysis shown in this section, since the absorption cross section is directly proportional to the conductivity the target, as the conductivity is higher, the relative numerical error in the FDTD results with respect to the Mie series solution decreases. Also, as expected, as the cell size is reduced, the numerical dispersion is reduced accordingly; hence, decreasing the error.

4.5 Computation of emissivity from finite size objects

4.5.1 Introduction

All substances at a finite absolute temperature radiate electromagnetic energy. The emphasis in existing emission modeling for passive remote sensing has been on emission from extensive-area targets. This section presents the computation of the emissivity of a finite-size object. In order to integrate the effects of finite-size objects into an extensive area target model, it is imperative to have a good understanding of the emission properties of finite-size objects. Since the purpose is to use the results of this study in passive remote sensing models, such as those described in [3, 5], it is needed to characterize both the emission behavior of the object and its scattering properties. To date, most of the modeling study on objects is for active sensing. With respect to the emissivity, studies in remote sensing modeling reported in literature are mainly for random surfaces. This section focuses on emission modeling for finite-size object with arbitrary shape. In [33, 51] analytical expressions are reported to find the emission from a body. A general expression is given for an object with arbitrary shape.

However, to obtain practical results, assumptions were made to make the formulation mathematically tractable; approximation using canonical object have been used. In [33, 43, 51] the equations to compute the flux of energy emitted into a particular direction of space and with a particular polarization is proportional to the absorptivity. The complexity of the analytical relation between the object's Stokes parameters and its absorption properties is determined by the geometry and dielectric properties of the object. The significance of those equations to compute the emission from a finite-size anisotropic medium is the fact that it relates the emission from the object to the absorption cross section of the object, therefore relating a passive emission problem to an active scattering problem. Consequently, to model the emission from an object, a numerical method can be used to simulate the interaction of an interrogating wave and the object, namely an active remote sensing modeling, and hence find the cross sections of the object. Additionally, numerical method allows for modeling of emission from an object of arbitrary shape and dielectric value. The FDTD approach has been shown adequate to perform this task [40]. In this study, a 3D-FDTD algorithm was developed and used to simulate a plane wave impinging on an object from several angles and polarizations. Both the absorption and the scattering cross sections of an object are obtained to compute the emissivity of an object.

4.5.2 Emission from finite-size objects

The characteristic as a source of a finite-size object is given by its brightness temperature emitted in a specific direction. When this is emitted by a blackbody, the brightness temperature is equal to the physical temperature T of the body. The ratio between the brightness temperature of the body and that one of a blackbody is the emissivity e . In this section an approach to compute the emissivity from an object is presented. A similar approach is given in [52], however it is valid for an extended surface. Consider that a wave with

polarization state α is incident on the object in the direction \hat{i} . Then the ratio of the total scattered power to the sum of scattered and absorbed power in the object, namely the albedo ω , is computed as

$$\omega = \frac{Q^{sca}}{Q^{abs} + Q^{sca}} \quad (4.5)$$

where Q^{sca} and Q^{abs} are the scattering and absorption cross sections, respectively.

The absorption cross section is defined as the power dissipated in the object under plane wave incidence, divided by the power density of the incident wave [53]. This can be calculated by integrating Poynting vector of the total field over a closed surface containing the object. Similarly, in the scattering cross section formulation the total power scattered by the object is used. According to [52] the following expressions can be used to obtain both the absorption and scattering cross sections:

$$Q^{abs} = \frac{-\int_{S_0} \text{Re}\left(\frac{1}{2} \vec{E} \times \vec{H}^*\right) \cdot d\vec{a}}{|S_i|} \quad (4.6)$$

$$Q^{sca} = \frac{\int_{S_0} \text{Re}\left(\frac{1}{2} \vec{E}_s \times \vec{H}_s^*\right) \cdot d\vec{a}}{|S_i|} \quad (4.7)$$

where \vec{E}, \vec{H} and \vec{E}_s, \vec{H}_s are the total and scattered fields respectively.

The fractional power absorbed by the object is therefore

$$a_\alpha(\hat{i}) = 1 - \omega_\alpha(\hat{i}). \quad (4.8)$$

The quantity $a_{\alpha}(\hat{i})$ is the absorptivity. The brightness temperature T_{α} emitted in the direction $(-\hat{i})$, with polarization state α , from an object kept at the temperature T is given then by

$$T_{\alpha}(-\hat{i}) = e_{\alpha}(-\hat{i})T . \quad (4.9)$$

According to Kirchhoff's law, if the object is in thermal equilibrium, the absorption must be equal to the emission, and therefore the emissivity is equal to the absorptivity:

$$e_{\alpha}(-\hat{i}) = a_{\alpha}(\hat{i}) . \quad (4.10)$$

4.5.3 Numerical modeling approach

According to Eq. (4.5), both the absorption and scattering cross sections of the object under analysis are needed. They will be computed using the FDTD approach. A plane wave incident at various angles is simulated and both the total and scattered electromagnetic fields tangential to a virtual surface enclosing the object (Figs. 4.13 and 4.14) are sampled at several points to compute the Poynting Vector at those points. The resulting Poynting vector values are then integrated over the enclosing surface to compute the power either leaving or entering the surface.

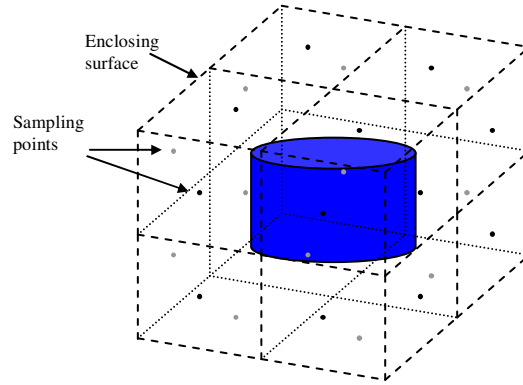


Figure 4.13 Virtual enclosing surface used for computation of cross sections. For absorption cross section the enclosing surface is generated in the FDTD total field region, while for the scattering cross section the enclosing surface is generated in the scattered field region.

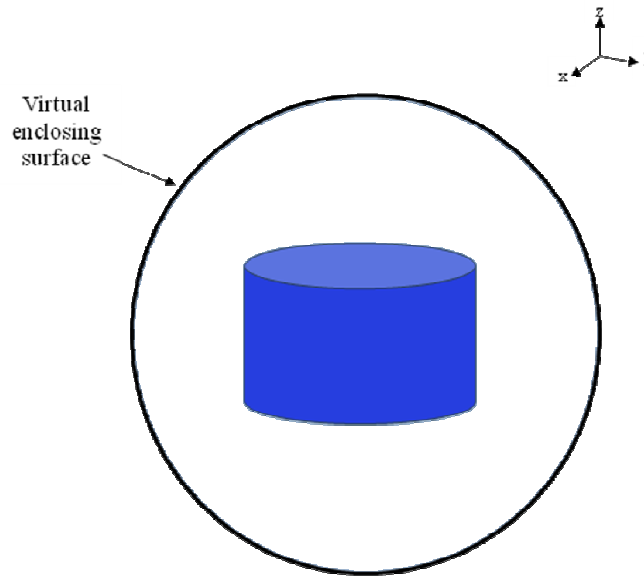


Figure 4.14 Virtual enclosing surface used for computation of cross sections using the Gaussian quadrature technique. For absorption cross section the enclosing surface uses the FDTD total field values, while for the scattering cross section the enclosing surface uses the scattered fields by subtracting the incident field from the total field.

The sampling of the required electromagnetic fields was performed in two ways: (a) using a virtual enclosing cube (Fig. 4.13), and (b) using sampling points according to the Gaussian quadrature technique (Fig. 4.14). The former approach simplifies the sampling since

only the tangential components at each of the faces are recorded. Since the surface was a cube, the required computational space could be reduced. The later approach requires both all rectangular components to be recorded and more computational memory; however it provides a more precise integration.

In the first approach, the enclosing area is formed by differential patches. The values of the \vec{E} and \vec{H} fields at the center of the patches are required. However, due to the nature of the FDTD algorithm, the fields are computed at shifted positions with respect to each other in the grid. To circumvent this problem, once the patches forming the enclosing surface were defined, the values of the \vec{E} and \vec{H} fields at the center of them were obtained by performing a tri-linear interpolation and then sampled. The interpolated values for \vec{E} and \vec{H} were assumed to be constant in the complete patch area.

To compute the absorption cross section the equation

$$Q^{abs} = \frac{-\int_{S_0} \text{Re}\left(\frac{1}{2} \vec{E} \times \vec{H}^*\right) \cdot d\vec{a}}{|S_i|},$$

was used. Due to the FDTD discretization, the numerator was replaced by the following approximation:

$$P = -\sum_{n=1}^N \frac{1}{2} \text{Re}\{\vec{E}_n \times \vec{H}_n^*\} \Delta a. \quad (4.11)$$

where N is the total number of patches and $\Delta a = \Delta s \times \Delta s$, being Δs the length of each patch side, equal to the length of the FDTD cell. The incident power density was computed analytically as:

$$S_i = \frac{|\vec{E}_{inc}|^2}{2\eta}. \quad (4.12)$$

where \vec{E}_{inc} and η are the incident field and the intrinsic impedance of free space, respectively.

4.5.4 Numerical computation of emissivity of lossless objects

Before computing and analyzing the emissivity from several targets, the emissivity from lossless targets is computed. The purpose is to assess the method to compute the emissivity with an a priori known result. Since the loss is zero, then the absorptivity and hence the emissivity must be zero too.

The first analysis was conducted on a cylinder with diameter and height equal to λ_0 . Although the emissivity was reduced by reducing the cell size, hence by increasing the number of points per wavelength for the simulation, the emissivity with respect to incident angle showed inconsistency due to resonance. Therefore, it was concluded that cylinder with dimensions the same as the wavelength should be avoided due to resonance problems.

For a $5GHz$ incident wave, the relative dimension of the cylinder ($d = \frac{5}{6}\lambda_0$ and $h = \frac{5}{6}\lambda_0$) with respect to λ_0 was smaller, therefore the resonance was avoided. Figure 4.15 shows that the emissivity with respect to incident angle approaches to a zero value as the number of points per wavelength is increased. Likewise, the trend of the curve representing the emissivity value tends to be flat. The peak at 45° is due to numerical dispersion.

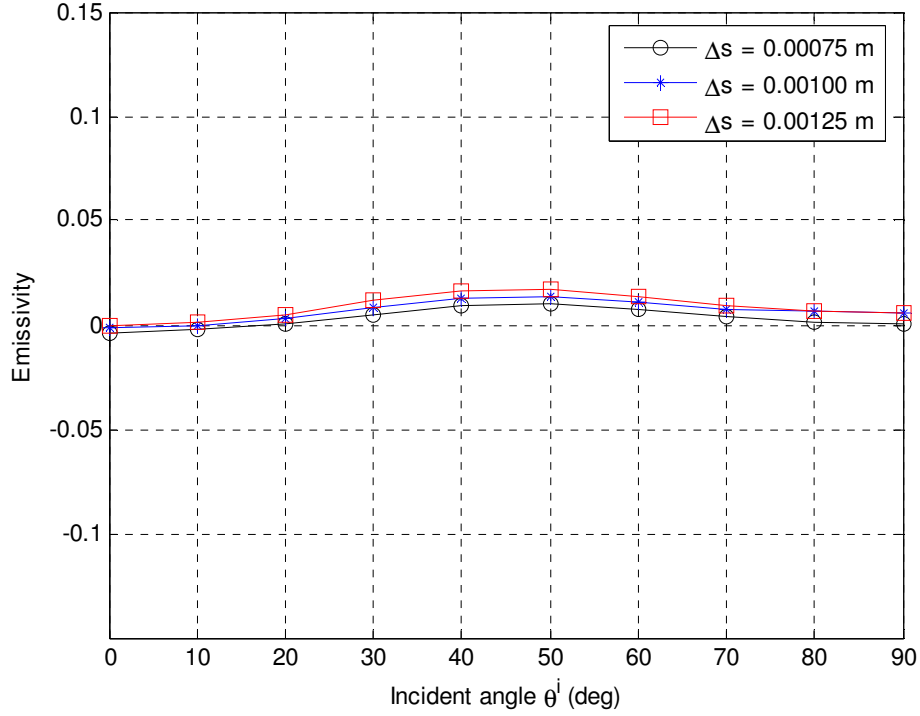


Figure 4.15 Emissivity of lossless cylinder with respect to incident angle, when varying the cell size Δs from $0.00075m$ to $0.00125m$. The dimensions of the cylinder are: diameter = $0.05m$ and height = $0.05m$. The dielectric properties are $\epsilon_r = 4.0$ and $\sigma = 0S/m$. The frequency of analysis is $5GHz$. The polarization is vertical.

Figures 4.16 and 4.17 shows the emissivity of a cylinder with dimensions $d = 0.8\lambda_0$ and $h = 0.8\lambda_0$ for $6GHz$ and $5GHz$ incident waves, respectively. As in previous case, the emissivity shows both a tendency to approach the correct value as the number of points per wavelength is increased; and a peak at 45° due to numerical dispersion.

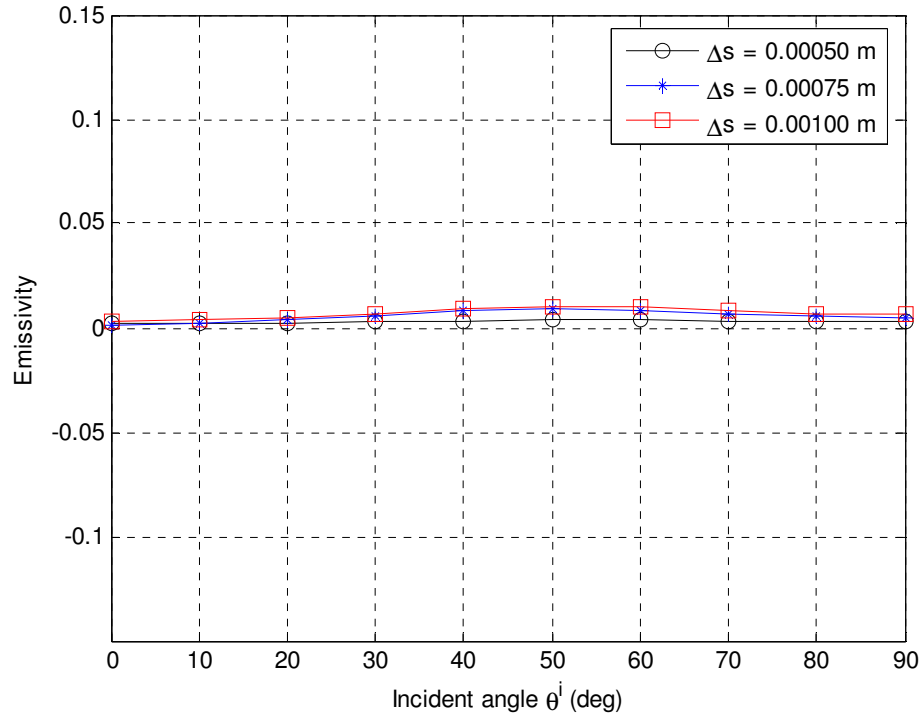


Figure 4.16 Emissivity of lossless cylinder with respect to incident angle, when varying the cell size from Δs from $0.0005m$ to $0.0010m$. The dimensions of the cylinder are: diameter = $0.04m$ and height = $0.04m$. The dielectric properties are $\epsilon_r = 4.0$ and $\sigma = 0S/m$. The frequency of analysis is $6GHz$. The polarization is vertical.

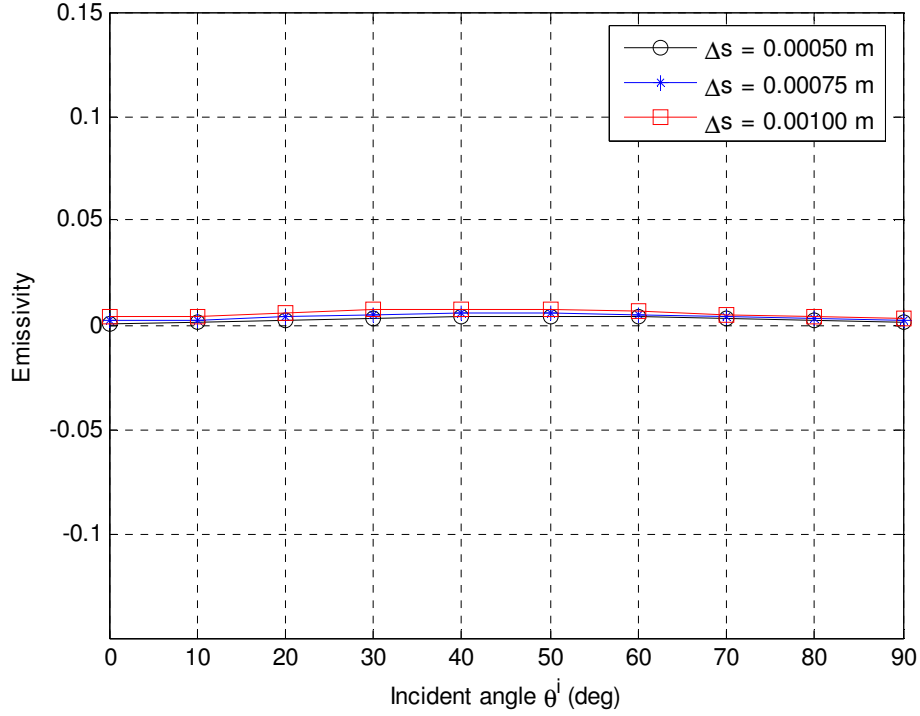


Figure 4.17 Emissivity of lossless cylinder with respect to incident angle, when varying the cell size from Δs from $0.0005m$ to $0.0010m$. The dimensions of the cylinder are: diameter = $0.04m$ and height = $0.04m$. The dielectric properties are $\epsilon_r = 4.0$ and $\sigma = 0S/m$. The frequency of analysis is $5GHz$. The polarization is vertical.

Additionally, the performance of the FDTD integration approach was assessed by computing the emissivity of a perfect-electric-conductor (PEC) object. In case of a PEC object all energy is scattered. Therefore, the absorptivity, and hence emissivity is zero.

For simplicity to represent the conducting object in the computational space, a perfect electric conductor (PEC) cube was used. This way, the PEC model was applied by setting the electric field tangent to the object surfaces to be zero.

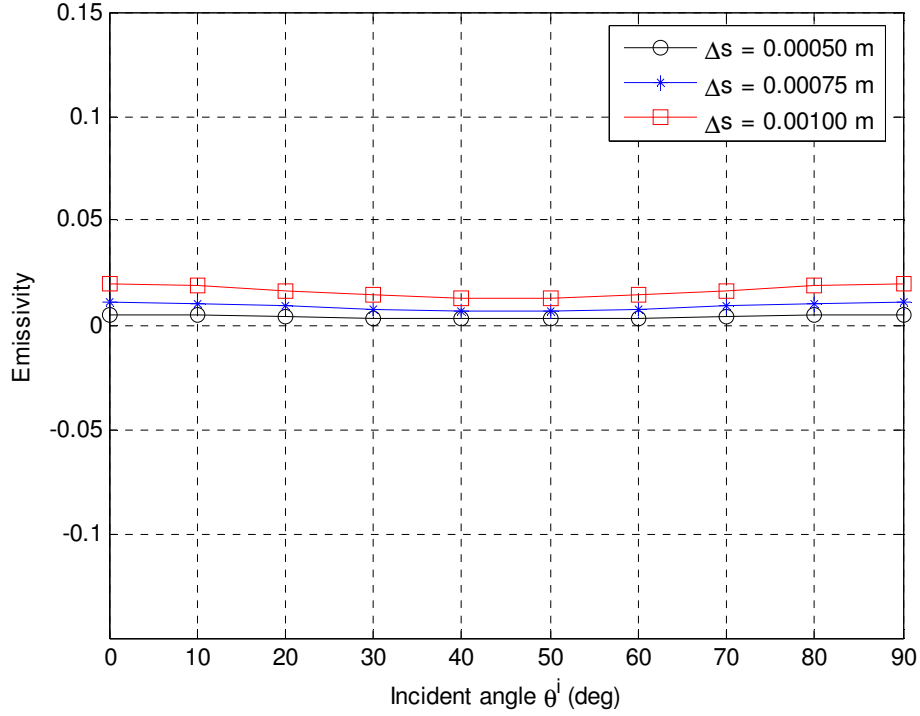


Figure 4.18 Emissivity of PEC cube with respect to incident angle, when varying the cell size from Δs from $0.0005m$ to $0.0010m$. The dimensions of the cube are: side = $0.04m$. The frequency of analysis is $6GHz$. The polarization is vertical.

Figures 4.18 and 4.19 show that for incident frequencies of $6GHz$ and $5GHz$, as expected, the emissivity tends to approach zero as the number of points per wavelength is increased. The effect of the numerical dispersion is also visible. However, contrary to previous cases, the incident wave does not travel through the PEC object, therefore the effect is less at 45° when compared with 0° and 90° incidence.

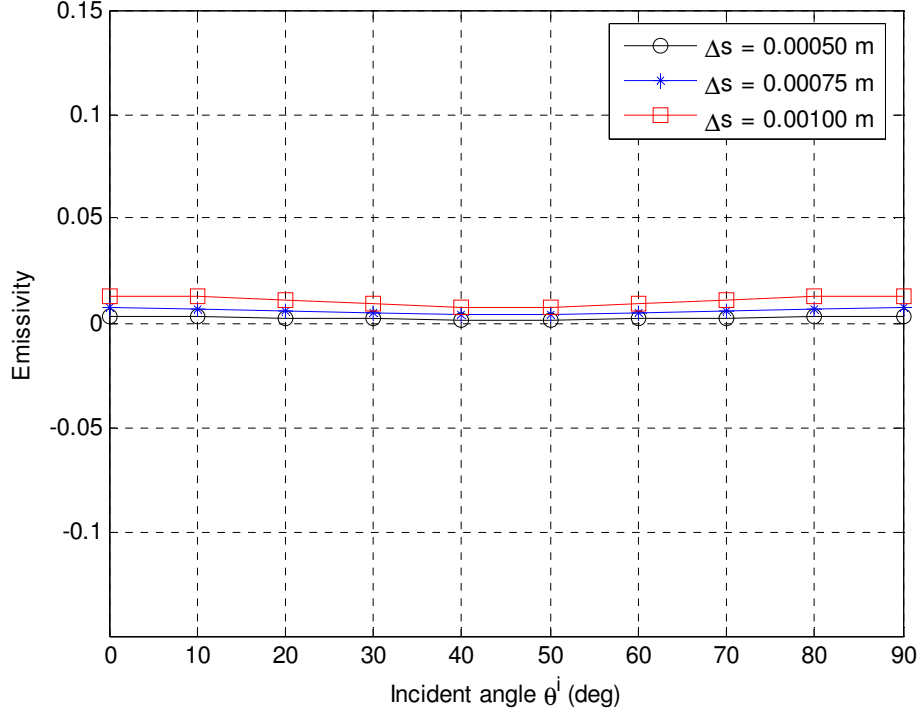


Figure 4.19 Emissivity of PEC cube with respect to incident angle, when varying the cell size from Δs from $0.0005m$ to $0.0010m$. The dimensions of the cube are: side = $0.04m$. The frequency of analysis is $5GHz$. The polarization is vertical.

4.5.5 Numerical computation of emissivity of lossy dielectric objects

The FDTD approach presented can be used to obtain the emissivity of objects with arbitrary shape. In this section, the emissivity calculations are presented for several finite-size objects. A relative permittivity $\epsilon_r = 4.0$, and values for conductivity σ ranging from 0.1 to $0.5S/m$ were used. The frequency of analysis was in the mid-range of C band ($6GHz$).

The emissivity is generally a function of both θ and φ , angles defined as shown in Figure 4.21. However, since the objects presented in this section have symmetry around the axis of rotation, in this case z-axis, the emissivity values are independent of φ , hence all results are shown only as a function of θ . Both the vertical and horizontal polarizations are considered in the FDTD simulations. The incident plane wave was a modulated Gaussian pulse with

central frequency at $6GHz$. To represent the FDTD space a regular grid with a cell size of $1mm$ was used.

4.5.6 Results and analysis

Figure 4.20 shows that the emissivity from a spherical object, due to its symmetry, is only a function of dielectric properties. For the permittivity values under analysis, the emissivity is higher for high conductivity (loss), hence, a higher contrast. The results obtained from the sphere are a good reference to analyze and understand the results from other geometrical shapes. Although small, the FDTD-computed emissivity showed some variation with respect to angle of observation. This was a consequence of the numerical dispersion due to the discretization of the computational space. This variation reduces as the size of the grid cell is reduced.

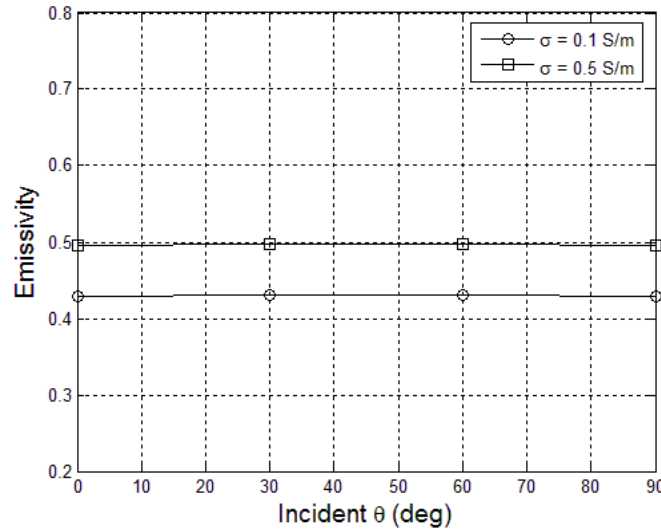


Figure 4.20 Emissivity at $6GHz$ for a sphere ($r = \lambda_0$) with $\epsilon_r = 4.0$ and $\sigma = 0.1, 0.5 S/m$.

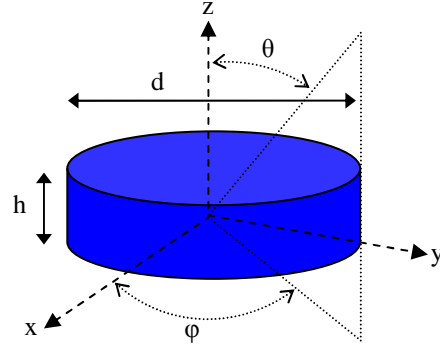


Figure 4.21 Geometry used for FDTD simulation of plane wave impinging on landmine-like object ($d = 2.4\lambda_0$ and $h = 0.8\lambda_0$).

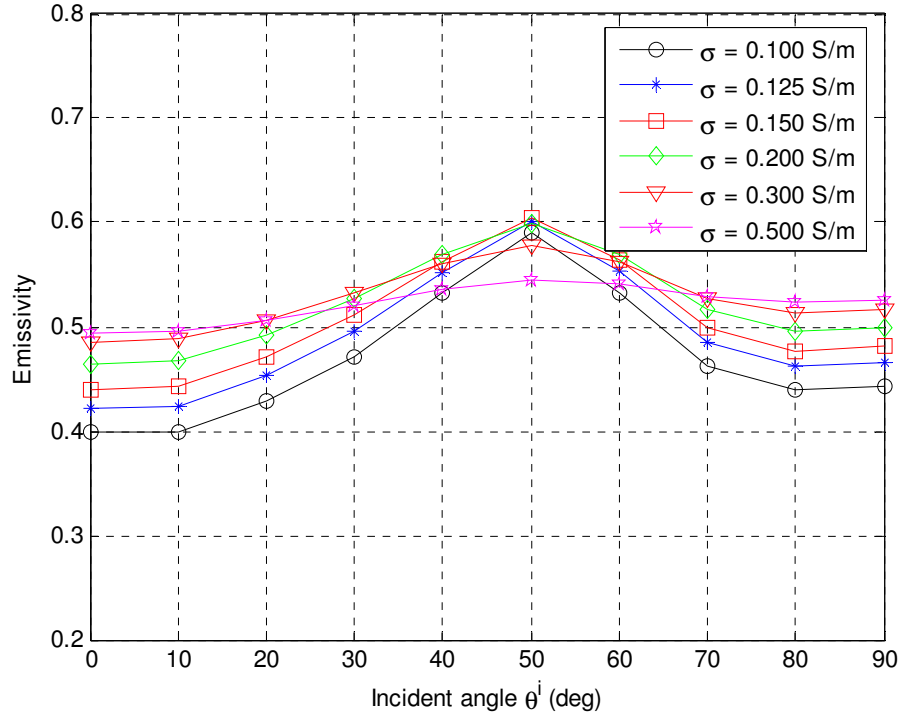


Figure 4.22 Emissivity at 6GHz for a circular cylinder with $\epsilon_r = 4.0$ and $\sigma = 0.1, 0.125, 0.15, 0.2, 0.3, 0.5 \text{ S/m}$, for vertical polarization. Dimensions of the cylinder are $d = 2.4\lambda_0 (12\text{cm})$ and $h = 0.8\lambda_0 (4\text{cm})$.

Figure 4.22 shows the emissivity from the landmine-like object for vertical polarization. For the permittivity analyzed, it can be observed that for low conductivity the

emissivity shows more variation with respect to the observation angle, having a peak value at about 50° . As the conductivity is increased, the emissivity tends to be more uniform with respect to the observation angle. Figure 4.23 shows the emissivity from the landmine-like object for horizontal polarization. Similarly to previous case, it can be observed that for low conductivity the emissivity shows more variation with respect to the observation angle, having also a peak value at about 50° . As the conductivity is increased, the emissivity tends to be more uniform with respect to the observation angle.

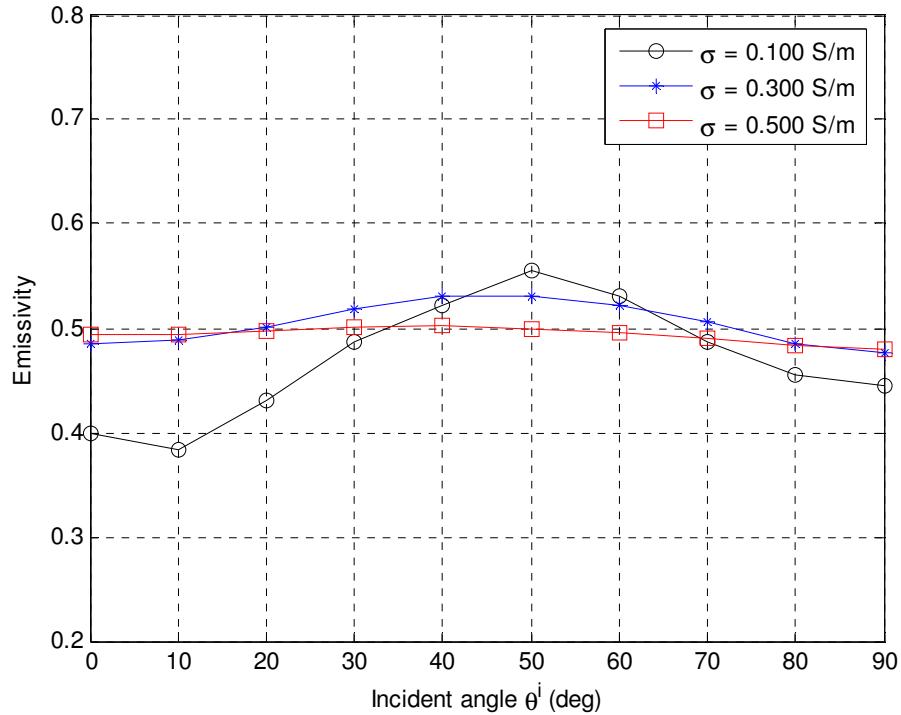


Figure 4.23 Emissivity at $6GHz$ for a circular cylinder with $\epsilon_r = 4.0$ and $\sigma = 0.1, 0.3, 0.5 S/m$, for horizontal polarization. Dimensions of the cylinder are $d = 2.4\lambda_0 (12cm)$ and $h = 0.8\lambda_0 (4cm)$.

Regarding the emissivity of the cylinder represented in Fig. 4.24, it can be observed that it has also more variation with respect to the observation angle for low conductivity, having a minimum at about 30° for both vertical and horizontal polarization (Fig. 4.25 and 4.26).

However, it shows a higher emissivity for horizontal polarization. Similarly as in the landmine-like object, the emissivity tends to be more uniform independently of the observation angle when the conductivity takes a higher value.

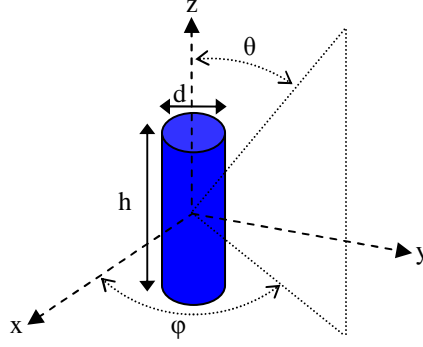


Figure 4.24 Geometry used for FDTD simulation of plane wave impinging on cylinder ($d = 1.2\lambda_0(6cm)$ and $h = 3.6\lambda_0(18cm)$).

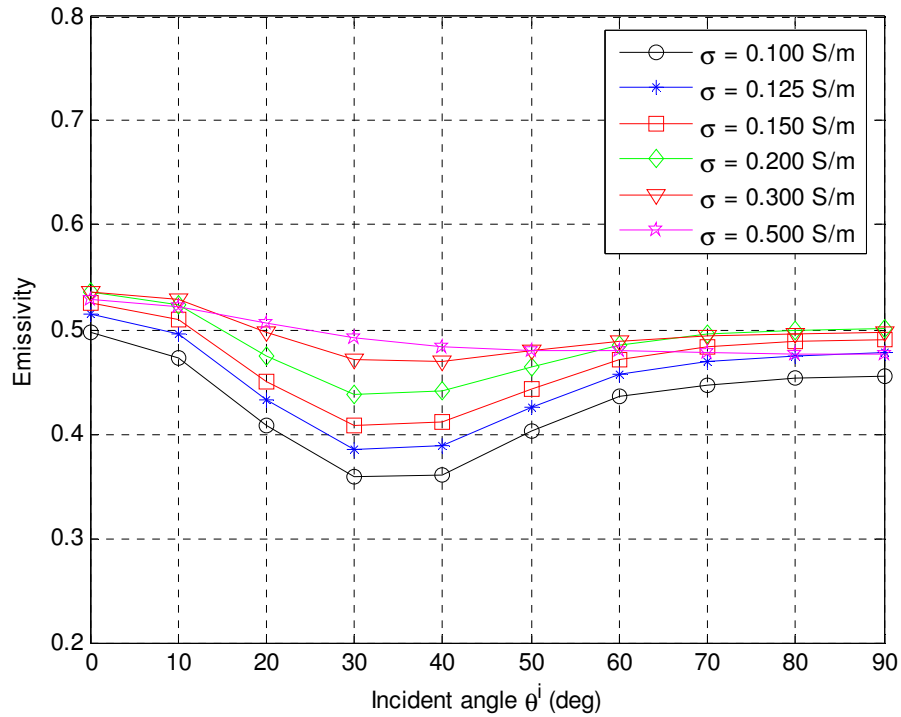


Figure 4.25 Emissivity at $6GHz$ for a circular cylinder with $\epsilon_r = 4.0$ and $\sigma = 0.1, 0.125, 0.15, 0.2, 0.3, 0.5 S/m$, for vertical polarization. Dimensions of the cylinder are $d = 1.2\lambda_0(6cm)$ and $h = 3.6\lambda_0(18cm)$.

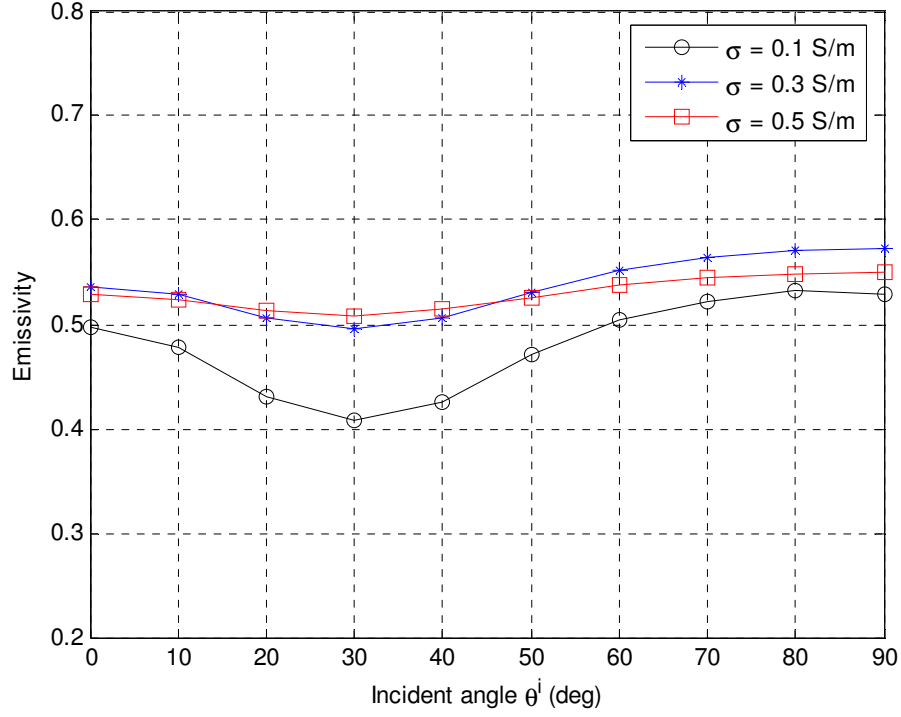


Figure 4.26 Emissivity at $6GHz$ for a circular cylinder with $\epsilon_r = 4.0$ and $\sigma = 0.1, 0.3, 0.5 S/m$, for horizontal polarization. Dimensions of the cylinder are $d = 1.2\lambda_0 (6cm)$ and $h = 3.6\lambda_0 (18cm)$.

In order to gain more insight in the behavior of emissivity of finite size objects with respect to dimensions and dielectric properties, more objects are tested. In following lines the objects as well as the emissivity plots are shown.

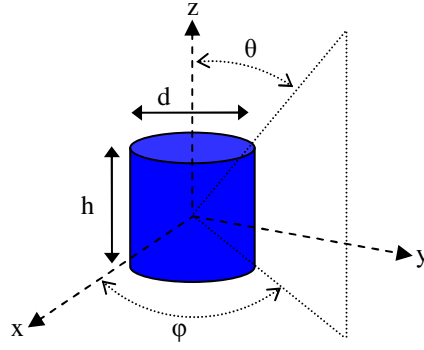


Figure 4.27 Geometry used for FDTD simulation of plane wave impinging on cylinder ($d = 1.6\lambda_0(8cm)$ and $h = 1.6\lambda_0(8cm)$).

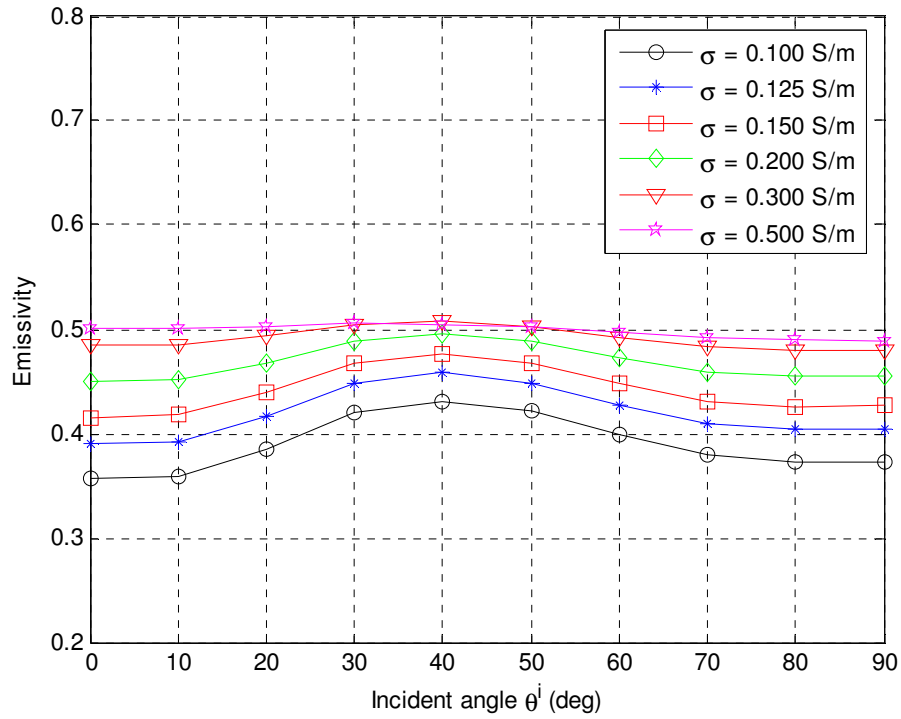


Figure 4.28 Emissivity at $6GHz$ for a circular cylinder with $\epsilon_r = 4.0$ and $\sigma = 0.1, 0.125, 0.15, 0.2, 0.3, 0.5 S/m$, for vertical polarization. Dimensions of the cylinder are $d = 1.6\lambda_0(8cm)$ and $h = 1.6\lambda_0(8cm)$.

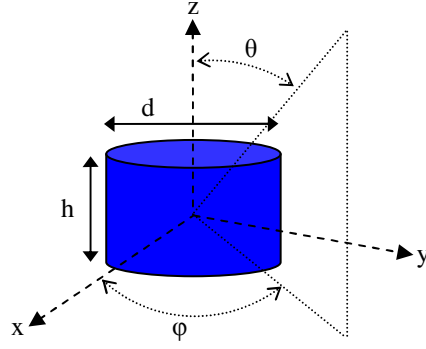


Figure 4.29 Geometry used for FDTD simulation of plane wave impinging on cylinder ($d = 2.0\lambda_0(10\text{ cm})$ and $h = 1.2\lambda_0(6\text{ cm})$).

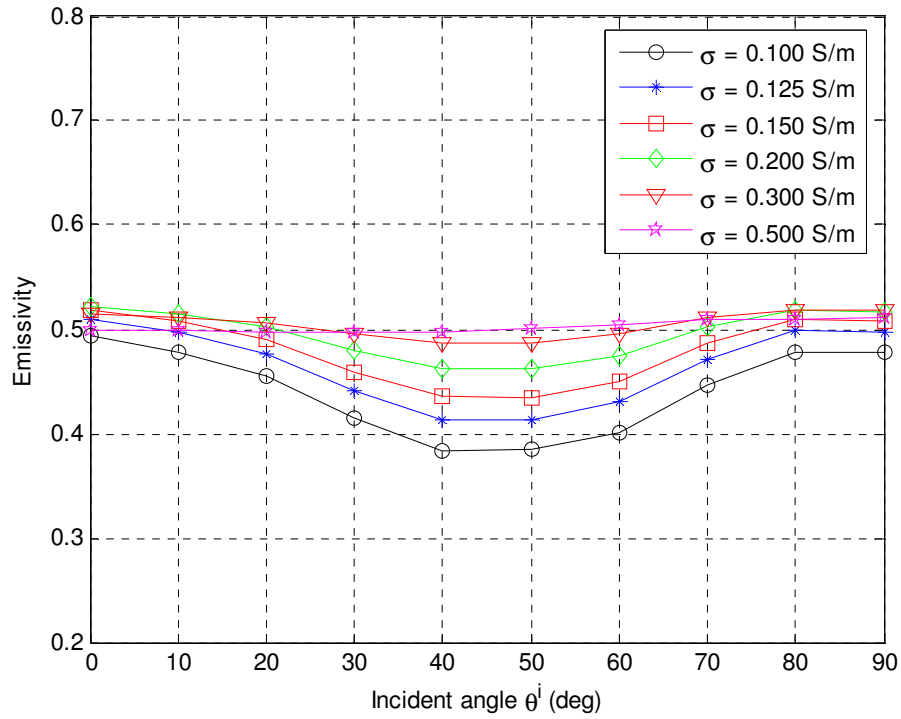


Figure 4.30 Emissivity at 6 GHz for a circular cylinder with $\epsilon_r = 4.0$ and $\sigma = 0.1, 0.125, 0.15, 0.2, 0.3, 0.5\text{ S/m}$, for vertical polarization. Dimensions of the cylinder are $d = 2.0\lambda_0(10\text{ cm})$ and $h = 1.2\lambda_0(6\text{ cm})$.

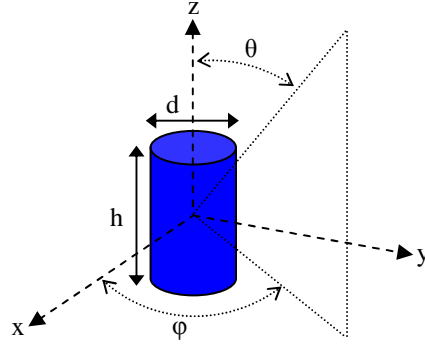


Figure 4.31 Geometry used for FDTD simulation of plane wave impinging on cylinder ($d = 1.2\lambda_0 (6\text{ cm})$ and $h = 1.8\lambda_0 (9\text{ cm})$).

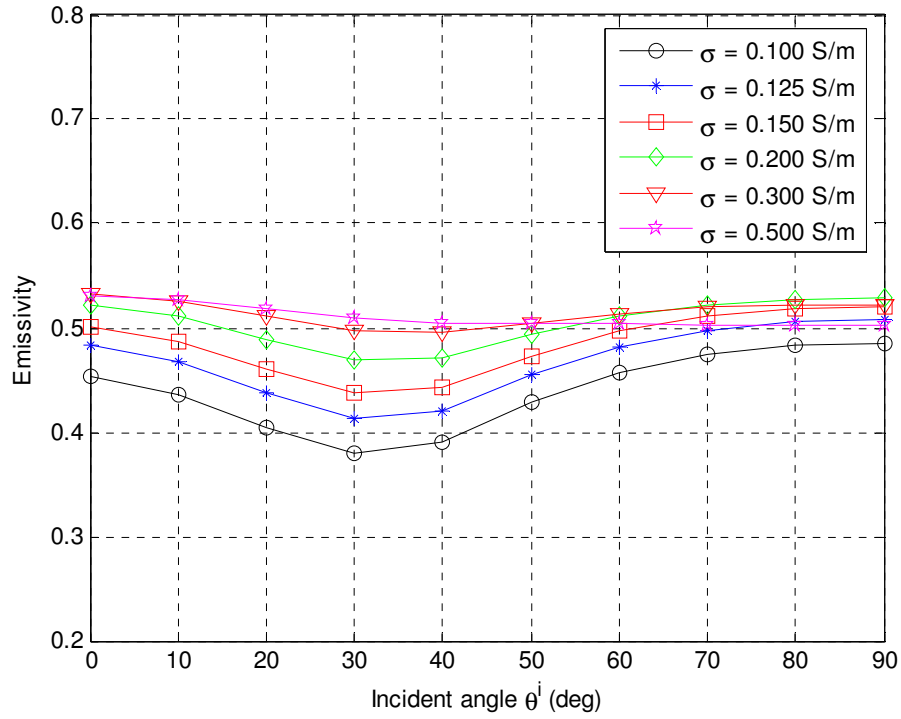


Figure 4.32 Emissivity at 6 GHz for a circular cylinder with $\epsilon_r = 4.0$ and $\sigma = 0.1, 0.125, 0.15, 0.2, 0.3, 0.5\text{ S/m}$, for vertical polarization. Dimensions of the cylinder are $d = 1.2\lambda_0 (6\text{ cm})$ and $h = 1.8\lambda_0 (9\text{ cm})$.

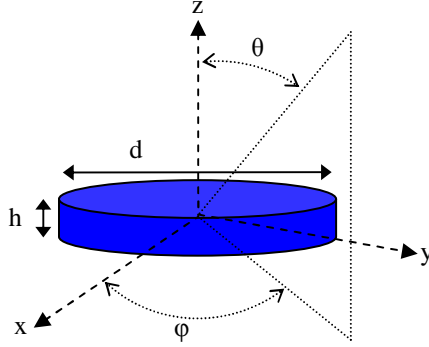


Figure 4.33 Geometry used for FDTD simulation of plane wave impinging on cylinder ($d = 2.8\lambda_0(14\text{ cm})$ and $h = 0.4\lambda_0(2\text{ cm})$).

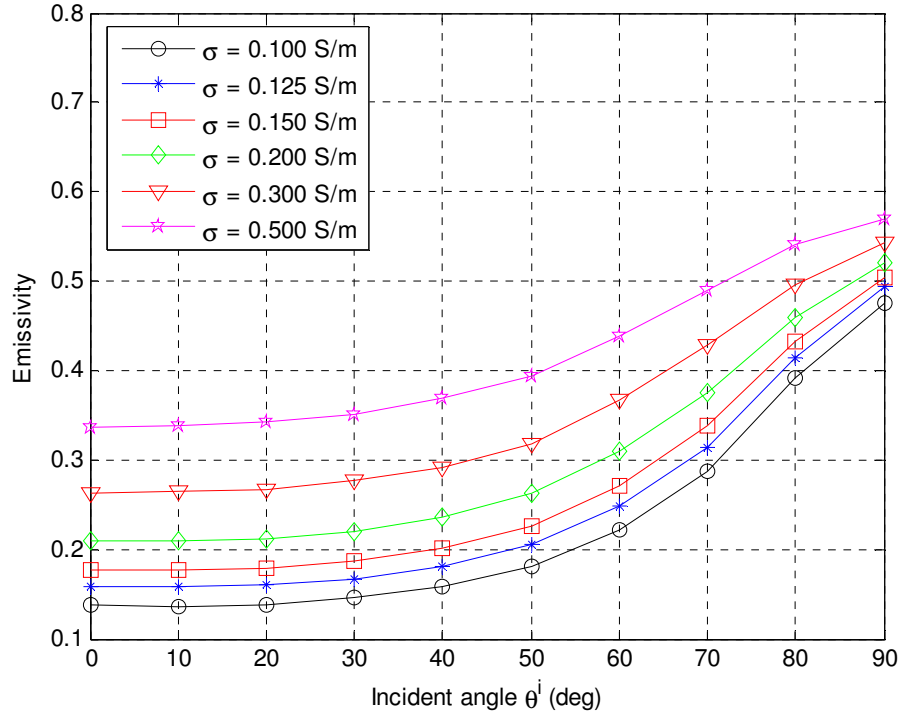


Figure 4.34 Emissivity at 6 GHz for a circular cylinder with $\epsilon_r = 4.0$ and $\sigma = 0.1, 0.125, 0.15, 0.2, 0.3, 0.5\text{ S/m}$, for vertical polarization. Dimensions of the cylinder are $d = 2.8\lambda_0(14\text{ cm})$ and $h = 0.4\lambda_0(2\text{ cm})$.

The plots show that the increment in the emissivity with respect to the increment in conductivity is not linear. Also, for relatively low values of conductivity the emissivity shows noticeable variations with respect to the angle of view. However, as the conductivity increases, the value of the emissivity tends to approach a specific value, independently of the view angle. For the cases analyzed in this chapter, the values were around 0.5. In order to gain an insight in the behavior of the scattering and absorption cross sections with respect to the parameters used in this study to estimate the emissivity, a qualitative analysis presented by Ishimaru could be used [8]. The analysis explains how the scattering and absorption cross sections are related to the geometric cross section, wavelength, and dielectric constant of an object. It states that if the size of a particle is much greater than a wavelength, the total cross section Q^{tot} approaches twice the geometric cross section Q^{geo} of the particle as the size increases. Additionally, the total absorbed power, when the particle is very large, cannot be greater than the product of the incident power density and the geometrical cross section, given by $S_i Q^{geo}$, and thus the absorption cross section Q^{abs} approaches a constant somewhat less than the geometric cross section. Using the method developed in Chapter 4 of this study, the emissivity would also be constant. The analysis also states that if the size of the particle is much smaller than a wavelength, the scattering cross section Q^{sca} is inversely proportional to the fourth power of the wavelength and proportional to the square of the volume of the particle; hence, the scattering cross section is small. For this condition, the total cross section would be mostly due to the absorption, and hence the emissivity would be high.

Although some understanding can be gained from that analysis, these two opposite conditions certainly do not represent the cases presented in this study, since the dimensions of the cylinders under study and the incident wavelength are not too different. Then, the values of

the ratio size/wavelength of the objects under analysis would be in the middle range of those extreme cases, requiring a more extensive analysis.

In conclusion, the analysis of emissivity in surfaces and finite size objects in optic region has been studied for a long time; however, the emissivity of objects in the microwave region is an ongoing research [32, 54, 55]. Hence, more studies are needed in order to establish a relationship between emissivity and object properties, such as dimensions, dielectric, as well as frequency and polarizations of interrogating waves. However, at this point, due to both intensive and extensive computational resources required, it is left as a topic for future study.

In summary, in this section a 3D-FDTD algorithm was developed to compute emissivity from finite-size objects. Some tendencies of the emissivity plots with respect to the properties of both the object and the interrogating waves can be observed. The method to compute the absorption and scattering cross sections of finite size objects will be integrated into a passive remote sensing model given in Chapter 5.

CHAPTER 5

MODELING OF MICROWAVE EMISSION FROM IRREGULAR LAYER

5.1 Introduction

The numerical modeling of microwave emission from an irregular layer covering a homogeneous half space is given; including the scattering mechanisms affecting the emission. The scattering behavior of the layer is characterized by the numerically-generated phase matrices. The approach to generate the phase matrices is also given here. In order to validate the phase matrices, both an energy conservation test and comparison with analytical results are carried out. The layer is also characterized by its effective permittivity, which is estimated by a linear model. Finally, the numerical model is validated by comparing model-predicted results with field measurements.

5.2 Construction of phase matrix for a circular cylinder

In order to use the radiative transfer formulation for the inhomogeneous layer, the single scattering phase matrix for the scatterers is needed. The phase matrix is a quantity that relates the Stokes vector of the scattered wave to that of the incident wave.

The values of the scattered fields \vec{E}^s, \vec{H}^s needed for construction of the phase matrix are computed at a constant distance R from the center of the object and at angle (θ, φ) . Figure 5.1 shows the geometry of the object for computation of the phase matrix.

Since both vertical and horizontal incidence polarizations are needed, the FDTD simulation is executed for the same polar angles but varying the incidence polarization

accordingly. The number of both the incident and scattered angles is chosen according to the Gaussian quadrature technique. At each simulation, the impinging field will have an incidence angle (θ^i, ϕ^i) . The fields will be computed and recorded at (ϕ^s, θ^s) at a distance R .

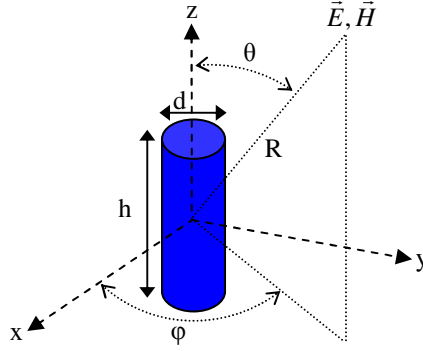


Figure 5.1 Geometry of the object for computation of the phase matrix.

In the same simulation the scattered fields at different frequencies can be computed; however, currently in our approach this requires that the dielectric properties be constant, which is not the case for the dielectric properties of vegetation components. Therefore, the FDTD simulation will be done for single frequency. This also allows reducing the computation time by selecting the parameters of the interrogating wave in such a way that the time-domain duration of the incident pulse is short.

For this purpose a MATLAB® program was develop to generate the coordinates of the scattered-field positions. Since the objects under study show symmetry around one axis (z) the incident angle will vary only in θ . These coordinates (x, y, z) input file is read by the FDTD program, and the scattered fields are obtained. Due to the shift in the \vec{E} and \vec{H} fields' positions in the Yee cell, a trilinear interpolation was performed during the simulation to obtain both \vec{E} and \vec{H} fields at the same point. The output of the program are the scattered fields

\vec{E}^s, \vec{H}^s . In the approach, \vec{E}_x , \vec{E}_y , and \vec{E}_z are normalized by $|\vec{E}_{inc}|$ and \vec{H}_x , \vec{H}_y , \vec{H}_z by $|\vec{H}_{inc}| = |\vec{E}_{inc}/\eta|$, where η is the characteristic impedance of the host medium, respectively.

Since the rectangular components of the \vec{E} and \vec{H} fields are computed in the FDTD program, a coordinate transformation is needed to find the spherical components needed for computation of the phase matrix. For sake of completeness, the R component is also shown in the expression (5.1); however, only the tangential components of the scattered field in the direction of propagation are needed, since those are the components needed to compute the power density. The coordinate transformation is given by

$$\begin{bmatrix} A_R \\ A_\theta \\ A_\phi \end{bmatrix} = \begin{bmatrix} \sin \theta \cos \phi & \sin \theta \sin \phi & \cos \theta \\ \cos \theta \cos \phi & \cos \theta \sin \phi & -\sin \theta \\ -\sin \phi & \cos \phi & 0 \end{bmatrix} \begin{bmatrix} A_x \\ A_y \\ A_z \end{bmatrix} \quad (5.1)$$

where A represents either E or H .

For emission problems, the emitted intensities and phase matrices are independent of azimuthal angle. Therefore, only the zeroth-order Fourier components of the intensities and the phase matrices expanded with respect to the azimuthal angles are needed.

The sizes of the intensity vectors and phase matrices used in the radiative transfer formulation are dependent upon the number of incidence and scattering angles chosen as well as the number of Stokes parameters computed. However, in natural emission, only the first two Stokes parameters, the vertical and horizontal polarizations, are coupled together. Hence, if N polar angles are chosen in accordance with the Gaussian quadrature technique (or any other integration technique used for this purpose), the intensity vectors will be $2N$ -column vectors and the phase matrices will have a dimension of $2N \times 2N$ for each Fourier component. Figure 5.2 shows the computational structure of the phase matrix for the first two Stokes Parameters.

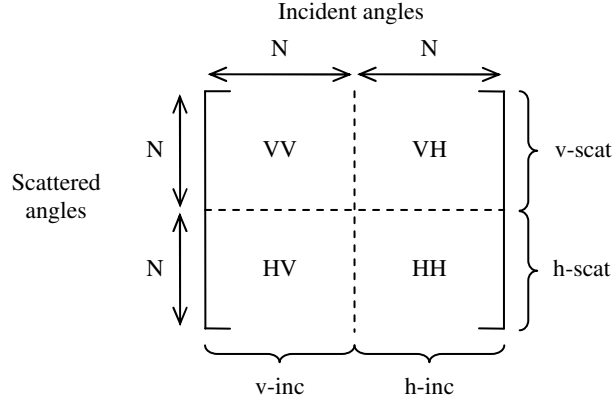


Figure 5.2 Computational structure of the phase matrix for the first two Stokes parameters.

Following the approach shown in [3] the phase matrices for the first two Stokes parameters are computed. However, in [3] the scatterers are represented by spheres, allowing to compute the required scattered fields analytically. Since no analytical solution exists for the scattered fields from finite-size cylinder, in this study the scattered fields are solved using a numerical approach. With the scattered fields components known, all the elements of the phase matrix can be computed. For many applications only like and cross polarizations are of interest; for such cases only the first four elements of the phase matrix are needed as

$$P_s = \frac{4\pi r^2 \eta n_0}{\kappa_s(\theta, \phi) |E_0|^2} \text{Re} \begin{bmatrix} (E_\theta^s H_{\phi'}^{s*})_{v\text{-incidence}} & (E_\theta^s H_{\phi'}^{s*})_{h\text{-incidence}} \\ (-E_{\phi'}^s H_\theta^{s*})_{v\text{-incidence}} & (-E_{\phi'}^s H_\theta^{s*})_{h\text{-incidence}} \end{bmatrix} \quad (5.2)$$

where $\kappa_s(\theta, \phi)$ is the effective volume-scattering coefficient (Np/m) and n_0 is the scatter number density. An estimation of $\kappa_s(\theta, \phi)$ is given by

$$\kappa_s(\theta, \phi) = n_0 Q_s(\theta, \phi) \quad (5.3)$$

Hence,

$$P_s = \frac{4\pi r^2 \eta}{Q_s(\theta, \phi) |E_0|^2} \text{Re} \begin{bmatrix} (E_\theta^s H_{\phi'}^{s*})_{v\text{-incidence}} & (E_\theta^s H_{\phi'}^{s*})_{h\text{-incidence}} \\ (-E_{\phi'}^s H_\theta^{s*})_{v\text{-incidence}} & (-E_{\phi'}^s H_\theta^{s*})_{h\text{-incidence}} \end{bmatrix} \quad (5.4)$$

where $Q_s(\theta)$ is the scattering cross section of the single component.

Another important parameter for characterizing an inhomogeneous medium is its absorption loss, represented by the volume-absorption coefficient in $\kappa_a(\theta, \phi)$, given by

$$\kappa_a(\theta, \phi) = n_0 Q_a(\theta, \phi) \quad (5.5)$$

where $Q_a(\theta, \phi)$ is the absorption cross section. The units of $\kappa_a(\theta, \phi)$ are also Np/m .

The total cross section, also known as the extinction cross section, for a particle is

$$Q_e(\theta, \phi) = Q_a(\theta, \phi) + Q_s(\theta, \phi) \quad (5.6)$$

Most of the studies have dealt with the special case of spherical particles. For these particles, or for nonspherical particles with random orientations, κ_e and κ_s reduce to scalars. However, for this study none of those conditions are met, because κ_e and κ_s are angle dependent, hence they are treated differently. Both parameters, the scattering and absorption cross sections are computed numerically using the approach given in Chapter 4.

The required fields are to be computed at an average distance from the center of the scatterer. Although the approach proposed here is valid for any arbitrary-shape object, the analysis will be focused on cylindrical-shape objects.

In order to validate the numerical model, by comparing its results with field measurements, the components of the irregular layer were chosen to be corn stalks, represented by vertical dielectric cylinders. The bottom half-space bottom was chosen to be soil with rough surface.

Figure 5.3 shows a general configuration for modeling emission from soil in the presence of vegetation components. The vegetation cover modifies the emission from soil, by scattering the soil emission and adding its own emission to the brightness temperature read by a radiometer. The vegetation components are both modeled as dielectric cylinders and assumed to be all vertical. The cylinders are considered to be homogeneous, circular, lossy, and of the same length and diameter.

The ground underlying the slab is represented by a homogeneous, lossy, dielectric half-space and the interface between the slab and ground is taken to be rough with the standard deviation of height $k\sigma$ and correlation length kL describing the degrees of vertical and horizontal roughness.

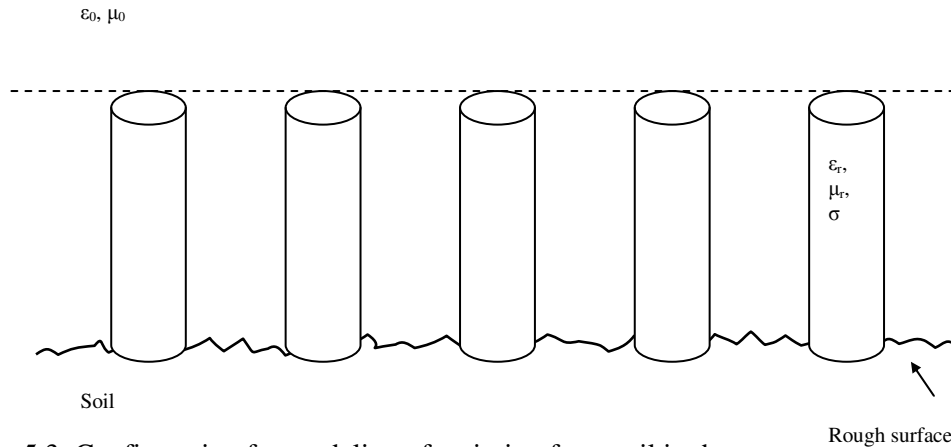


Figure 5.3 Configuration for modeling of emission from soil in the presence of cylindrical vegetation components. Dielectric cylinders are used to model the vegetation components.

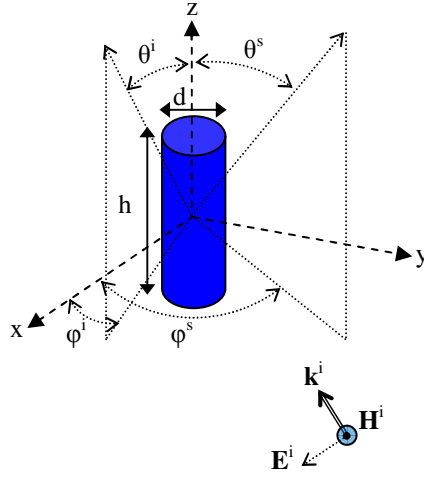


Figure 5.4 Geometry used for FDTD simulation of plane wave impinging on cylinder.

For emission from soil, most of the data available are based on an analysis done at L -band. Therefore, in order to compare prediction of the model with field measurements, the analysis is done at a frequency of 1.4 GHz , at vertical and horizontal polarizations. Figure 5.4 illustrates the geometry for the cylinder in the slab used for the FDTD simulation.

5.3 Construction of phase matrix of corn stalks represented by cylinders

An analysis corresponding to corn stalks represented by vertical cylinders was conducted (Figure 5.5). The analysis was performed at L band. The dielectric properties of corn stalks were obtained from a study reported in [56]; in which measurements of vegetation components at 1-2, 3.5-6.5, and 7.5-8.5 GHz bands, as a function of moisture content and microwave frequency, were performed. The materials measured included the leaves and stalks of corn and wheat. Dielectric measurements also were made of the liquid included in the vegetation material after it was extracted from the vegetation by mechanical means.

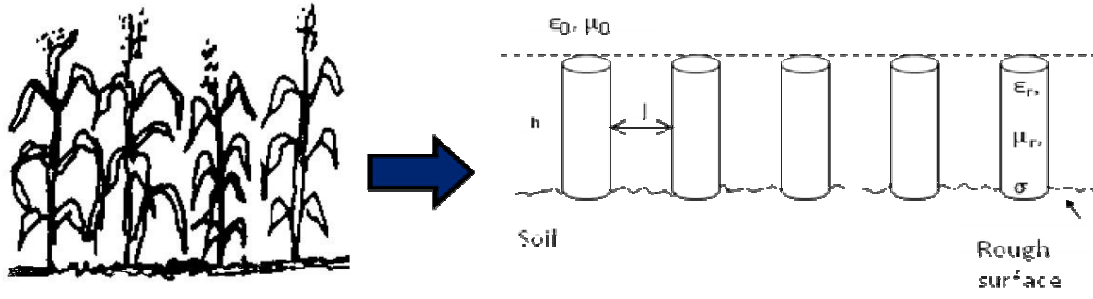
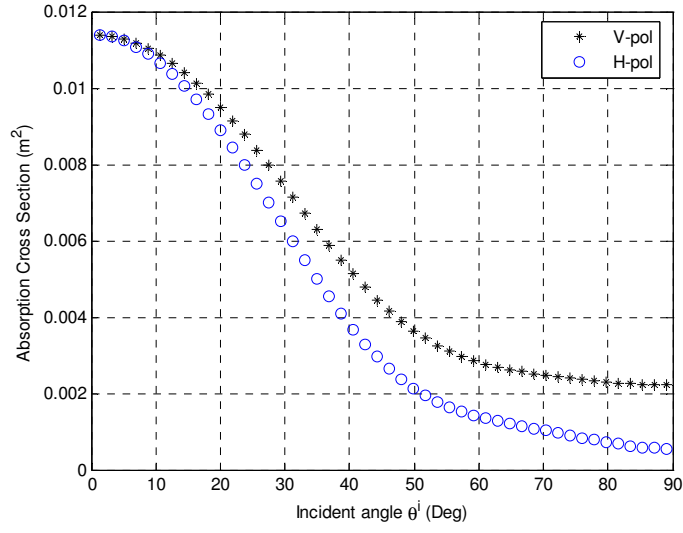


Figure 5.5 Corn stalks represented by dielectric cylinders.

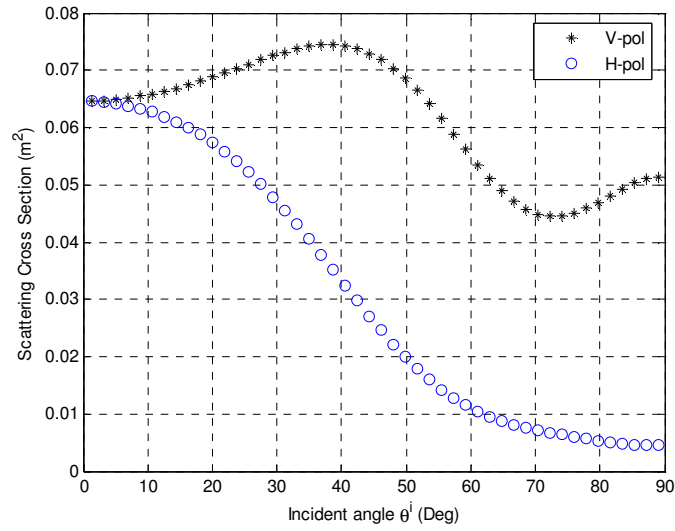
For the analysis carried out in this study the volumetric moisture content m_v was considered to be 0.5, in order to keep the value of ϵ' relatively low so that the computer memory requirement was not high. The dielectric constant for corn stalk would then be $\epsilon' = \epsilon' + j\epsilon'' = 18.5 + j2.1818$.

Similarly, to keep computer memory requirements manageable, the height of the corn stalk was set to be $1.5\lambda_0$ (30 cm), and its diameter was $0.15\lambda_0$ (3 cm). A more detailed report about stalks dimensions can be found in [57]. The range at which the scattered field was computed is obtained from an average distance among scatterers, taking a value of corn fields density from [58].

With the method shown in Chapter 4, and the dielectric properties taken from [57] and dimensions described above, both the absorption and scattering cross sections of the cylinder representing a corn stalk were computed (Figure 5.6).



(a)



(b)

Figure 5.6 (a) Absorption and (b) scattering cross sections numerically computed for a dielectric cylinder representing a corn stalk.

5.4 Validation of phase matrices for energy conservation

Before integrating the numerically-computed phase matrix for a finite-size object into the layer model, it needs to be validated for energy conservation, which requires that for each incident angle (θ^i, ϕ^i)

$$\sum_p \frac{1}{4\pi} \int_0^{2\pi} \int_0^\pi P_{pq} \sin \theta^s d\theta^s d(\phi^s - \phi^i) = 1 \quad (5.7)$$

where P_{pq} denotes the elements of the phase matrix $P(\theta_i, \theta_j)$, and the summation over p includes the elements of the first two Stokes parameters (I_v, I_h) [5].

Assuming $\phi^i = 0^\circ$ equation (5.7) can be also expressed as

$$\sum_p \frac{1}{4\pi} \int_0^{2\pi} \int_{-1}^1 P_{pq} d\mu^s d\phi^s = 1 \quad (5.8)$$

where μ^s is the directional cosine ($\cos \theta^s$) for the scattered field.

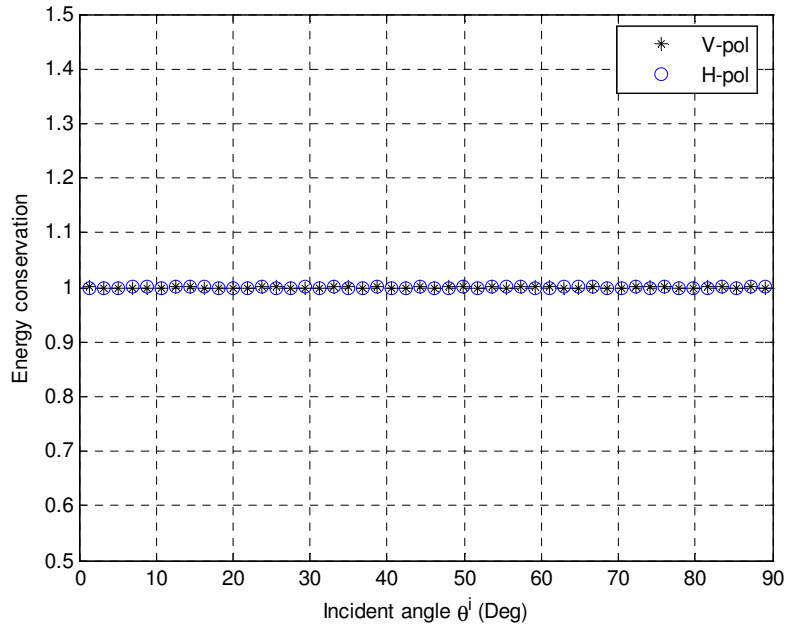


Figure 5.7 Energy conservation test results for numerically-computed phase matrices S^* .

Figure 5.7 shows the energy conservation test results for the numerically-computed phase matrix S^* with respect to the incident angle θ^i . Results show that the energy is conserved at each incident angle. The same results were obtained when testing the phase matrix T^* .

5.5 Verification of computation of backward and forward phase matrices

In order to verify the precision of numerically-computed phase matrices, a comparison with analytically-computed phase matrices was carried out. For this purpose, a configuration as shown in Figure 5.10 is used. The phase matrices describing the scattering and absorption behavior of the inhomogeneous layer are assumed to have a behavior like the one from a sphere. The parameters used for the comparison are given in Table 5.1.

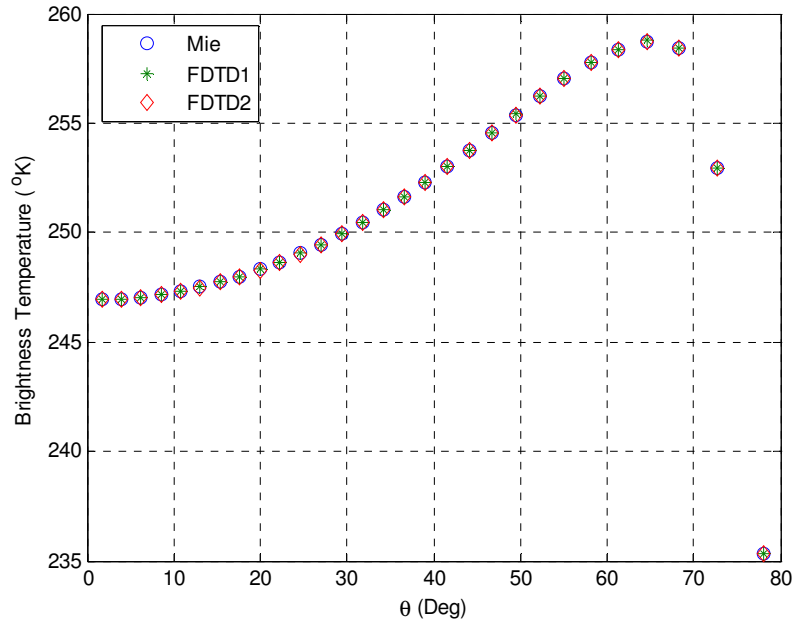
Table 5.1 Parameters used for computation of emission from ground covered with an inhomogeneous layer with phase matrices similar to those of a sphere

Parameter	Value
Scatterer relative permittivity	$\epsilon_{rs} = 3.15 + j0.015$
Effective permittivity of layer	$\epsilon_{rl} = 1.477 + j0.02324$
Permittivity of top half-space	$\epsilon_{ra} = 1.0 + j0.0$
Scatterer volume fraction	$v_f = 30\%$
Scatterer radius	$r = 1 \times 10^{-3} \text{ m}$
Slab thickness	$d = 0.001 \text{ m}$
Background relative permittivity	$\epsilon_{rb} = 1.0 + j0.0$
Permittivity of bottom half space	$\epsilon_{rg} = 5.0 + j0.0$
Layer temperature	$T_L = 293^\circ \text{ K}$
Bottom half space temperature	$T_B = 293^\circ \text{ K}$
Frequency	$f = 35 \text{ GHz}$
Parameters of surface (ground)	$k\sigma = 0.20$ $\sigma = 2.7284 \times 10^{-4} \text{ m}$ $kL = 1.00 \quad L = 1.3642 \times 10^{-3} \text{ m}$
Parameters of top boundary	$k\sigma = 0.50$ $\sigma = 6.8209 \times 10^{-4} \text{ m}$ $kL = 2.50 \quad L = 3.4105 \times 10^{-3} \text{ m}$

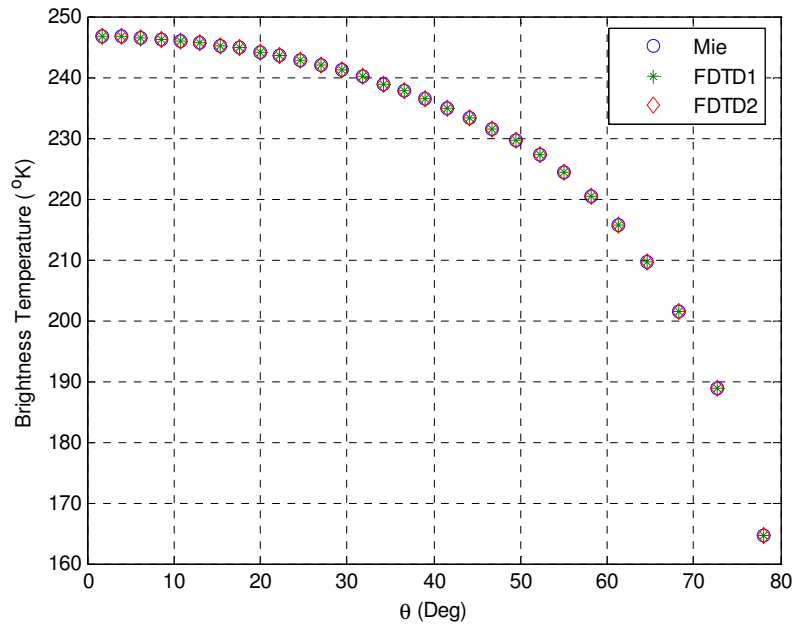
The results shown in Figure 5.8 are obtained using phase matrices computed with (a) fields computed analytically with Mie solutions; (b) FDTD-computed fields, with the phase matrices normalized by constant analytical cross section (FDTD1); and (c) FDTD-computed fields, with phase matrices normalized by the corresponding scattering cross section using

$$Q^{sca} = \frac{\int_{S_0} \text{Re} \left(\frac{1}{2} \vec{E}_s \times \vec{H}_s^* \right) \cdot d\vec{a}}{|S_i|}$$

where \vec{E}_s and \vec{H}_s are the scattered electric and magnetic fields, respectively; \vec{S}_i is the power density of the incident wave, and S_0 is the virtual surface enclosing the object.



(a)



(b)

Figure 5.8 Emission from surface with a cover of a layer with phase matrices characterized as those of a sphere. The phase matrices were obtained using Mie-formulation fields, FDTD-computed fields (phase matrix normalized by analytical scattering cross section – FDTD1), and FDTD-computed fields (phase matrix normalized by scattering cross section using method described in chapter 4 – FDTD2), (a) V-polarization, and (b) H-polarization.

Additionally, although the scattering cross section for a sphere is independent of angle and polarization, due to FDTD-related numerical dispersion, the numerically-computed cross section depends slightly on incident angle. Hence, in order to assure energy conservation, in the third case the phase matrix is normalized by $Q^{sca}(\theta^{inc}, pol)$.

Figure 5.8 shows the model-predicted brightness temperature for both vertical and horizontal polarization. A very good agreement between the results obtained by using the analytically-computed and the numerically-computed phase matrices can be observed.

5.6 Emission scattering mechanisms

The general configuration of a layer between two half spaces is given in Figure 5.9. The total emission into a top homogeneous half space (medium 1) is composed of contributions from both the emission by an inhomogeneous layer (medium 2) and the emission from a homogeneous half-space (medium 3). Because of the inhomogeneities in the layer and the discontinuity at the interfaces between medium 2 and media 1 and 3, respectively; the emissions will further undergo multiple scattering processes; which are described in this section. Since the inclusions volume fraction is very low in the layer, and the host medium dielectric properties are the same as those of the medium 1, the effective permittivity of medium 2 is very close to the permittivity of medium 1; hence, the reflectivity at the top boundary is neglected.

In order to simplify the analysis, the emission from the inhomogeneous layer is decomposed in its upwelling and downwelling components, which are referred to as u_u , and u_d , respectively. The emission from the bottom half-space will be referred to as u_g .

Additionally, the volume density of the layer is considered to be low; hence, the distance between vegetation components is assumed to be large so that only the first order scattering is considered.

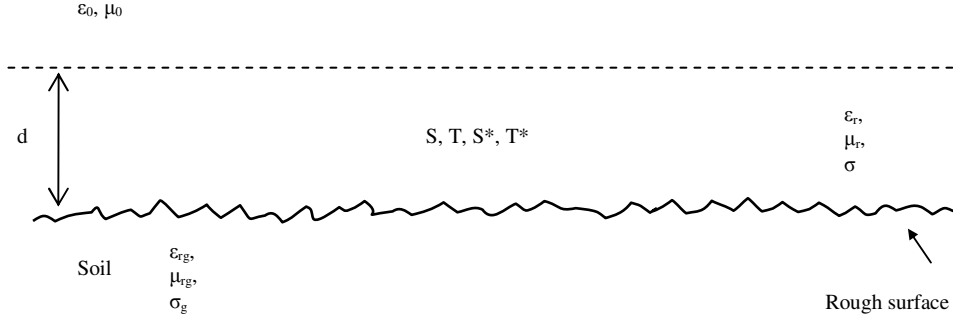


Figure 5.9 General geometry for modeling of emission from soil in the presence of inhomogeneous layer.

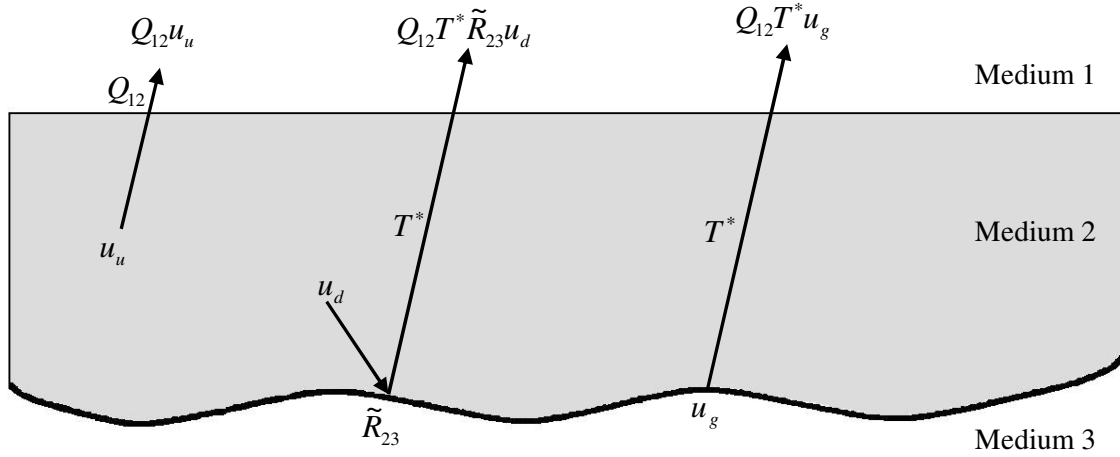


Figure 5.10 Emission scattering mechanisms for upwelling and downwelling emission from the layer and upwelling emission from the bottom half-space.

The multiple scattering mechanisms geometry of the microwave emission problem for an inhomogeneous layer (medium 2) with irregular boundaries is shown in Figure 5.10. The media 1 and 3 are assumed to be homogeneous half spaces, and the layer backward and forward volume scattering phase matrices are the numerically computed single scattering phase matrix

of the layer components, S^* and T^* , respectively. The surface phase matrix \tilde{R}_{23} represents the effective reflectivity matrix at the interface between media 2 and 3; its computation is given below.

Under local thermodynamic equilibrium, the upwelling and downwelling emitted intensities, expressed as brightness temperature, from an elementary layer of optical thickness $\Delta\tau$ at level τ are given by the Kirchhoff-Planck law [3]

$$u_u(\tau; \theta, \phi) = u_d(\tau; \theta, \phi) = U(\theta, \phi)^{-1} \varepsilon_r (1 - \omega(\theta, \phi)) T(\tau) \Delta\tau \quad (5.9)$$

where $T(\tau)$ is the temperature profile of the layer; U is the diagonal matrix of the cosine of the scattered angles, ω is the single-scattering albedo, ε_r is the relative permittivity of the layer, and the layer relative permeability μ_r is assumed to be 1. Both the single-scattering albedo and the optical thickness have angle dependency. Equation (5.9) is used to determine the inhomogeneous layer upward and downward emission sources, namely u_u and u_d , respectively. The emission from lower inhomogeneous half-space, u_g , can be determined using

$$u_g = T_g * \varepsilon_g(\theta) \quad (5.10)$$

where T_g and $\varepsilon_g(\theta)$ are the temperature and emissivity of the ground, respectively.

Figure 5.11 shows the scattering process at the interface between inhomogeneous space (medium 2) and homogeneous half-space (medium 3) due to a unit incident intensity. S^* is the medium-2 backward scattering phase matrix for upward incidence. The surface phase matrix R_{23} , to account for the scattering at the lower boundary, is obtained by using the Integral Equation Method [11].

Following those scattering processes, the corresponding effective reflectivity phase matrix \tilde{R}_{23} at the boundary is obtained in the following way:

$$\tilde{R}_{23} = R_{23} + R_{23}S^*R_{23} + R_{23}S^*R_{23}S^*R_{23} + R_{23}S^*R_{23}S^*R_{23}S^*R_{23} + \dots \quad (5.11a)$$

$$\tilde{R}_{23} = R_{23} \sum_{i=0}^{\infty} (S^*R_{23})^i \quad (5.11b)$$

$$\tilde{R}_{23} = R_{23} (I - S^*R_{23})^{-1} \quad (5.11c)$$

where I represents the identity matrix.

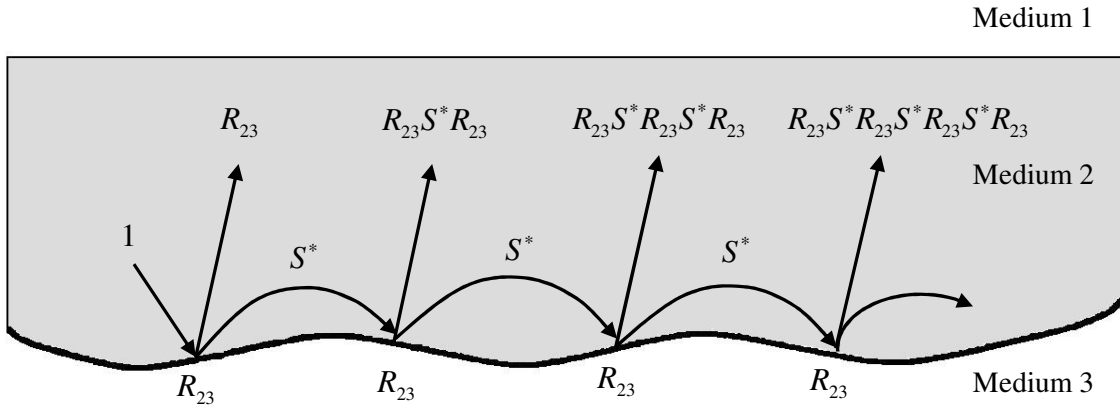


Figure 5.11 Effective reflectivity matrix from the medium 2 - medium 3 interface.

The effective reflectivity phase matrix can be expressed in terms of its Fourier components as:

$$\tilde{R}_{23}^m = R_{23}^m \left(I - fm^2 S^{*m} R_{23}^m \right)^{-1} \quad \text{where } fm = \begin{cases} 2\pi & m=0 \\ \pi & m \geq 1 \end{cases} \quad (5.12)$$

However, for emission only the zeroth order of the Fourier components is used, hence

$$\tilde{R}_{23}^0 = R_{23}^0 \left(I - fm^2 S^{*0} R_{23}^0 \right)^{-1} \quad (5.13)$$

Once the effective reflectivity matrix is obtained, the general scattering operators are given by

$$L_u = Q_{12} \quad (5.14)$$

$$L_d = Q_{12} T^* \tilde{R}_{23} \quad (5.15)$$

$$L_g = Q_{12} T^* \quad (5.16)$$

Again, considering that only the zeroth order Fourier coefficients are needed, then the scattering operators can be expressed as

$$L_u = f_0 Q_{12}^0 \quad (5.17)$$

$$L_d = f_0^2 Q_{12}^0 T^{*0} \tilde{R}_{23}^0 \quad (5.18)$$

$$L_g = f_0 Q_{12}^0 T^{*0} \quad (5.19)$$

5.7 Determination of effective permittivity of layer

The inhomogeneous layer is composed of the host (background) medium and the inclusions (scatterers). Therefore, the effective permittivity ε_l of the inhomogeneous layer is computed using a model given in [5, 16], namely

$$\varepsilon_l^\alpha = \varepsilon_h^\alpha + v_i (\varepsilon_i^\alpha - \varepsilon_h^\alpha) \quad (5.20)$$

where ε_h and ε_i are the host (air) and the inclusion (scatterers) permittivities, respectively; and v_i is the inclusion volume fraction. In the model, α is a constant. For $\alpha = 1$, the preceding formula is known as the linear model, for $\alpha = 1/2$ as the refractive model (since $\varepsilon^{1/2} = n$ is the refractive index), and for $\alpha = 1/3$ as the cubic model. In this work the linear model is used.

The number of inclusions per unit volume is computed using

$$n_0 = v_i / v_0 \quad (5.21)$$

where v_i is the inclusions volume fraction and v_0 is the volume of the inclusion.

5.8 Validation of model by comparison with field measurements

For the most part, the applicability of a given model to a given target type (such as vegetation) is evaluated by comparing the model-calculated scattering coefficient or brightness temperature to the corresponding measured values. Hence, once the model was determined and its components tested for accuracy, it was validated by comparing its predicted results with field measurements. For this purpose, the measurements of the microwave emission from soil with a canopy of corn stalks were used. The measurement program was carried out at the Agricultural Research Center test site in Beltsville, MD. The radiometric measurements over bare fields as well as fields covered with corn, soybean, alfalfa, and grass were reported in [24]. The measurements were made with radiometers at 1.4GHz (L band) and 5GHz (C band) frequencies. For the corn fields, the radiometric measurements were made with incidence angles from 0° to 70° in 10° steps. The scanning plane was approximately 45° to the crop row direction. The soil type was a mixture of Elkton silty loam and Elinsboro sandy loam.

Only those field measurements with parameters similar to the available model-predicted results were used for the model validation.

In the field measurements report, the surface is mentioned as smooth; therefore, to describe the surface roughness practical parameters were chosen [25, 26] that best fit the measurements.

For the FDTD computation of the single scattering phase matrices of the corn stalks, the stalks were represented by vertical dielectric cylinders. The simulated physical dimensions were height $h=30\text{ cm}$, and diameter $d=3\text{ cm}$; however, in the field, the corn stalks had a height of $h=10\text{ cm}$ and a circular diameter of $d=3\text{ cm}$. All parameters used for the comparison of model-predicted emission and field measurements are given in Table 5.2.

Table 5.2 Parameters used for model-predicted emission

Parameter	Value
Scatterer relative permittivity	$\epsilon_{rs} = 18.90 + j 0.3473$
Effective relative permittivity of layer	$\epsilon_{rl} = 1.10 + j 0.0011$
Relative permittivity of top half-space (air)	$\epsilon_{ra} = 1.0 + j 0.0$
Scatterer volume fraction	$v_f = 1\%$
Cylinder diameter	$d = 0.03\text{ m}$
Layer thickness	$h = 0.30\text{ m}$
Background relative permittivity	$\epsilon_{rb} = 1.0 + j 0.0$
Relative permittivity of ground	$\epsilon_{rg} = 9.2 + j 0.8$
Ground temperature	$T = 289^\circ\text{ K}$
Layer temperature	$T = 289^\circ\text{ K}$
Frequency	$f = 1.5\text{ GHz}$ (L-band)
Parameters of surface (ground)	$k\sigma = 0.03141$ $\sigma = 0.0010\text{ m}$ $kL = 0.94247$ $L = 0.0300\text{ m}$

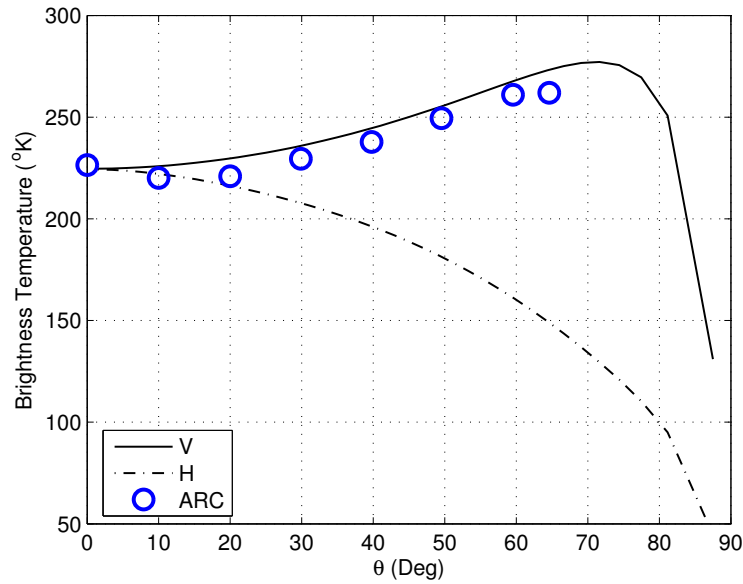


Figure 5.12 Comparison of model-predicted microwave emission and field measurements (ARC) from soil with a cover of corn stalks.

Figure 5.12 shows both the predicted brightness temperature and the field measurements. The microwave emission model used to compute the emission from soil with a layer of vegetation components provides reasonable good results. Data for brightness temperature for horizontal polarization were not available; therefore, the predicted microwave emission for horizontal polarization is given just for completeness.

It is known that for a given soil moisture content ($\geq 10\%$) percent by dry weight, the presence of the vegetation increases the brightness. Hence, the higher prediction from the model could come from the difference between the height of the cylinder representing the stalks (30 cm) in the simulation and the actual height of the stalks in the field (10 cm). However, more analysis should be carried out to characterize with more detail the behavior of the brightness temperature with respect to the parameters of the layer.

Additionally, although not given here, the model-predicted results show: a) the main emission contribution comes from the surface (soil); and b) as expected, the contribution from the upward layer source is greater than the downward layer source.

CHAPTER 6

CONCLUSIONS AND RECOMMENDATIONS

6.1 Summary and Conclusions

A model based on the radiative transfer formulation is presented to predict the microwave emission from an irregular layer on top of a homogeneous half space. A method was developed to compute the emissivity from the layer components. The scattering characteristics, given by the phase matrix, of the elements representing the layer components were computed using the FDTD approach. The phase matrix was then integrated into a layer model that accounts for the scattering within the layer and the scattering between the vegetation layer and ground, using the radiative transfer theory. The emission and scattering at the boundaries were computed using the IEM. In order to validate the numerical model, by comparing its results with field measurements, the components of the irregular layer were chosen to be corn stalks, being represented by vertical dielectric cylinders. The half-space at the bottom was chosen to be soil with rough surface. The microwave emission model predictions were then compared to those field measurements, showing a good agreement. For the case analyzed, the main contribution to the microwave emission into the upper half space (air) came from the ground. This study was focused on cylindrical objects, but the methods to compute both the emissivity and the phase matrix can be applied to objects of arbitrary shape.

6.2 Future work

More detailed analysis of the relationship between emissivity and properties of finite-size objects should be carried out, which will require an extensive computational effort. Also, when the model is applied to emission from soil with vegetation cover, further study needs to be carried out to take into consideration the attenuating and scattering effects of other vegetation components, such as leaves. The plant geometry is an important factor in the microwave emission of vegetation canopy and shall be taken into account in the development of sophisticated theoretical/numerical models. Hence, as the computational power is increased, a study using more realistic dimensions of vegetation components should be conducted.

Furthermore, azimuthal angle dependence of microwave emission by the canopy is not considered in the present research. In natural vegetation covers the distribution of vegetation components can be considered to be random; however, in man-made vegetation canopies such as orchards, plantations and row crops a semideterministic approach may be needed.

APPENDIX A
LIST OF ABBREVIATIONS

FDTD	Finite Difference Time Domain Method
IEM	Integral Equation Method
MoM	Method of Moments
RTT	Radiative Transfer Theory
RTE	Radiative Transfer Equation
MDM	Matrix Doubling Method
SAR	Synthetic Aperture Radar
SPM	Small Perturbation Method
HPC	High Performance Computing
EIFE	Electric Integral Field Equation
MIFE	Magnetic Integral Field Equation
MKS system	meter kilogram second system
3D-FDTD	Three-Dimensional Finite Difference Time Domain Method
BT	Brightness Temperature
LSP/R	Land Surface Process/Radiobrightness model
PEC	Perfect electric conductor

REFERENCES

- [1] E. Schanda, "Applications of Microwaves to Remote Sensing," in *17th European Microwave Conference* Rome, Italy, 1987.
- [2] T. J. Jackson and T. J. Schmugge, "Vegetation Effects on the Microwave Emission of Soil," *Remote Sensing Environment*, vol. 36, pp. 203-212, 1991.
- [3] A. K. Fung, *Microwave Scattering and Emission Models and Their Applications*: Artech House, 1994.
- [4] F. T. Ulaby, R. K. Moore, and A. K. Fung, *Microwave Remote Sensing: Active and Passive, Volume II: Radar Remote Sensing and Surface Scattering and Emission Theory*: Artech House, Inc., 1982.
- [5] F. T. Ulaby, R. K. Moore, and A. K. Fung, *Microwave Remote Sensing: Active and Passive. Volume III: From Theory to Applications*: Artech House, Inc., 1986.
- [6] T. J. Jackson and P. E. O'Neill, "Attenuation of Soil Microwave Emission by Corn and Soybeans at 1.4 and 5 GHz," *IEEE Transactions on Geoscience and Remote Sensing*, vol. 28, pp. 978-980, September 1990.
- [7] A. K. Fung, "A review of Volume Scatter Theories for Modeling Applications," *Radio Science*, vol. 17, pp. 1007-1017, 1982.
- [8] A. Ishimaru, *Wave Propagation and Scattering in Random Media* vol. I and II. New York: Academic Press, 1978.
- [9] L. Tsang and J. A. Kong, "Radiative Transfer Theory for Active Remote Sensing of Half-Space Random Media," *Radio Science*, vol. 13, pp. 763-773, 1978.
- [10] S. Twomey, "Matrix Method for Multiple Scattering Problems," *J. Atmos. Sci.*, vol. 23, pp. 289-296, 1966.
- [11] A. K. Fung, Z. Li, and K. S. Chen, "Backscattering from a Randomly Rough Dielectric Surface," *IEEE Transactions on Geoscience and Remote Sensing*, vol. 30, pp. 356- 369, March 1992.
- [12] D. R. Brunfeldt and F. T. Ulaby, "Microwave Emission from Row Crops," *IEEE Transactions on Geoscience and Remote Sensing*, vol. GE-24, pp. 353-359, May 1986.
- [13] G. Macelloni, S. Paloscia, P. Pampaloni, and R. Ruisi, "Microwave Emission Features of Crops with Vertical Stems," *IEEE Transactions on Geoscience and Remote Sensing*, vol. 36, pp. 332-337, January 1998.
- [14] T. Schmugge, P. E. O'Neill, and J. R. Wang, "Passive Microwave Soil Moisture Research," *IEEE Transactions on Geoscience and Remote Sensing*, vol. GE-24, pp. 12-22, January 1986
- [15] A. Tavakoli, K. Sarabandi, and U. F. T., "Horizontal Propagation through Periodic Vegetation Canopies," *IEEE Transactions on Antennas and Propagation*, vol. 39, pp. 1014-1023, July 1991.
- [16] T. Schmugge and T. J. Jackson, "A Dielectric Model of the Vegetation Effects on the Microwave Emission from Soils," *IEEE Transactions on Geoscience and Remote Sensing*, vol. 30, pp. 757-760, July 1992.

- [17] W. L. Crosson, A. S. Limaye, and C. A. Laymon, "Parameter Sensitivity of Soil Moisture Retrievals from Airborne L-Band Radiometer Measurements in SMEX02," *IEEE Transactions on Geoscience and Remote Sensing*, vol. 43, pp. 1517-1528, July 2005.
- [18] T. Mo, T. J. Choudhury, T. J. Schmugge, J. R. Wang, and T. J. Jackson, "A Model for Microwave Emission from Vegetation-Covered Fields," *Journal of Geophysical Research*, vol. 87, pp. 11,229-11,237, 1982.
- [19] J. P. Wigneron, M. Pardé, P. Waldteufel, A. Chanzy, Y. Kerr, S. Schmidl, and N. Skou, "Characterizing the Dependence of Vegetation Model Parameters on Crop Structure, Incidence Angle, and Polarization at L-Band," *IEEE Transactions on Geoscience and Remote Sensing*, vol. 42, pp. 416-425, February 2004.
- [20] C. Utku and R. H. Lang, "Simulations of L-Band Brightness Temperature of a Quasi-Periodic Corn Canopy," *IEEE International Geoscience and Remote Sensing Symposium*, vol. 5, pp. V-530 V-533, July 7-11 2008.
- [21] M. A. Karam, "A Physical Model for Microwave Radiometry of Vegetation," *IEEE Transactions on Geoscience and Remote Sensing*, vol. 35, pp. 1045-1058, July 1997.
- [22] P. D. Matthaeis and R. H. Lang, "Comparison of Surface and Volume Currents Models for Electromagnetic Scattering from Finite Dielectric Cylinders," *IEEE Transactions on Antennas and Propagation*, vol. 57, pp. 2216-2220, July 2009.
- [23] Z. Zhang, G. Sun, and L. Zhang, "A Discrete Model to Evaluate Vegetation Effect in Passive Microwave Soil Moisture Retrieval," *IEEE International Geoscience and Remote Sensing Symposium, 2003. IGARSS '03*, vol. 2, pp. 1338-1340, July 21-25 2003.
- [24] J. R. Wang, J. C. Shiue, S. L. Chuang, R. T. Shin, and M. Dombrowski, "Thermal Microwave Emission from Vegetated Fields: A Comparison Between Theory and Experiment," *IEEE Transactions on Geoscience and Remote Sensing*, vol. GE-22, pp. 143-150, March 1984.
- [25] Y.-A. Liou, K.-S. Chen, and T.-D. Wu, "Reanalysis of L-Band Brightness Predicted by the LSP/R Model for Prairie Grassland: Incorporation of Rough Surface Scattering," *IEEE Transactions on Geoscience and Remote Sensing*, vol. 39, pp. 129-135, January 2001.
- [26] Y. Q. Jin and X. Z. Huang, "Correlation of Temporal Variations of Active and Passive Microwave Signatures from Vegetation Canopy," *IEEE Transactions on Geoscience and Remote Sensing*, vol. 34, pp. 257-263, January 1996.
- [27] M. N. O. Sadiku and A. F. Peterson, "A Comparison of Numerical Methods for Computing Electromagnetics Fields," *IEEE Southeastcon '90*, vol. 1, pp. 42-47, April 1-4 1990.
- [28] A. Taflove and M. E. Brodwin, "Numerical Solution of Steady-State Electromagnetic Scattering Problems Using the Time-Dependent Maxwell's Equations," *IEEE Transactions on Microwave Theory and Techniques*, vol. MIT-23, pp. 623-630, August 1975.
- [29] K. S. Yee, "Numerical Solution of Initial Boundary Value Problems Involving Maxwell's Equations in Isotropic Media," *IEEE Transactions on Antennas and Propagation*, vol. AP-14, pp. 302-307, May 1966.
- [30] K. L. Shlager and J. B. Schneider, "A Selective Survey of the Finite-Difference Time-Domain Literature," *IEEE Antennas and Propagation Magazine*, vol. 37, pp. 39-57, August 1995.

- [31] A. Taflove, M. J. Picket-May, and S. C. Hagness, "FDTD – How Complex a Problem Can We Solve?," *IEEE Antennas and Propagation Society International Symposium*, vol. 3, July 16-21 2000.
- [32] L. M. Camacho, M. Lu, and S. Tjuatja, "Study of Emission from Finite-Size Objects using FDTD," *IEEE International Geoscience and Remote Sensing Symposium, 2008. IGARSS 2008*, vol. 4, pp. IV 1153-IV 1156, July 7-11 2008.
- [33] D. C. Bertilone, "Stokes Parameters and Partial Polarization of Far-Field Radiation Emitted by Hot Bodies," *Journal of Optical Society of America*, vol. 11, pp. 2298-2304, August 1994.
- [34] S. Chandrasekhar, *Radiative Transfer*. New York: Dover, 1960.
- [35] C. F. Bohren and D. R. Huffman, *Absorption and Scattering of Light by Small Particles*: John Wiley and Sons, 1983.
- [36] S. Tjuatja, "Theoretical Scatter and Emission Models for Inhomogeneous Layers with Application to Snow and Sea Ice," in *Electrical Engineering Department Arlington Texas: University of Texas at Arlington*, 1992.
- [37] A. Ishimaru and R. L. Cheung, "Multiple Scattering Effects on Wave Propagation due to Rain," *Annals of Telecommunications*, vol. 35, pp. 373-379, 1980.
- [38] A. K. Fung and G. W. Pan, "A scattering model for perfectly conducting random surfaces. I - Model development. II - Range of validity," *International Journal of Remote Sensing*, vol. 8, pp. 1579-1605, November 1987.
- [39] A. K. Fung, C. Y. Hsieh, G. Nesti, A. J. Sieber, and P. Coppo, "A Further Study of the IEM Surface Scattering Model," *IEEE Transactions on Geoscience and Remote Sensing*, vol. 35, pp. 901-909, July 1997.
- [40] A. Taflove and S. C. Hagness, *Computational Electrodynamics: The Finite Difference Time-Domain Method*, 3 ed. MA: Artech House, 2005.
- [41] F. T. Ulaby, R. K. Moore, and A. K. Fung, *Microwave Remote Sensing: Active and Passive. Volume I: Microwave Remote Sensing Fundamentals and Radiometry*: Artech House, Inc., 1981.
- [42] T. Schmugge, "Remote Sensing of Surface Soil Moisture," *Journal of Applied Meteorology*, vol. 17, October 1978.
- [43] S. H. Yueh and R. Kwok, "Electromagnetic Fluctuations for Anisotropic Media and the Generalized Kirchhoff's Law," *Radio Science*, vol. 28, pp. 471-480, 1993.
- [44] M. A. Karam, A. K. Fung, R. H. Lang, and N. S. Chauhan, "A Microwave Scattering Model for Layered Vegetation," *IEEE Transactions on Geoscience and Remote Sensing*, vol. 30, pp. 767-784, 1992.
- [45] F. T. Ulaby, K. Sarabandi, K. McDonald, and M. C. Dobson, "Michigan Microwave Canopy Scattering Model," *International Journal of Remote Sensing*, vol. 11, pp. 1223-1253, July 1990.
- [46] R. F. Harrington, *Field Computations by Moment Methods*, 1968.
- [47] P. D. Matthaeis and R. H. Lang, "Microwave Scattering Models for Cylindrical Vegetation Components," *Progress In Electromagnetics Research*, vol. 55, pp. 307-333, 2005.
- [48] F. T. Ulaby and M. A. El-Rayes, "Microwave Dielectric Spectrum of Vegetation — Part II: Dual Dispersion Model," *IEEE Transactions on Geoscience and Remote Sensing*, vol. GE-25, pp. 550-557, September 1987.

- [49] S. C. Chauhan, R. H. Lang, and K. J. Ranson, "Radar Modeling of a Boreal Forest," *IEEE Transactions on Geoscience and Remote Sensing*, vol. 29, pp. 627–638, July 1991.
- [50] S. C. Chauhan, D. M. Le Vine, and R. H. Lang, "Discrete Scatter Model for Microwave Radar and Radiometer Response to Corn: Comparison of Theory and Data," *IEEE Transactions on Geoscience and Remote Sensing*, vol. 32, pp. 416–426, March 1994.
- [51] L. Tsang, "Thermal Emission of Nonspherical Particles," *Radio Science*, vol. 19, pp. 966-974, July-August 1984.
- [52] A. Ishimaru, *Electromagnetic Wave Propagation, Radiation, and Scattering*: Prentice Hall, 1991.
- [53] U. Carlberg, Z. Sipus, and P. S. Kildal, "Calculation of Absorption Cross Section of Lossy Objects used when Measuring Antenna in Reverberation Chambers," *Antennas and Propagation Society International Symposium*, vol. 2, pp. 470-473, June 16-21 2002.
- [54] J. Wang, "Research on the Interception Power of Finite Object in Plane Wave," *Conference on Environmental Electromagnetics, 2009. CEEM 2009. 5th Asia-Pacific* pp. 26-29, 2009.
- [55] J. Wang, Y. Yang, J. Miao, and Y. Chen, "Emissivity Calculation for a Finite Circular Array of Pyramidal Absorbers Based on Kirchhoff's Law of Thermal Radiation," *IEEE Transactions on Antennas and Propagation*, vol. 58, pp. 1173-1180, April 2010.
- [56] F. T. Ulaby and R. P. Jedlicka, "Microwave Dielectric Properties of Plant Materials," *IEEE Transactions on Geoscience and Remote Sensing*, vol. GE-22, pp. 406-415, July 1984.
- [57] C. Igathinathane, A. R. Womach, S. Sokhansanj, and S. Narayan, "Size Reduction of High- and Low-Moisture Corn Stalks by Linear Knife Grid System," *Biomass and Bioenergy*, vol. 33, pp. 547-557, April 2009.
- [58] R. H. Lang, C. Utku, P. de Matthaeis, T. D. Tsegaye, P. E. O'Neill, and C. Laymon, "Active and Passive Microwave Sensing of Soil Moisture through Corn Fields of Varying Density," in *URSI XXVII General Assembly* The Netherlands, 2002.

BIOGRAPHICAL INFORMATION

Luis M. Camacho-Velázquez was born in Poza Rica, Mexico. He earned a bachelor's degree at the Universidad Autónoma de Nuevo León (UANL), Mexico in 1988. At the same university he earned an M.S. degree in 1991. From October 1991 to March 1993 he conducted research at the Technische Hochschule Darmstadt, Germany.

From 1989 to 1998 he was a lecturer at the Universidad Autónoma de Nuevo León, where he also held administrative positions. He was also an engineer providing services to industry. In 2010 he was a lecturer for the same university in a distance-education modality.

In 2004 he earned an M.S. degree in Electrical Engineering from The University of Texas at Arlington. In the same institution he earned in 2011 a Ph.D. degree from the Electrical Engineering Department.

During his stay as student at The University of Texas at Arlington, he was appointed as a lecturer for several undergraduate courses and as a graduate teaching assistant for both graduate and undergraduate courses at the Electrical Engineering Department. He was also appointed as a graduate research assistant at the Wave Scattering Research Center.

His main research interests are modeling for remote sensing, numerical techniques for electromagnetics, and parallel computation.